

Novel Instrumentation and Methods for Chemical Applications of Dissolution Dynamic Nuclear Polarization

THÈSE N° 7171 (2016)

PRÉSENTÉE LE 16 DÉCEMBRE 2016

À LA FACULTÉ DES SCIENCES DE BASE

LABORATOIRE DE RÉSONANCE MAGNÉTIQUE BIOMOLÉCULAIRE

PROGRAMME DOCTORAL EN CHIMIE ET GÉNIE CHIMIQUE

ÉCOLE POLYTECHNIQUE FÉDÉRALE DE LAUSANNE

POUR L'OBTENTION DU GRADE DE DOCTEUR ÈS SCIENCES

PAR

Jonas MILANI

acceptée sur proposition du jury:

Prof. K. Severin, président du jury

Prof. G. Bodenhausen, Dr S. Jannin, directeurs de thèse

Dr F. Engelke, rapporteur

Dr J. Van Bentum, rapporteur

Dr L. Emsley, rapporteur



ÉCOLE POLYTECHNIQUE
FÉDÉRALE DE LAUSANNE

Suisse
2016

Abstract

One of the major disadvantages of Nuclear Magnetic Resonance (NMR) is its low sensitivity, mainly due to a very low spin polarization. Since 2003, Dissolution Dynamic Nuclear Polarization (D-DNP) provides a way of overcoming this drawback in solution by increasing polarization by factors exceeding 10'000-fold. In a D-DNP experiment, the high electron spin polarization at low temperatures is transferred to other nuclei (like ^1H and ^{13}C) by microwave irradiation, and the frozen sample is subsequently dissolved to room temperature while preserving part of the polarization. This thesis presents novel conceptual and instrumental developments in D-DNP that enable a better hyperpolarization of several nuclear spins.

More specifically, after a brief introduction to NMR and D-DNP in Part A, we will discuss in Part B new strategies for improving microwave irradiation and implementing Longitudinal Detection Electron Spectroscopy Resonance (LODESR) in situ, c.a. at low temperature and high magnetic field. We will see how Cross Polarization can be made fully compatible with D-DNP with an original double resonance circuit developed in our laboratory (^1H and another nucleus like ^{13}C , ^{15}N , ^{29}Si or ^{129}Xe). Finally, we will show how the problem of low field transfer of hyperpolarized solutions can be overcome by the use of a novel concept of a magnetic tunnel that sustains the magnetic field and prevent excessive losses of our hyperpolarized "ambitions". Finally, new applications in D-DNP that were either enabled or better realized by these new strategies are briefly presented in Chapter C.

Key words: Nuclear Magnetic Resonance (NMR); Dynamic Nuclear Polarization (DNP); Dissolution-DNP (D-DNP); hyperpolarization; TEMPO free radical; Cross-Polarization (CP); Magnetic Tunnel; CP D-DNP Probe.

Résumé

L'un des désavantages majeurs en Résonance Magnétique Nucléaire (RMN) est sa faible sensibilité, principalement due à la très faible polarisation des spins. Depuis 2003, la Dissolution de Polarisation Dynamique Nucléaire (D-PDN) permet de surpasser cet inconvénient en solution en augmentant la polarisation d'un facteur supérieur à 10'000. Dans une expérience de D-PDN, la haute polarisation de spin électronique à basse température est transférée à d'autres noyaux (comme ^1H ou ^{13}C) par irradiation de micro-ondes. L'échantillon gelé est, par la suite, rapidement dissous à température ambiante. Il préserve ainsi en partie sa polarisation. Cette thèse présente de nouveaux développements conceptuels et instrumentaux en D-DNP qui permettent une meilleure hyperpolarisation de différents spins nucléaires.

Plus précisément, après une brève introduction à la RMN et D-PDN dans la partie A, nous allons discuter, dans la partie B, de nouvelles stratégies pour améliorer l'irradiation de micro-ondes et la mise en œuvre de la Longitudinal Detection Electron Spectroscopy Resonance (LODESR) in situ, c.a. à basse température et champ magnétique élevé. Nous allons voir comment la Polarisation Croisée peut être parfaitement compatible avec la D-PDN avec un circuit original à double résonances développé dans notre laboratoire (^1H et un autre noyau comme ^{13}C , ^{15}N , ^{29}Si ou ^{129}Xe). Enfin, nous allons montrer comment le problème du faible champ ambiant durant le transfert des échantillons hyperpolarisés peut être surmonté par l'utilisation d'un nouveau concept de tunnel magnétique qui soutient le champ magnétique et évite ainsi des pertes excessives de nos "ambitions hyperpolarisées". Enfin, de nouvelles applications dans D-PDN qui ont été soit permises ou mieux réalisées par ces nouvelles stratégies sont brièvement présentées dans la partie C.

Mots-clefs : Résonance Magnétique Nucléaire (RMN); Polarisation Dynamique Nucléaire (PDN); Dissolution-PDN (D-PDN); hyperpolarisation; TEMPO radical libre; Polarisation Croisée; Tunnel Magnétique.

Table of Contents

Abstract / Résumé	3
Table of Contents	6
Part A : Introduction to Nuclear Magnetic Resonance (NMR) and Dynamic Nuclear polarization (DNP)	9
Chapter 1: Nuclear Magnetic Resonance (NMR)	11
a. Importance of NMR spectroscopy	11
b. Importance of Polarization in NMR	12
c. Principal DNP techniques	15
d. Electron Spin Resonance (ESR)	15
i. Spectra of Radicals	16
Chapter 2: DNP effects as a function of the ESR lineshape, concentration, etc.	18
a. Overhauser Effect	18
b. Solid Effect	19
c. Cross Effect	20
d. Thermal Mixing	21
e. The importance of Spin Diffusion	23
Chapter 3: Conventional dissolution DNP experiments	25
a. D-DNP hardware	26
i. Temperature management	27
ii. Microwave irradiation	28
b. Practical DNP experiment	29
i. DNP at 3.35 T with TEMPOL radical	30
ii. DNP at 6.7 T with TEMPOL radical	30
iii. Effect of radical concentration	31
iv. Effect of Microwaves Frequency Modulation	31
c. Problems addressed in this thesis	33

Part B : Improved and novel instrumentation for Dissolution DNP	37
Chapter 1: Experimental design	39
a. Details of the top and bottom of the probe	41
Chapter 2: Longitudinal Detection of ESR (LODESR)	45
a. Introduction	45
b. Probe Design	45
c. Results (ESR spectra T_{1e} , saturation curve)	48
Chapter 3: Low temperature CP-DNP probe	52
a. RF circuit details	52
b. Tuning and matching strategy	56
c. Pulse sequences adapted for cross-polarization (CP)	58
d. Samples containing ^{15}N	61
i. CP optimization	62
e. Samples containing ^{29}Si	64
f. Solution-state ^{15}N NMR at 300 K	65
Chapter 3: Dissolution	68
a. Introduction	68
b. Dissolution stick	68
c. Fluid path	72
Chapter 4: Transfer through a magnetic tunnel	75
a. Introduction	75
i. Relaxation mechanisms	76
b. Designs of magnetic tunnels	77
i. Magnetic field mapping	79
ii. Relaxometry	80
iii. Magnetic tunnel structure	82
iv. Adiabatic condition	86
v. Results and discussion	89
c. Effects in systems with quadrupolar nuclei	94

Chapter 5: Laser excitation for D-DNP	97
Part C : Applications	103
Chapter 1: ^1H DNP with a magnetic tunnel	106
a. Drug Screening by hyperpolarized ligands	106
b. Hyperpolarized water without contaminants	109
c. Water-LOGSY	111
Chapter 2: Cross Polarization (CP)	114
a. Hyperpolarized Glucose	114
b. Hybrid polarizing solids (HYPSOs) for pure hyperpolarized liquids	116
c. Natural Abundance ^{13}C – Metabolomics	118
Chapter 3: Spectra of highly polarized molecules in solution	121
Part D : Conclusion	125
Part E : Annexes	127
Probe design	129
Magnetic tunnel design	130
Remerciements	133
Curriculum Vitae	135

Part A:

**Introduction to Nuclear Magnetic Resonance (NMR) and
Dynamic Nuclear polarization (DNP)**

Chapter 1: Nuclear Magnetic Resonance (NMR)

a. Importance of NMR spectroscopy

Nuclear Magnetic Resonance (NMR) is a powerful spectroscopic technique daily used for molecular characterization and protein structure determination. NMR spectroscopy involves the study of transitions of nuclear spins, which corresponds of an energy on the order of MHz (radiofrequencies). This corresponds to low energies in spectroscopy. By comparison, electron spin resonance occurs in the microwave domain (GHz), while molecular vibrational and rotational resonances occur in the infrared area (300 GHz to 430 THz, or wavelengths of 1 mm to 700 nm.) Electronic transitions (changes between electronic orbitals) needs an energy comparable to visible light (400 nm - 750 nm) or ultraviolet light (200 nm - 400 nm).

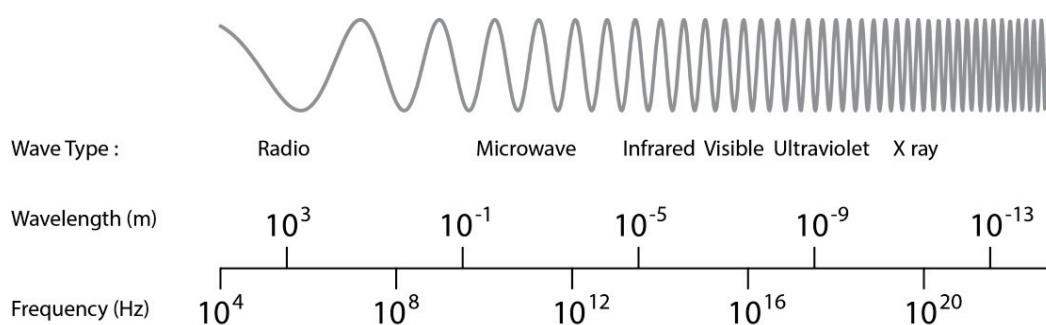


Fig. 1 Electromagnetic waves: general scheme. Nuclear Magnetic Resonance takes place in radio frequency range. This corresponds to low-energy electromagnetic waves.

For each spectroscopic technique, a source of electromagnetic waves that resonate at the frequency or energy of the transition is needed. Techniques to create such waves are highly dependent on the frequency domain. UV-VIS spectroscopy uses a light source, microwave irradiation can be generated by solid state sources and radio frequency (RF) waves for NMR analysis can be created thanks to an electronic device composed by a coil and capacitors coupled to Signal Generation Unit (SGU) and an amplifier. Resonant irradiation is ultimately transmitted to the NMR sample via a tuned and matched coil, creating an oscillating field (B_1) perpendicular to the main static magnetic field (B_0). Simultaneously, this coil serves to pick up the signal. Depending on the application, especially on the geometrical requirements of the sample, coils can have different forms, for example saddle coils or solenoid coils (figure. 2).

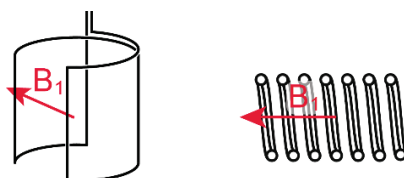


Fig. 2 Saddle coil and solenoid coil with the direction of the oscillating B_1 field. Depending on geometrical constraints dictated by the main magnetic field and by the sample insertion, different types of coils can be chosen. Because the insertion of the sample is done from the top, the saddle coil is commonly used in all liquid state NMR spectrometers. In Magic Angle Spinning (MAS) NMR, solenoid coils are usually used.

b. Importance of Polarization in NMR

The signal in NMR originates from the magnetic moment or spin of a nucleus. NMR signals can in principle be observed as soon as the magnetic moment $\vec{\mu}$ has a non-zero value.

$$\vec{\mu} = \gamma \hbar \vec{I} \quad (1.1)$$

where γ is the gyromagnetic ratio and \vec{I} the spin of the nucleus. The gyromagnetic ratio and spin are intrinsic quantum properties of each nucleus, and the spin number is related to the number of energy levels of the magnetic moment. For $I = \frac{1}{2}$, $m_i = \left[-\frac{1}{2}; \frac{1}{2}\right]$, the states of the system are defined in the literature as $m_\alpha = |\alpha\rangle = -\frac{1}{2}$ and $m_\beta = |\beta\rangle = +\frac{1}{2}$. At $B_0 = 0$, all states are degenerate, but if an external magnetic field $B_0 \neq 0$ is applied an energy splitting from the Zeeman Effect arises. It is proportional to γ and B_0 [2].

$$\Delta E = -\vec{\mu} B_0 = -\gamma \hbar \vec{I} B_0 \quad (1.2)$$

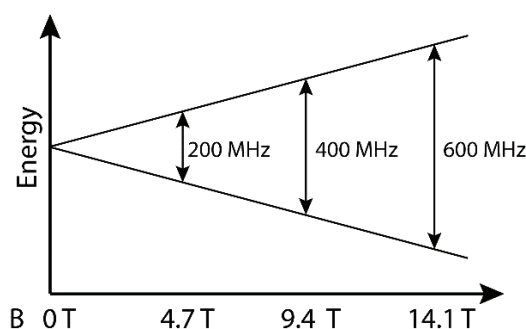


Fig. 3 Zeeman effect. NMR spectrometers are classified according to the ^1H resonance frequency. For example, 200 MHz for a field of 4.7 T, 400 MHz for a field of 9.4 and 600 MHz for a field of 14.1 T are common commercially available fields. At 9.4 T, the ^1H resonance corresponds to an energy of $2 \cdot 10^{-26}$ J or $1.25 \cdot 10^{-7}$ eV. The benefits of high field spectrometers are a higher signal due to a higher polarization but also a better resolution due to the larger chemical shifts.

The measured NMR signal is proportional to the total bulk magnetization of the sample under investigation, and this magnetization is proportional to the number of spins in the sample, but also to the nuclear spin alignment, also called spin polarization.

$$S \propto M = P * N_{spin} \quad (1.3)$$

For a spin $\frac{1}{2}$, the polarization is defined as the difference of populations between the energy levels, divided by the sum of these populations.

$$P \equiv \frac{n_{\alpha} - n_{\beta}}{n_{\alpha} + n_{\beta}} \quad (1.4)$$

where n_{α} and n_{β} respectively are the populations in α and β states. At thermal equilibrium, the population distribution follows Boltzmann's rule:

$$\frac{n_i}{n_{tot}} = \frac{g_i e^{-E_i/k_B T}}{Z(T)} \quad (1.5)$$

where $Z(T) = \sum_i g_i e^{-E_i/k_B T}$, g_i is the degeneracy of the energy levels, here equal to 1. E_i is the Zeeman energy which depends on the gyromagnetic ratio γ .

$$E_i = m_i \hbar \gamma B_0 \quad (1.6)$$

where m_i is the spin state, \hbar Plank's constant and B_0 the external magnetic field. In a spin $\frac{1}{2}$ system, the spin states are $m_i = \left[-\frac{1}{2}; \frac{1}{2}\right]$. The difference of the energies corresponds to

$$\Delta E = E_{\beta} - E_{\alpha} = (m_{\beta} - m_{\alpha}) \hbar \gamma B_0 = \hbar \gamma B_0 \quad (1.7)$$

P can be easily calculated by applying the mathematical relation $\tanh(z) = \frac{e^z - e^{-z}}{e^z + e^{-z}}$, since the polarization for a spin $\frac{1}{2}$ system is given by:

$$P = \frac{n_{\alpha} - n_{\beta}}{n_{\alpha} + n_{\beta}} = \frac{e^{-E_{\alpha}/k_B T} - e^{-E_{\beta}/k_B T}}{e^{-E_{\alpha}/k_B T} + e^{-E_{\beta}/k_B T}} = \tanh\left(\frac{\hbar \gamma B_0}{2k_B T}\right) \quad (1.8)$$

Note that all terms n_{tot} , $Z(T)$ and g_i are canceled. For clarity, the final equation is written again :

$$P = \tanh\left(\frac{\hbar \gamma B_0}{2k_B T}\right) \quad (1.9)$$

Equation 1.9 explains the cause of the greatest disadvantage of NMR, its low sensitivity. The weak signal intensity is due to the very low nuclear spin polarization. Table 1 gives a non-exhaustive list of nuclear spins $\frac{1}{2}$ that will be observed in the course of the present thesis with their polarizations for different temperatures and magnetic fields. Again, these polarizations and temperatures are the ones that we shall be working with in this thesis. Polarizations at room temperature are very low, below 0.01%, even for ^1H spins that have the highest gyromagnetic ratio. Furthermore, for carbon-13 NMR

only 1% of the carbon atoms naturally possess a spin (^{13}C with a spin $\frac{1}{2}$). This is even worse for nitrogen since ^{15}N has a 0.36% natural abundance. When both polarization and abundance are low, the strategy consisting of increasing the number of scans becomes impractical as the signal to noise ratio only increases with the square root of the number of scans. According to equation 1.9 there are not many ways to increase the polarization and therefore the signal of the sample. The field B_0 can be increased. The strongest supraconducting magnet has a field B_0 of 28.2 (1.2 GHz) [3] or higher thanks hybrid magnet at 40 T [4] which demands a very long development and a lot of money. And even in this huge field, the ^1H polarization only raises to 0.07 %. The second possibility to increase the signal is to decrease the temperature T . Moderate fields (3.35 T) and low temperatures (4.2 K) give a ^1H polarization of 0.08%, which is already better than in a field of 22.2 T but still weak. Even a temperature of 1.2 K is not enough to reach a polarization of 0.1 %. For a 9.4 T magnet, the ^1H polarization is 0.8 % at 1.2 K. It goes without saying that this low temperature approach is possible only in the solid state. The last possibility is to change the gyromagnetic ratio γ . Electrons have a gyromagnetic ratio that is almost 3 orders of magnitudes higher than protons $\gamma(e) = 660 \gamma(^1\text{H})$. Table 1 gives the electronic polarizations under the same conditions as before. At low temperature and moderate magnetic fields, the electronic polarization becomes close to 100 %. The solution for NMR developments is to use electrons as a source of polarization. This corresponds to the initial idea of Dynamic Nuclear Polarization (DNP).

B_0 (T)	$\gamma(\text{s}^{-1}\text{T}^{-1})$	P(%) (T = 300K)			P(%) (T = 4.2K)			P(%) (T = 1.2K)		
		3.35 T	6.70 T	9.4 T	3.35 T	6.70 T	9.4 T	3.35 T	6.70 T	9.4 T
^1H	$42.576 \cdot 10^6$	$1.1 \cdot 10^{-3}$	$2.3 \cdot 10^{-3}$	$3.2 \cdot 10^{-3}$	$8.1 \cdot 10^{-2}$	$1.6 \cdot 10^{-2}$	$2.3 \cdot 10^{-1}$	0.29	0.57	0.80
^{13}C	$10.705 \cdot 10^6$	$2.9 \cdot 10^{-4}$	$5.8 \cdot 10^{-4}$	$8.1 \cdot 10^{-4}$	$2.0 \cdot 10^{-2}$	$4.1 \cdot 10^{-2}$	$5.6 \cdot 10^{-2}$	$7.2 \cdot 10^{-2}$	0.14	0.20
^{15}N	$-4.316 \cdot 10^6$	$1.2 \cdot 10^{-4}$	$2.3 \cdot 10^{-4}$	$3.3 \cdot 10^{-4}$	$8.3 \cdot 10^{-3}$	$1.7 \cdot 10^{-2}$	$2.3 \cdot 10^{-2}$	$2.9 \cdot 10^{-2}$	0.058	0.08
^{29}Si	$-8.465 \cdot 10^6$	$2.3 \cdot 10^{-4}$	$4.6 \cdot 10^{-4}$	$6.4 \cdot 10^{-4}$	$1.6 \cdot 10^{-2}$	$2.1 \cdot 10^{-2}$	$4.5 \cdot 10^{-2}$	$5.7 \cdot 10^{-2}$	0.11	0.16
^{129}Xe	$-11.777 \cdot 10^6$	$3.2 \cdot 10^{-4}$	$6.4 \cdot 10^{-4}$	$8.9 \cdot 10^{-4}$	$2.3 \cdot 10^{-2}$	$4.5 \cdot 10^{-2}$	$6.3 \cdot 10^{-2}$	$7.9 \cdot 10^{-2}$	0.16	0.22
e^-	$-2.802 \cdot 10^{10}$	0.8	1.5	2.1	49	80	91	95	99.98	99.995

Table 1 Gyromagnetic ratios and spin polarizations of some nuclear spins and of the electron spin for different magnetic fields and temperatures. The table presents the polarizations at thermal equilibrium for different nuclei at 300K, 4.2K (liquid helium at ambient pressure) and 1.2K (lowest temperature available in our setup).

c. Principal DNP techniques

In 1953, Overhauser proposed a method for polarizing nuclear spins in metals by saturating the EPR line of the conduction electrons [5]. He observed an enhancement of the signal of the nuclei if the electronic transition is irradiated. The Overhauser effect is nowadays one of several "Dynamic Nuclear Polarization" (DNP) methods. The method relies on the hyperfine couplings between electrons and nuclear spins.

MAS DNP. DNP has found many applications in solid-state NMR. It is nowadays routinely performed under Magic Angle Spinning (MAS) conditions to study DNP enhanced NMR of solid samples doped with paramagnetic species (mostly free radicals). DNP is therefore performed while spinning the sample (typically between 10 to 100 kHz) at an angle 54.74° with respect to the external magnetic field. Commercial MAS-DNP work at temperatures usually $T \geq 100$ K (commercially available in Bruker) or $T \geq 85$ K [6] and work with a flow of gaseous nitrogen or helium. A prototype is working at temperature down to 30 K with helium [7].

Dissolution DNP. In 2003, the group of Klaes Golman invented Dissolution DNP (D-DNP) [8]. In this approach, the sample is polarized by DNP at low temperatures (usually around 1 K and 3.35 T) in the solid state and rapidly dissolved to a room temperature liquid with hot solvent, usually water, in the DNP magnet, and transferred to an NMR spectrometer or an MRI machine. This dissolution and transfer must be performed fast enough to preserve the hyperpolarization from relaxing back to Boltzmann's steady state.

Initially, D-DNP experiments were performed in a field of 3.35 T at a temperature of 1.2 K where the electron spin polarization is about 95 % [8]. Our group has shown that working at a higher field, currently 6.7 T [9], is beneficial for the DNP nuclear polarization, even if the electron spin polarization only increases from 95 % at 3.35 T to 99.89 % at 6.7 T. Currently, D-DNP at high fields is under development in several laboratories. This thesis is dedicated to Dissolution-DNP.

d. Electron Spin Resonance (ESR)

The DNP efficiency and the mechanisms depend of the nature of the free radical. The electron resonance, the spectral width, and the relaxation times are all important elements to understand DNP. The DNP process needs the saturation of the ESR line. By studying ESR, the saturation time constant

can be determined. Though the final aim is to study the nuclei, some characteristics of electronic resonance are relevant to understand the DNP process.

Similar to protons, electrons possess a $\frac{1}{2}$ spin but have a much higher gyromagnetic ratio ($-3 \cdot 10^{10} \text{ s}^{-1} \text{ T}^{-1}$), almost three orders of magnitude larger than for protons. This means that electrons resonate at a frequency of 188 GHz at 6.7 T (figure 4.B). Following Boltzmann's law, it appears that the electron spin polarization can approach unity for relatively moderate temperatures and magnetic fields (see Table 1). Historically, DNP for dissolution applications used a field of 3.35 T [8], so that a temperature of 1.2 K was necessary to reach an electron polarization of 95 %. Recently, Jannin et al. demonstrated that a higher field leads higher DNP efficiency at low temperatures [9]. One reason is the higher polarization of the electrons (near 100%) and get 100 % $P(e^-)$. By this same logic, a field of 9.4 T should be strong enough to allow use at 4.2 K (figure 4.A). This temperature is easier to get experimentally because it corresponds to the temperature of helium bath under atmospheric pressure, as explained in *Chapter 3.a.i, Part A*.

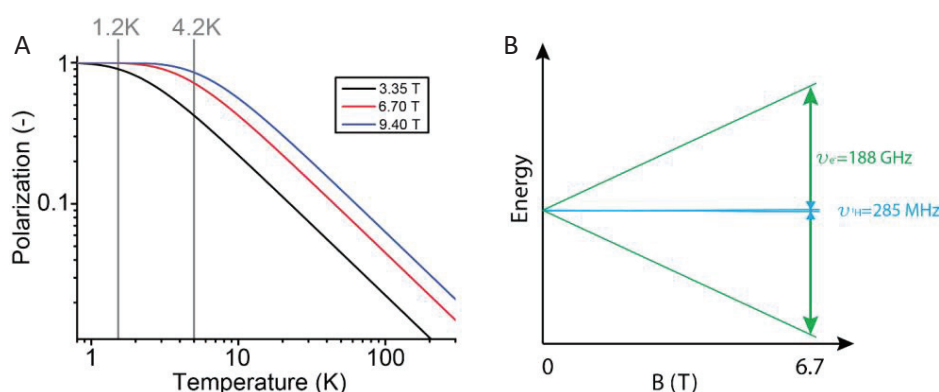


Fig. 4 A : polarization of electrons in fields of 3.35 T, 6.70 T or 9.4 T. It is interesting to note that the polarization at 9.40 T and 4.2 K is equal to the polarization at 3.35 T and 1.2 K. At 4.2 K, a simple helium Dewar could replace the setup with pumps. **B :** illustration of the Zeeman effect for electrons compared to protons.

i. Spectra of Radicals

D-DNP is traditionally performed by saturating the ESR transitions of narrow-line radicals such as Trityls [10]. In this thesis we exclusively work with nitroxide radicals. The EPR spectrum of nitroxides is much broader than the one of Trityl. This (inhomogeneous) broadening arises mainly from the g -anisotropy and the hyperfine coupling of the electron with ^{14}N , and also to a lesser extent from dipolar couplings between electrons (homogeneous broadening) (figure 5). This latter contribution becomes especially relevant at high electron spin concentrations. The homogeneous and inhomogeneous linewidths are

important parameters and influence which DNP mechanism may take place, as will be developed in Chapter 3.b.iii, Part A.

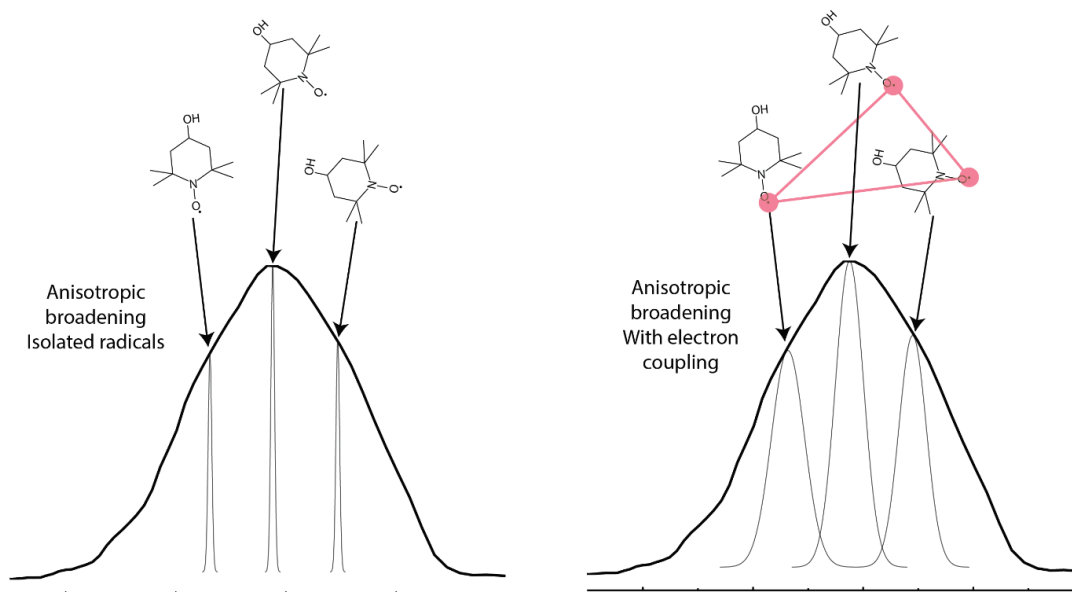


Fig. 5 Broad spectrum of TEMPOL radicals due to the anisotropic effect of ^{14}N nuclei in the molecule. The coupling between electrons broadens the spectrum even more.

Chapter 2: DNP effects as a function of the ESR lineshape, concentration, etc.

Below is a brief overview of the different DNP mechanisms that can take place in a DNP experiment, depending mainly on the features of the ESR spectrum (homogeneous or inhomogeneous linewidths)

a. Overhauser Effect

Initially only thought to exist in conducting media, DNP by Overhauser Effect in non-conducting solids was observed at around 100 K under MAS conditions [6] and in liquid state [11]. The effect appears when the microwave irradiation is applied at the ESR resonance $\omega_{MW} = \omega_e$. This effect relies on differences in relaxation rates across zero- and double-quantum transitions. The OE was observed with 6 1,3-bisdiphenylene-2-phenylallyl (BDPA) radicals and, to a lesser extent, with Trityl [12]. We are currently studying this effect at 1.2 K and 6.7 T in our laboratory. Figure 6 shows the DNP spectrum (DNP enhancement of the protons as a function of the microwave frequency) for a sample consisting in a glass-forming glycerol/water mixture containing sulfonated BDPA. The spectrum clearly shows a central enhancement lobe that is characteristic of the Overhauser effect.

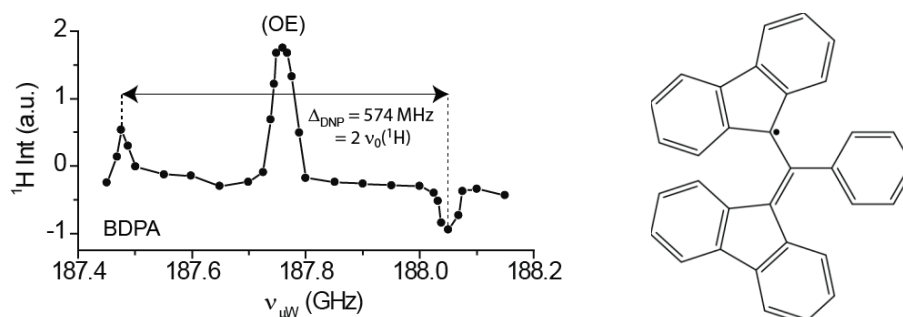


Fig. 6 Left: Microwave frequency profile of DNP enhancement of protons. Right: Structure of 1,3-bisdiphenylene-2-phenylallyl (BDPA). Sulfonated BDPA possesses a SO_3Na group attached to the aromatic ring for a better dissolution in polar solvents. One can observe both the Overhauser Effect (OE) and the Solid Effect (SE).

b. Solid Effect

In the same figure 6 one can also observe two enhancement lobes separated by twice the proton Larmor frequency. These are due to the Solid Effect (SE)[13-19]. It requires a single electron coupled with a single nuclear spin. The hyperfine structure can be represented by four energy levels (see figure 7), note that the figure is not to scale since the electron Zeeman splitting appears at a few hundreds of GHz, while the nuclear splitting occurs at a few hundreds of MHz). The solid effect DNP process happens when the spin system is irradiated by microwaves with a frequency near $\omega_{MW} = \omega_e \pm \omega_n$. This corresponds to forbidden transitions, more precisely to double- or zero-quantum transitions. SE therefore needs more microwave energy than the Overhauser effect, which arises from the saturation of an allowed electron spin transition. A positive nuclear polarization (i.e., when the lower energy nuclear state is more populated than the higher energy state) is obtained for $\omega_{MW} = \omega_e - \omega_n$. Inversely a negative polarization is obtained for $\omega_{MW} = \omega_e + \omega_n$.

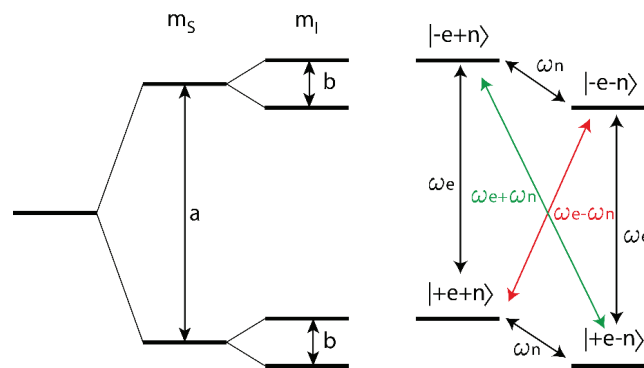


Fig. 7 Left: hyperfine splitting with (a) the electron splitting and (b) the nuclear splitting. For clarity, the figure is not drawn to scale. Right: hyperfine structure with four energy levels. The conditions for SE are $\omega_{MW} = \omega_e \pm \omega_n$. The OE effect is possible if the relaxation rate across the $|-e - n\rangle \rightarrow |+e + n\rangle$ transition is not equal to $|-e + n\rangle \rightarrow |+e - n\rangle$ transition.

In practice, the Solid Effect (SE) is rarely observed. The electron ESR spectrum needs to be very narrow $\Delta\omega_e < \omega_n$ for it to be observed in a resolved manner. However, the SE mechanism is observed for ^1H polarization with Trityl, though it is relatively inefficient.

c. Cross Effect

The Cross Effect (CE) [19-23] involves two coupled electron spins and one nuclear spin. The two electrons must be dipolar coupled, and their electron spin resonance frequencies should be separated by the nuclear Larmor frequency $|\omega_{e1} - \omega_{e2}| = \omega_n$. This mechanism is usually more efficient than SE because it only involves saturating allowed electron spin transitions. In practice, an electron spin concentration of at least 10 mM is required to obtain sufficiently large electron-electron dipolar couplings. The spin system is irradiated by microwaves at a frequency equal to the one of the electron spin resonances

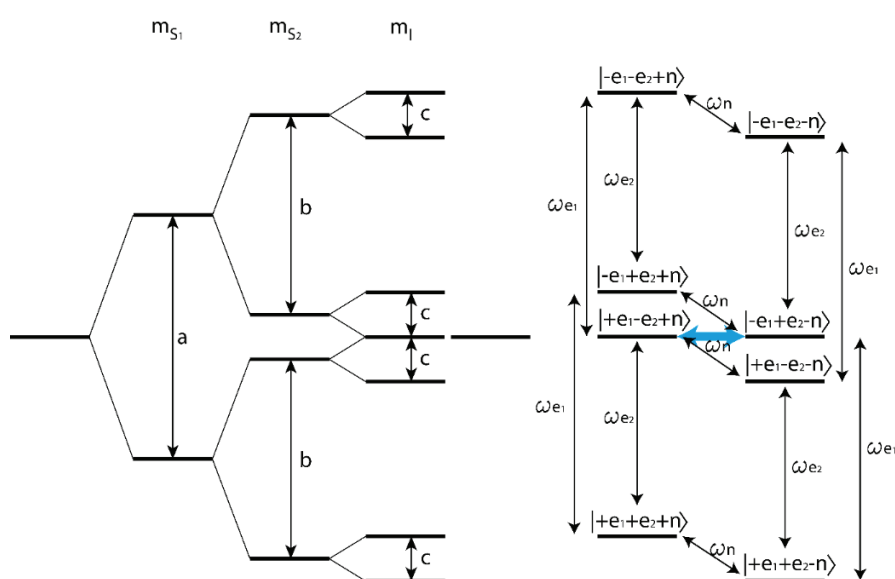


Fig. 8 Left: hyperfine splittings with (a) and (b) the electron splitting and (c) the nuclear splitting. Here again for clarity the figure is not drawn to scale. Right: Hyperfine structure for electron-electron-nucleus system. The condition to have an efficient CE is to have two degenerate energy levels. This condition is matched if $|\omega_{e1} - \omega_{e2}| = \omega_n$. In blue, the arrow represents the flip-flop transition. CE is particularly efficient because this transition is allowed.

The Cross Effect requires ESR resonances that are separated by the nuclear Larmor frequency. In practice, this is achieved with radicals with broad ESR lines. Nitroxides are good candidates for this approach, with an ESR spectrum that is broader than the proton Larmor frequency.

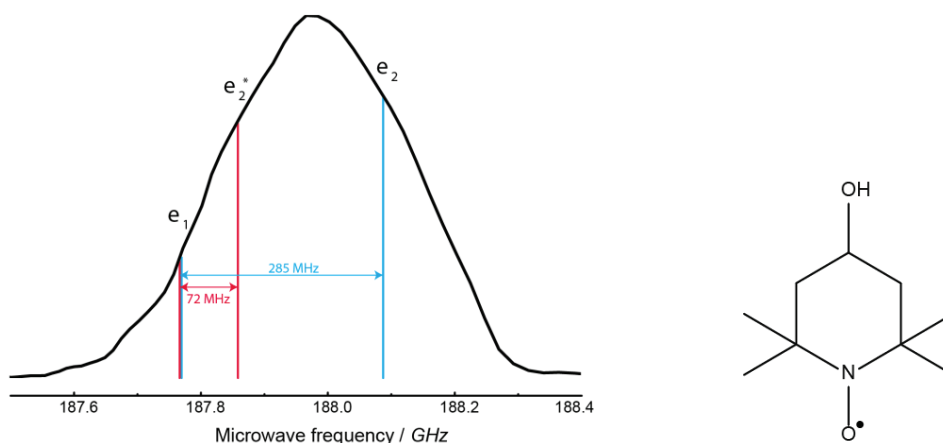


Fig. 9 The TEMPOL radical is a good candidate for CE because of its broad ESR spectrum. Different pairs of electrons can be found to match the CE condition.

d. Thermal Mixing

DNP by Thermal Mixing (TM) [24-32] also requires a broad ESR line (possibly inhomogeneous) and a substantial electron spin concentration above 10 mM so as to yield significant electron-electron dipolar couplings. The electron broadening is caused by the continuous (or quasi-continuous) energy-level distribution which arises from the anisotropy of the ESR line and from electron-electron dipolar couplings. At thermal equilibrium, the distribution of the populations of the states is governed by Boltzmann's law. When MW-irradiation is applied, the system is perturbed and obeys a different distribution. This new distribution is usually described by using the concept of spin temperature [33-35]. At thermal equilibrium, $T_{spin} = T_{bulk}$, but during DNP, $T_{spin} \neq T_{bulk}$. The spin temperature can be either positive or negative. The nuclear system is said to be "in contact" with the system of electrons through electron-electron-nuclear cross-relaxation events. This is analogous to the Cross Effect, but here, all the electron-electron couplings satisfying $|\omega_{e1} - \omega_{e2}| = \omega_n$ can contribute to the DNP effect. Therefore, when the condition $\omega_n < \Delta\omega_e$ is fulfilled, the nuclear spin temperature tends to equilibrate with the spin temperature of the electron system.

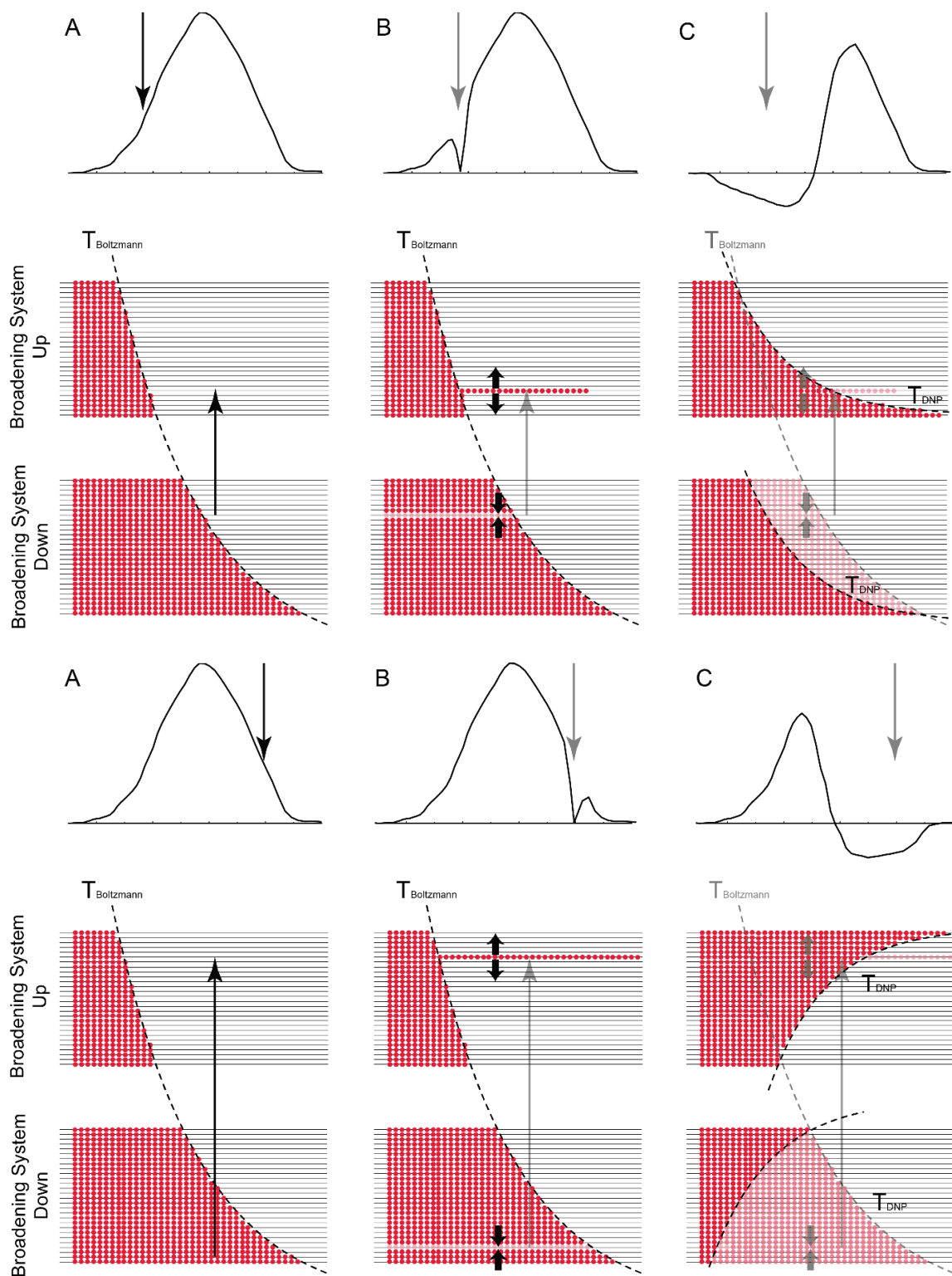


Fig. 10 Schematic representation of thermal mixing: upper pictures for positive irradiation, lower pictures for negative irradiation. This effect needs a multi-level energy structure. It is a thermodynamic representation of a macroscopic view. The distribution follows Boltzmann's rule in the initial state. Firstly the system is irradiated with MW which acts as a pump between the two systems. Secondly, spin diffusion populates the other states in the system. Finally the system gets a distribution that is totally different from the initial Boltzmann distribution. This new distribution can be described thanks to a spin temperature. By interacting with the lattice by exchanging phonon, the nuclear spin system tends to have a similar temperature.

TM happens in two steps: first the electron system acquires a new spin temperature under microwave irradiation. Depending on the microwave frequency, the system can reach a positive or negative spin temperature. In a second step, cross relaxation between two electron spins and one nuclear spin leads to the equilibration of the spin temperatures of the electronic and nuclear systems. The final spin temperature is the same for all nuclear spins, leading to a polarization roughly proportional to the gyromagnetic ratios. An interesting feature of the TM is that the DNP spectra are similar for ^1H or ^{13}C , with maxima at the same point [24, 25].

e. The importance of Spin Diffusion

Nuclear Spin diffusion (SD) is a process by which polarization can be exchanged spontaneously between spins by dipolar couplings, and therefore transported across space. During DNP, SD transfers the nuclear spin polarization away from the electron spins. Indeed most of the nuclear spins in a DNP sample are polarized by SD-assisted DNP, and not directly by the electrons. The nearest spin near electronic spin cannot process for SD, this phenomena is known as spin diffusion barrier or bleaching barrier [26]. The SD happens beyond this barrier which corresponds to about 1-1.5 nm. Figure 11 gives a visual representation of the importance of SD for the bulk polarization of the sample.

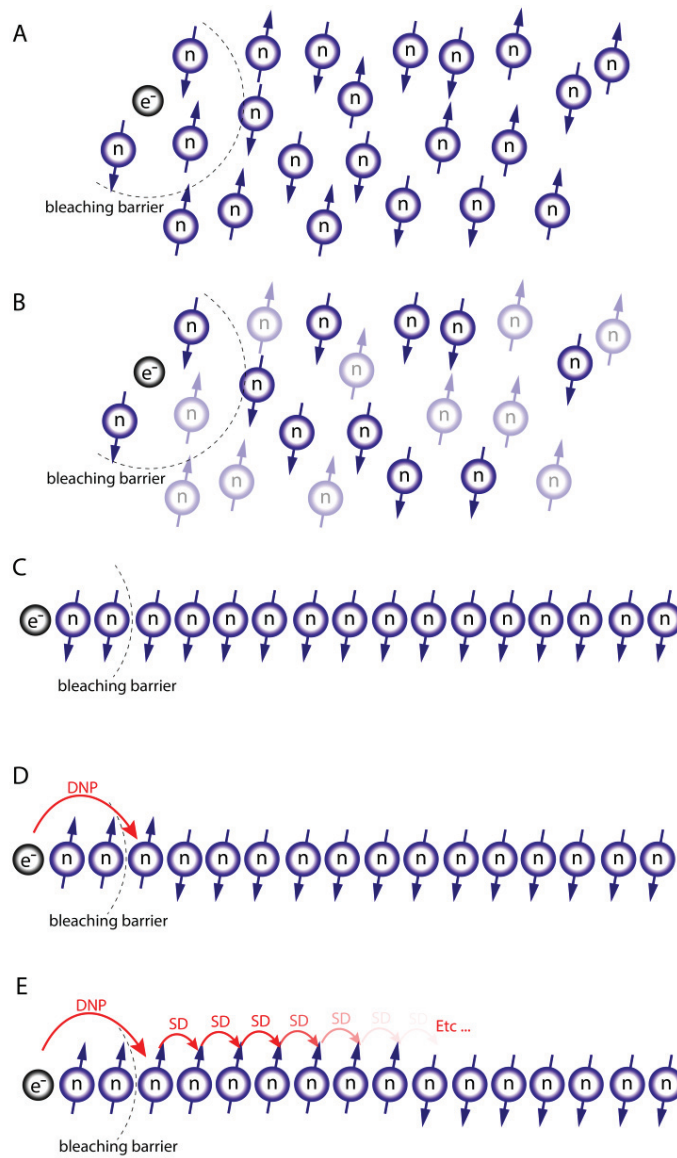


Fig. 11 (A) The solution contains approximately an equal number of spins up and spins down. (B) Considering only the spins down, all the spins up are ignored, the positive irradiation tends the system to get a full spin up state by changing the state of each spin down. (C) Illustration of all the spins down in a line. (D) The DNP process happens near the electron but the spin diffusion (SD) can process after the diffusion barrier or bleaching barrier (E).

Chapter 3: Conventional dissolution DNP experiments

The work presented in this thesis is a further development of the invention of Klaes Golman, Jan-Henrik Ardenkjaer-Larsen and colleagues [8], based on a home-built polarizer developed at EPFL in collaboration with the Paul Scherrer Institute [36, 37]. A basic D-DNP setup comprises two machines; the polarizer where the nuclear spins are polarized, with a superconducting magnet, a cryostat and a MW source, and a standard NMR or MRI machine where the hyperpolarized experiment is performed in the liquid state. The dissolution system usually consists of a dissolution stick that can be rapidly coupled to the sample for injecting hot solvent. The dissolved sample is then transferred with pressurized gas to the NMR or MRI machine prior to injection in a tube, a phantom or a living animal. The next section presents the standard setup already used in our lab, like the cryostat including the system of pumps to reach adequate temperature and the microwaves source which include the frequency modulation [38]. The microwaves sources, the pumps but also the dissolution process (presented in Part B) are totally managed thanks to a LabVIEW software.

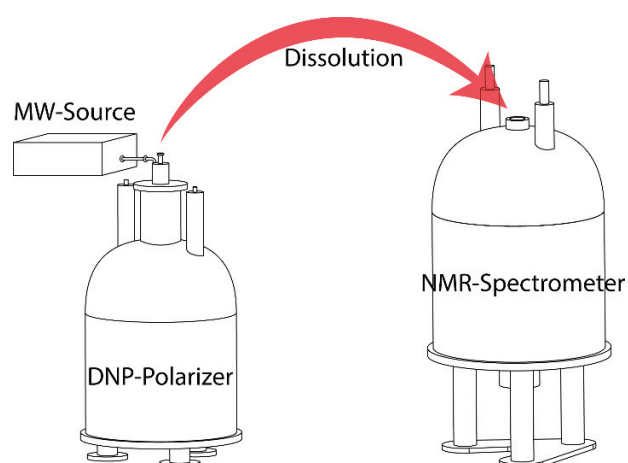


Fig. 12 General schema for D-DNP. The polarization is achieved in a machine that is separated from the NMR spectrometer. The DNP process happens at low temperature in a solid. To obtain a liquid and transfer it to an NMR analyzer, it is necessary to melt the sample. The field of the NMR analyzer is not relevant. Depending on the kind of analysis, especially for optimal chemical shift dispersion, it is possible to use 800 MHz or higher. Note that high field NMR spectrometers will have similar signal intensities as lower field spectrometer, since the signal depends only of the DNP process.

a. D-DNP hardware

The D-DNP setup in our laboratory is composed of a superconducting magnet (a 7 T wide-bore magnet from Oxford Instrument used at 6.7 T), in which a continuous flow He-4 cryostat is inserted (designed and constructed by the low-temperature facility at PSI). The outer vacuum chamber of the cryostat is evacuated with a turbopump (Pfeiffer Vacuum) to guarantee a vacuum of $< 10^{-5}$ mBar. The helium bath can be pumped by two pumps in series (Leybold RUVAC WAU 251 and Leybold TRIVAC D 65 B) to obtain a pressure controlled by a butterfly valve, down to a pressure of 81 Pa (0.81 mBar). The temperature can go down to 1.2 K. The cryostat is coupled to a 100 L helium Dewar for continuous refill. The helium is transferred from the helium Dewar to a phase separator connected to the sample space by two capillary tubes equipped with manually operated needle valves. We constantly monitor the pressure, temperature and helium level (two sensors near the sample and one near the phase separator). The interfacing is running under Labview (national Instruments). Helium gas is recovered and re-liquefied. Three cryostat modes can be used for routine experiments.

4 K or stand-by mode: the sample space is slightly above atmospheric pressure, connected to the helium recovery line. The two needle valves are closed and helium is pumped to have a very small flux of about 3 liters of gas per minute from the Dewar to the phase separator to keep the separator temperature below 40 K.

1.2 K mode: The sample space is pumped down to 1 mBar. The needle valves are closed.

Filling mode: The helium flux in the phase separator is increased to 10 L/min so as to pump liquid helium from the Dewar. One needle valve is opened and the sample space is pumped down to a pressure of 800 mBar to let liquid helium refill through the needle valve.

It is also possible to use this setup with a nitrogen Dewar to work with liquid nitrogen at 77 K. The nitrogen passes through the same path as the helium.

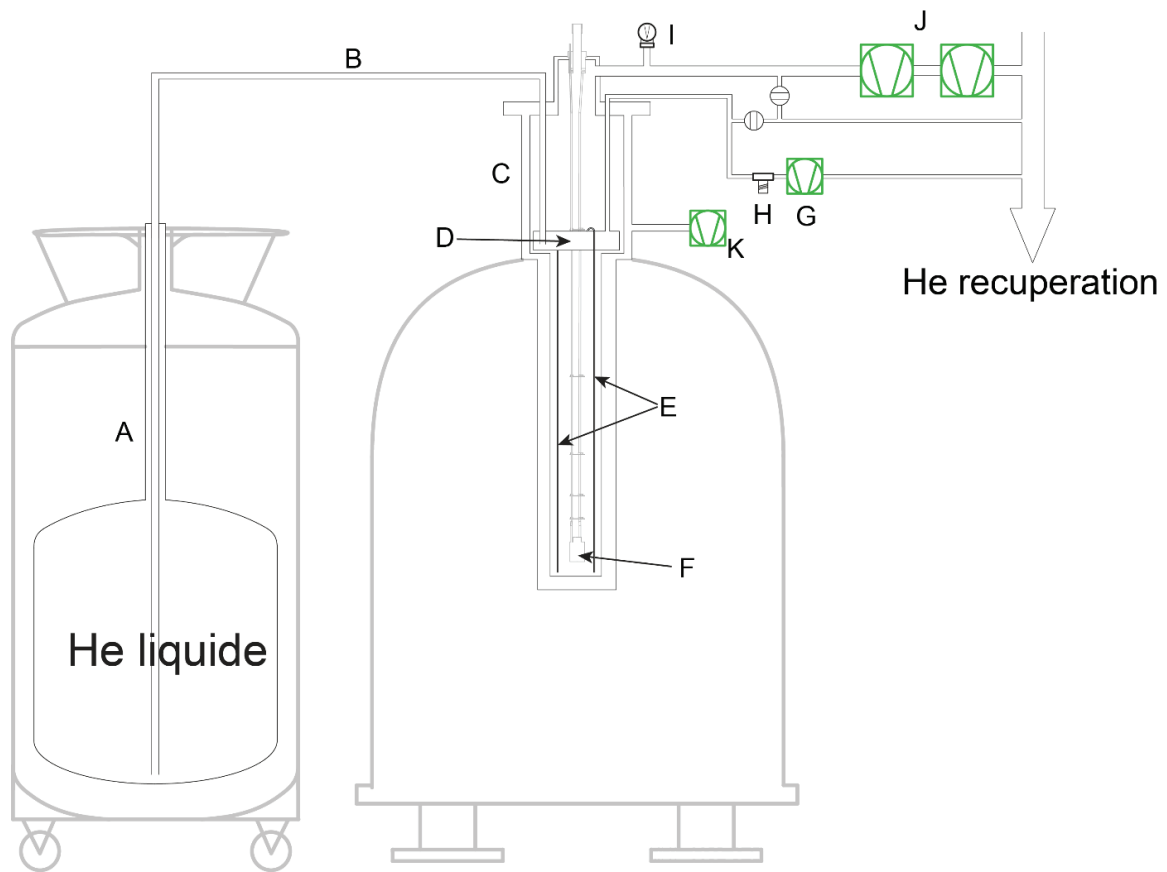


Fig. 13 Complete cooling setup with helium tank (A), cryostat (C) and pumps (J, G and K). The Dewar (A) contains liquid helium at ambient pressure. Through an isolated transfer line (B) the helium arrives in the separator room (D). The flux of helium is regulated by a flux measurement (H) and a pump (G). By managing the pressure in sample space (F) with two pumps (J) and a pressure measurement (I), the liquid helium is pumped through capillary tube (E). A turbo pump (K) maintains the vacuum in the isolated cryostat.

i. Temperature management

The temperature of a helium bath can be controlled by modifying the helium vapor pressure. This relationship was studied experimentally by Durieux and Rusby [39]. Our experiment take place between 4.2 K, the temperature at atmospheric pressure, and 1.2 K, the temperature with maximal pumping (1 mBar).

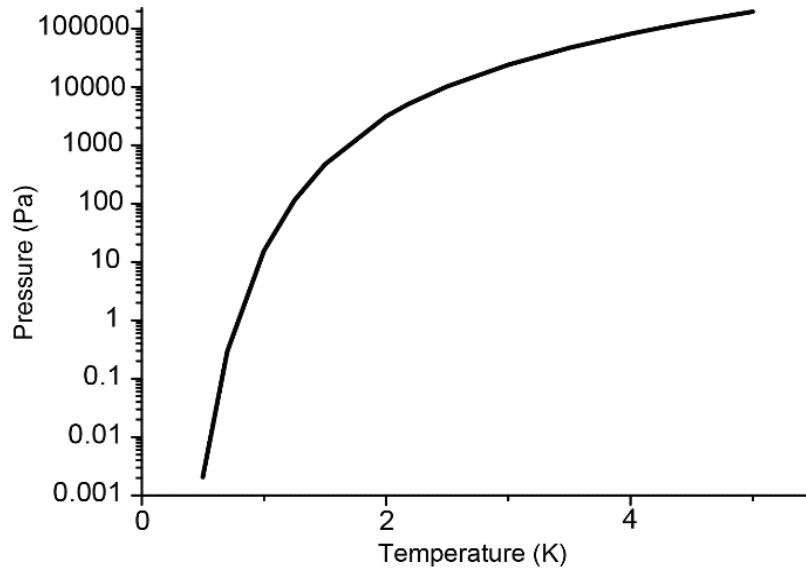


Fig. 14 Durieux and Rusby empirically studied in 1982 the relationship between the pressures above a helium bath and its temperature. This relation is used here to control the temperature in the sample space. A temperature of 1.2 K can be reached in the DNP polarizer.

ii. *Microwave irradiation*

DNP is performed by microwave irradiation at frequencies $187.5 < f_{\mu\text{w}} < 188.5$ GHz, and with a maximum power $P_{\mu\text{w}} \approx 87.5$ mW at the input of the DNP insert. Microwaves are generated with a source (Elva VCOM-10/0.5/94/400) delivering up to $P_{\mu\text{w}} \approx 400$ mW at $f_{\mu\text{w}} = 94$ GHz \pm 250 MHz at the WR-10 output in the rectangular fundamental TE₁₀ mode. At this stage the frequency is controlled directly by a voltage controlled oscillator unit (VCO) by a constant or modulated voltage (Stanford Research Systems DS345). The voltage source combined with the Elva VCO enables fast (up to 10 MHz) and broad frequency modulation over a range of ± 500 MHz. A doubler (Virginia Diode D200) is used to double the microwave frequency, thus providing $f_{\mu\text{w}} = 188 \pm 0.5$ GHz with $P_{\mu\text{w}} \approx 87.5$ mW at the WR-5 waveguide output in the TE₁₀ mode. A commercial rectangular-to-circular transition device (Quinstar QWC series) is placed directly after the doubler to convert the rectangular TE₁₀ mode to a circular TE₁₁ mode. The microwave beam propagates in an oversized stainless steel waveguide with a 4.5 mm diameter equipped with two home-built gold-plated miter bends. The microwave beam is directed horizontally to the side of the sample.

b. Practical DNP experiment

During the last decade, D-DNP experiments have been performed mainly by direct ^{13}C polarization with trityl radicals, and in a field of 3.35 T at a temperature of 1.2 K. When the DNP sample is suitably prepared, trityl can lead to ^{13}C polarizations as high as $P(^{13}\text{C}) = 36\%$ [10] under these conditions. By comparison, the nitroxide radical TEMPOL (4-hydroxy-2,2,6,6-tetramethylpiperidin-1-oxyl) only gives $P(^{13}\text{C}) = 10\%$ ^{13}C polarization [40]. However, TEMPOL is very efficient for ^1H polarization, both in terms of the final value ($P(^1\text{H}) = 40\%$) and of the build-up time constant ($\tau_{\text{DNP}}(^1\text{H}) = 70\text{ s}$) [41].

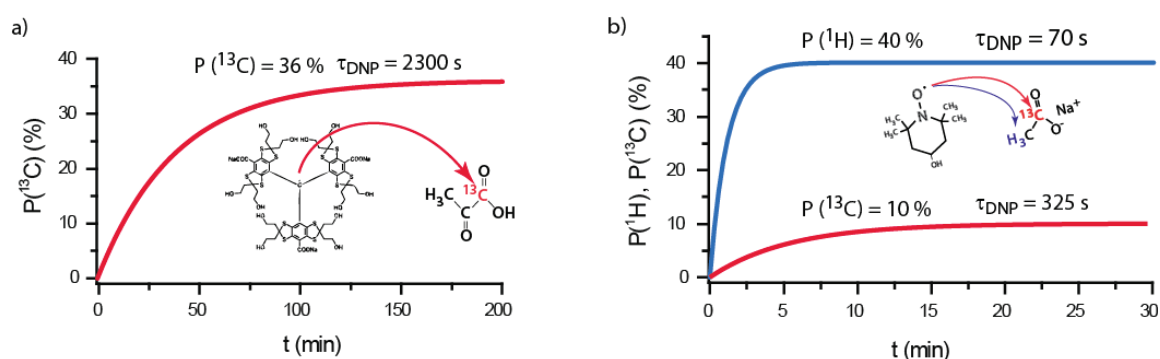


Fig. 15 a) Typical DNP build-up of a ^{13}C signal with trityl radicals. The characteristic time to reach a polarization of 36% is 38 min. b) Typical DNP build-up with TEMPOL radicals for ^1H (blue) and ^{13}C (red). ^{13}C reaches only 10% but in a short time of 5 min. It appears that TEMPOL radicals are very efficient for ^1H polarization since one can reach a polarization of 40% in a build-up time of only 1.2 min.

Figure 15 shows how the ^1H DNP build-up with TEMPOL is very fast if compared to ^{13}C . Therefore the rest of this thesis principally focusses on ^1H polarization, followed by cross-polarization (CP) to other low-gamma nuclear spins. We will see later how CP can be used to transfer the high ^1H polarization to other nuclei (^{13}C , ^{15}N , ^{29}Si ...). This strategy is motivated not only by the improved DNP efficiency (high polarization in short build-up time) but also for economical reason. TEMPOL is in fact rather inexpensive (ca. 20 CHF per gram).

i. DNP at 3.35 T with TEMPOL radical

Table 2 gives the polarization reached by DNP in a 3.35 T magnetic field at different temperatures. The sample was a 3 M $1\text{-}^{13}\text{C}$ labeled acetate solution with 30 mM TEMPOL a (2:1) mixture of 100% deuterated water and ethanol [41]. At lower temperatures, DNP becomes more efficient partly thanks to the higher electron spin polarization. At 1.2 K, $P_e = 95\%$ (Table 1, Chapter 1.b).

T (K)	$P_{\text{DNP}}(^1\text{H})$ (%)	$\tau_{\text{DNP}}(^1\text{H})$ (s)	$P_{\text{DNP}}(^{13}\text{C})$ (%)	$\tau_{\text{DNP}}(^{13}\text{C})$ (s)
1.2	40	70	10	324
2.2	24	57	6	267
3	12	32	3	222
4.2	8	22	2	158

Table 2 Polarizations achieved by direct irradiation at 3.35 T for ^1H and ^{13}C in a sample of 3 M $1\text{-}^{13}\text{C}$ labeled acetate with 30 mM TEMPOL in a (2:1) mixture of 100% deuterated water and ethanol

ii. DNP at 6.7 T with TEMPOL radicals

At 6.7 T, TEMPOL becomes even more efficient for ^1H DNP. At 1.2 K we routinely measure ^1H polarizations higher than 90 %. See table 3 for results measured on a sample of 3 M $1\text{-}^{13}\text{C}$ labeled pyruvate with 50 mM TEMPOL in a (2:1) mixture of 100% deuterated water and ethanol [9].

T (K)	$P_{\text{DNP}}(^1\text{H})$ (%)	$\tau_{\text{DNP}}(^1\text{H})$ (s)	$P_{\text{DNP}}(^{13}\text{C})$ (%)	$\tau_{\text{DNP}}(^{13}\text{C})$ (s)	$\epsilon_{\text{DNP}}(^1\text{H}/^{13}\text{C})$
1.2	91	150	36	1980	2.5
2.2	60	52	22.5	1010	2.6
4.2	25	25	5.5	359	4.5

Table 3 Polarizations achieved by direct irradiation at 6.7 T for ^1H and ^{13}C for a sample of 3 M $1\text{-}^{13}\text{C}$ labeled pyruvate with 50 mM TEMPOL in a (2:1) mixture of 100% deuterated water and ethanol. These measurements were done with direct MW irradiation applied to a sample without methyl groups.

iii. Effect of radical concentration

The concentration of unpaired electrons has a dramatic effect on the DNP mechanism and on its efficiency. Figure 16 shows the DNP spectrum of both ^1H and ^{13}C for different radical concentrations. At low concentrations (10 mM), we recognize that DNP is dominated by CE since the two extrema are separated either by the ^1H Larmor frequency $\Delta_{\text{max}} = \omega, = 285.23 \text{ MHz}$ at 6.7 T, or by the ^{13}C Larmor frequency $\Delta_{\text{max}} = \omega, = 71.73 \text{ MHz}$ at 6.7 T. On the other hand, at higher concentrations (50 mM), the DNP spectra for ^1H and ^{13}C are identical, therefore TM must be the dominant mechanism.

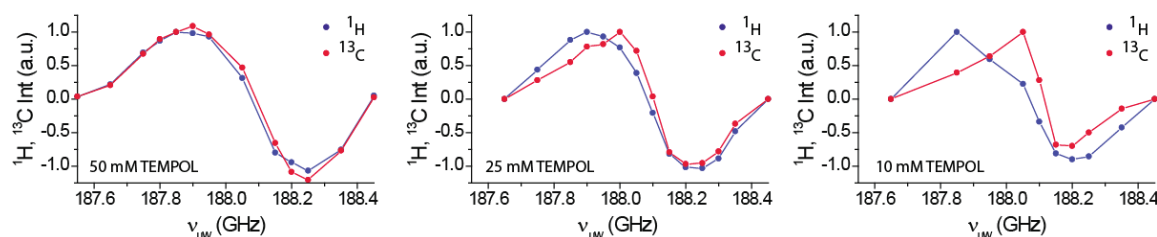


Fig. 16 DNP spectrum for different radical concentrations. At high concentrations, the predominant mechanism is TM, and the DNP spectrum does not depend on the nature of nuclei. At low concentration, CE is predominant [1].

iv. Effect of MW Frequency Modulation

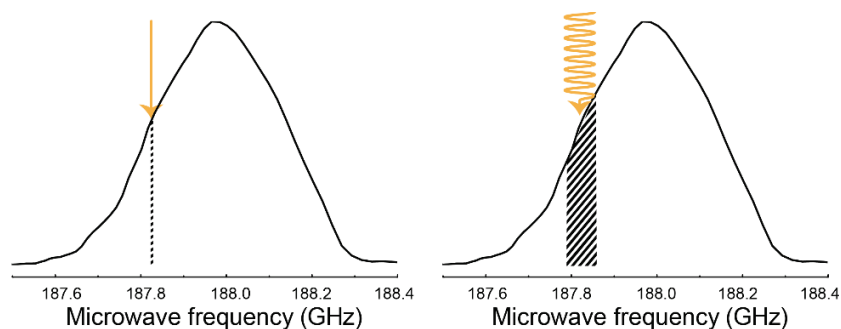


Fig. 17 The modulation allows one to exploit a broader range of the ESR spectrum of the radicals.

Lowering the concentration of the polarizing agent results in weaker electron-electron dipolar couplings, as the inter-electron distances increase. In such cases, electron-electron spectral spin diffusion is ineffective, and a monochromatic irradiation only saturates a small fraction of the electron spin resonance. To increase the DNP efficiency, one way is to irradiate a wider range of the ESR spectrum to involve more electron spins. This can be done by applying a modulation of the irradiation

frequency of the MW source [38]. This strategy increases significantly the polarization for low electron spin concentrations. At high concentrations, the benefit is lower, as electron-electron spectral spin diffusion is more efficient. Figure 18 illustrate the benefits due to MW modulation if the CE mechanism is predominant.

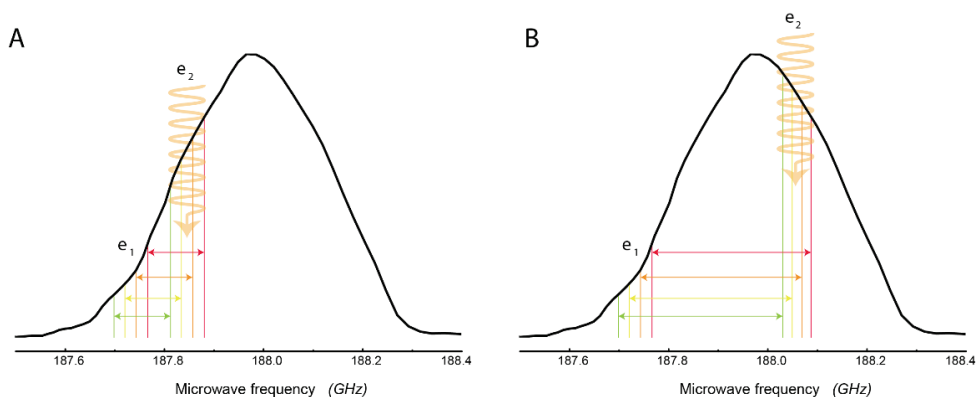


Fig. 18 The effects of microwave modulation depend on the concentration of the radicals which determines the efficiency of electron-electron spin diffusion. More pairs of electrons are exploited when using microwave modulation if CE is the dominant mechanisms. (A) Illustration of the benefit of modulation in a system with ^{13}C coupling and (B) for ^1H coupling.

Table 4 shows proton DNP results with and without frequency modulation in a 10:40:50 v/v/v $\text{H}_2\text{O}:\text{D}_2\text{O}:\text{d}_8\text{-glycerol}$ mixture with 10, 25 and 50 mM TEMPOL at 1.2 K. The frequency of modulation is $f_{\text{mod}} = 10$ kHz. Sinusoidal or triangular frequency modulation has similar effects on DNP efficiencies. For positive polarization $P^+(\text{}^1\text{H})$ or negative polarization $P^-(\text{}^1\text{H})$, the microwave frequencies were found to be optimal at $f_{\mu\text{w}} = 187.85$ and 188.3 GHz respectively. The monochromatic irradiation is defined by an irradiation without modulation (spectral purity of our microwave source ca. $\Delta f_{\mu\text{w}} < 10$ kHz). For frequency modulation, we experimentally found an optimal amplitude of $\Delta f_{\mu\text{w}} = 100$ MHz with a modulation frequency of $f_{\text{mod}} = 10$ kHz.

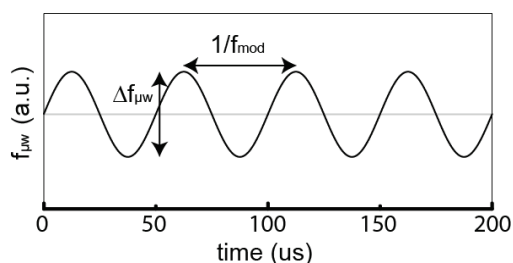


Fig. 19 Characteristics of the microwave modulation.

Frequency modulation provides a way of increasing the proton polarization $P(\text{}^1\text{H})$, while simultaneously increasing the DNP build-up rate $R_{\text{DNP}}(\text{}^1\text{H}) = 1/\tau_{\text{DNP}}(\text{}^1\text{H})$. The effect of frequency

modulation is hardly remarkable at higher radical concentrations around 50 mM, but it is more pronounced if the radical concentration is decreased to 25 or 10 mM [38]. Table 4 shows the benefits of microwave frequency modulation.

[TEMPOL] (mM)	Modulation	P ⁺ (¹ H) (%)	$\tau_{\text{DNP}}^+(\text{}^1\text{H})$ (s)	P ⁻ (¹ H) (s)	$\tau_{\text{DNP}}^-(\text{}^1\text{H})$ (s)
10	With	14.5*	2600 ± 1000**	-21.1*	2500 ± 1000**
	Without	0.9*	NA***	-1.2*	NA***
25	With	57.3	159 ± 1.8	-60.7	185 ± 2
	Without	9.3*	9000 ± 2000**	-29.5	625 ± 11
50	With	61.3	108 ± 1.6	-63.3	152.2 ± 2
	Without	21.9	338 ± 7	-43.7	218 ± 4

Table 4 Polarizations obtained by DNP with and without microwave modulation for different concentrations of paramagnetic agents (PA). The DNP maximum was not reached; the polarization shown was achieved after 20 min of microwave irradiation. Fits have large uncertainties because only the first 20 min of the DNP build-up curve were recorded. Estimates of the build-up times are not available because of poor fits.

c. Problems addressed in this thesis

There is no need to show that the D-DNP is a powerful tool for NMR analysis. The future of NMR spectrometry and MRI will be greatly helped by DNP. The current state of development of our DNP setup gives very high polarizations in the solid state. Although polarization records have been established in liquid state, much of the DNP enhancement is lost during sample transfer. The presence of radicals, which is the foundation of DNP, becomes a disadvantage as soon as the dissolution process is launched. Effectively the presence of radicals, especially at low fields, dramatically enhances the spin-lattice relaxation rate $1/T_1$. One solution is presented in this thesis to overcome this problem. A magnetic tunnel was built to keep the sample in a high field during its passage through the laboratory. The development of instrumentation plays a central role in this thesis. First, the development of a Cross Polarization (CP) probe based on an older model used previously in our lab is described. RF coils were developed for different nuclei. The MW setup was also studied to optimize irradiation across the sample volume within the constraints of a DNP dissolution facility.

An ESR probe was built to measure the electronic spectrum *in situ*, at a field of 6.7 T and at low temperatures from 1.2 K to 4.2 K. This measurement is not only used to get spectra but also to measure the characteristic time constants of the electronic spins, the time of saturation during MW irradiation and the electron relaxation time.

Finally to overcome the problem of persistent radicals in solution, a setup was built to study DNP by MW irradiation of optically excited triplet states at high magnetic fields (6.7 T) and low temperatures (from 1.2 K to 4.2 K in a helium bath. or at 77 K in liquid nitrogen). A laser was coupled to an optical fiber to guide intense visible light to the sample space. Unfortunately no positive results could be obtained so far with our system.

A non-exhaustive list of applications is presented in the last part of this thesis demonstrating the benefits of the developed setup. The magnetic tunnel is particularly beneficial for ^1H DNP. Cross polarization from ^1H to ^{13}C has been used not only for ^{13}C -labeled molecules but also for ^{13}C in 1.1% natural abundance.

References

1. Bornet, A. De l'usage des protons hyperpolarisés pour augmenter la sensibilité de la RMN, **2015**, PhD Thesis, Ecole Polytechnique Fédérale de Lausanne.
2. Zeeman, P. *Astrophysical Journal*, **1897**, 5,332.
3. Kiyoshi, T.; Otsuka, A.; Kosuge, M.; Yuyama, M.; Nagai, H.; Matsumoto, F. *Fusion Engineering and Design*, **2006**, 81(20-22),2411-2415.
4. Gan, Z.H.; Gor'kov, P.; Cross, T.A.; Samoson, A.; Massiot, D. *Journal of the American Chemical Society*, **2002**, 124(20),5634-5635.
5. Overhauser, A.W. *Physical Review*, **1953**, 92(2),411-415.
6. Pike, K.J.; Kemp, T.F.; Takahashi, H.; Day, R.; Howes, A.P.; Kryukov, E.V.; MacDonald, J.F.; Collis, A.E.C.; Bolton, D.R.; Wylde, R.J.; Orwick, M.; Kosuga, K.; Clark, A.J.; Idehara, T.; Watts, A.; Smith, G.M.; Newton, M.E.; Dupree, R.; Smith, M.E. *Journal of Magnetic Resonance*, **2012**, 215,1-9.
7. Lee, D.; Bouleau, E.; Saint-Bonnet, P.; Hediger, S.; De Paepe, G. *Journal of Magnetic Resonance*, **2016**, 264,116-124.
8. Ardenkjaer-Larsen, J.H.; Fridlund, B.; Gram, A.; Hansson, G.; Hansson, L.; Lerche, M.H.; Servin, R.; Thaning, M.; Golman, K. *Proceedings of the National Academy of Sciences of the United States of America*, **2003**, 100(18),10158-10163.
9. Jannin, S.; Bornet, A.; Melzi, R.; Bodenhausen, G. *Chemical Physics Letters*, **2012**, 549,99-102.
10. Johannesson, H.; Macholl, S.; Ardenkjaer-Larsen, J.H. *Journal of Magnetic Resonance*, **2009**, 197(2),167-175.
11. van Bentum, P.J.M.; van der Heijden, G.H.A.; Villanueva-Garibay, J.A.; Kentgens, A.P.M. *Physical Chemistry Chemical Physics*, **2011**, 13(39),17831-17840.
12. Haze, O.; Corzilius, B.; Smith, A.A.; Griffin, R.G.; Swager, T.M. *Journal of the American Chemical Society*, **2012**, 134(35),14287-14290.
13. Jeffries, C.D. *Physical Review*, **1957**, 106(1),164-165.
14. Abragam, A.; Proctor, W.G. *Comptes Rendus Hebdomadaires Des Seances De L Academie Des Sciences*, **1958**, 246(15),2253-2256.
15. Borghini, M.; Abragam, A. *Comptes Rendus Hebdomadaires Des Seances De L Academie Des Sciences*, **1959**, 248(12),1803-1805.
16. Leifson, O.S.; Jeffries, C.D. *Physical Review*, **1961**, 122(6),1781.
17. Schmutge, T.J.; Jeffries, C.D. *Physical Review*, **1965**, 138(6A),1785.
18. Hovav, Y.; Feintuch, A.; Vega, S. *Journal of Chemical Physics*, **2011**, 134(7).
19. Hu, K.N.; Debelouchina, G.T.; Smith, A.A.; Griffin, R.G. *Journal of Chemical Physics*, **2011**, 134(12).
20. Hwang, C.F.; Hill, D.A. *Physical Review Letters*, **1967**, 18(4),110-&.
21. Kessenikh, A.V.; Lushchikov, V.I.; Manenkov, A.A.; Taran, Y.V. *Soviet Physics-Solid State*, **1963**, 5(6),1191-1193.
22. Kessenikh, A.V.; Manenkov, A.A.; Pyatnitskii, G.I. *Soviet Physics-Solid State*, **1964**, 6(3),641-643.
23. Hovav, Y.; Feintuch, A.; Vega, S. *Journal of Magnetic Resonance*, **2012**, 214,29-41.
24. Provotorov, B.N. *Soviet Physics Jetp-Ussr*, **1962**, 14(5),1126-1131.
25. Provotorov, B.N. *Soviet Physics Jetp-Ussr*, **1962**, 15(3),611-614.
26. Abragam, A.; Goldman, M. *Reports on Progress in Physics*, **1978**, 41(3),395-467.
27. Abragam, A.; Goldman, M., *Nuclear magnetism : order and disorder*. The International series of monographs on physics. 1982, Oxford

28. Atsarkin, V.A.; Rodak, M.I. *Uspekhi Fizicheskikh Nauk*, **1972**, 107(1),3.
29. Atsarkin, V.A. *Uspekhi Fizicheskikh Nauk*, **1978**, 126(1),3-39.
30. Borghini, M. *Physical Review Letters*, **1968**, 20(9),419.
31. Ardenkjaer-Larsen, J.H.; Macholl, S.; Johannesson, H. *Applied Magnetic Resonance*, **2008**, 34(3-4),509-522.
32. Jannin, S.; Comment, A.; van der Klink, J.J. *Applied Magnetic Resonance*, **2012**, 43(1-2),59-68.
33. Abragam, A.; Proctor, W.G. *Physical Review*, **1958**, 109(5),1441-1458.
34. Goldman, M., *Spin temperature and nuclear magnetic resonance in solids*. The International series of monographs on physics. 1970, Oxford,: Clarendon Press. ix, 246 p.
35. Redfield, A.G. *Physical Review*, **1955**, 98(4),1182-1182.
36. Comment, A.; van den Brandt, B.; Uffmann, K.; Kurdzesau, F.; Jannin, S.; Konter, J.A.; Hautle, P.; Wenckebach, W.T.H.; Gruetter, R.; van der Klink, J.J. *Concepts in Magnetic Resonance Part B-Magnetic Resonance Engineering*, **2007**, 31B(4),255-269.
37. Jannin, S. **2009**.
38. Bornet, A.; Milani, J.; Vuichoud, B.; Linde, A.J.P.; Bodenhausen, G.; Jannin, S. *Chemical Physics Letters*, **2014**, 602,63-67.
39. Durieux, M.; Rusby, R.L. *Metrologia*, **1983**, 19(2),67-72.
40. Kurdzesau, F.; van den Brandt, B.; Comment, A.; Hautle, P.; Jannin, S.; van der Klink, J.J.; Konter, J.A. *Journal of Physics D-Applied Physics*, **2008**, 41(15).
41. Bornet, A.; Melzi, R.; Jannin, S.; Bodenhausen, G. *Applied Magnetic Resonance*, **2012**, 43(1-2),107-117.

Part B:

Improved and novel instrumentation for Dissolution DNP

In this part, we will describe the complete dissolution DNP setup and focus on its new implementation. Two probe designs are presented in details, one for DNP and pulsed NMR experiments that can be tuned for nuclear spin resonances typically from 20 to 300 MHz and the second for DNP with simultaneous longitudinal detection of electron spin resonance. The dissolution setup is then presented. The development of a magnetic tunnel is presented in detail and the benefices are explained. Concrete applied benefices are presented in *Part C: Applications*. Finally a setup to irradiate with a LASER is presented in order to close this part.

Chapter 1: Experimental design

We have designed and built a novel CP-DNP probe for cross-polarization from ^1H to ^{15}N and ^1H to ^{29}Si at 6.7 T and 1.2 K compatible with our home-built D-DNP polarizer [1, 2]. The probe can accommodate a sample insertion stick with a sample holder in a cavity where both DNP and CP can be performed simultaneously with suitable microwave and radiofrequency irradiation. The probe design is shown in figure 1. The probe can be mounted with a LODESR coil or with double tuned CP coil. After CP-DNP, a dissolution stick can be inserted to rapidly dissolve the sample to yield an injectable hyperpolarized solution.

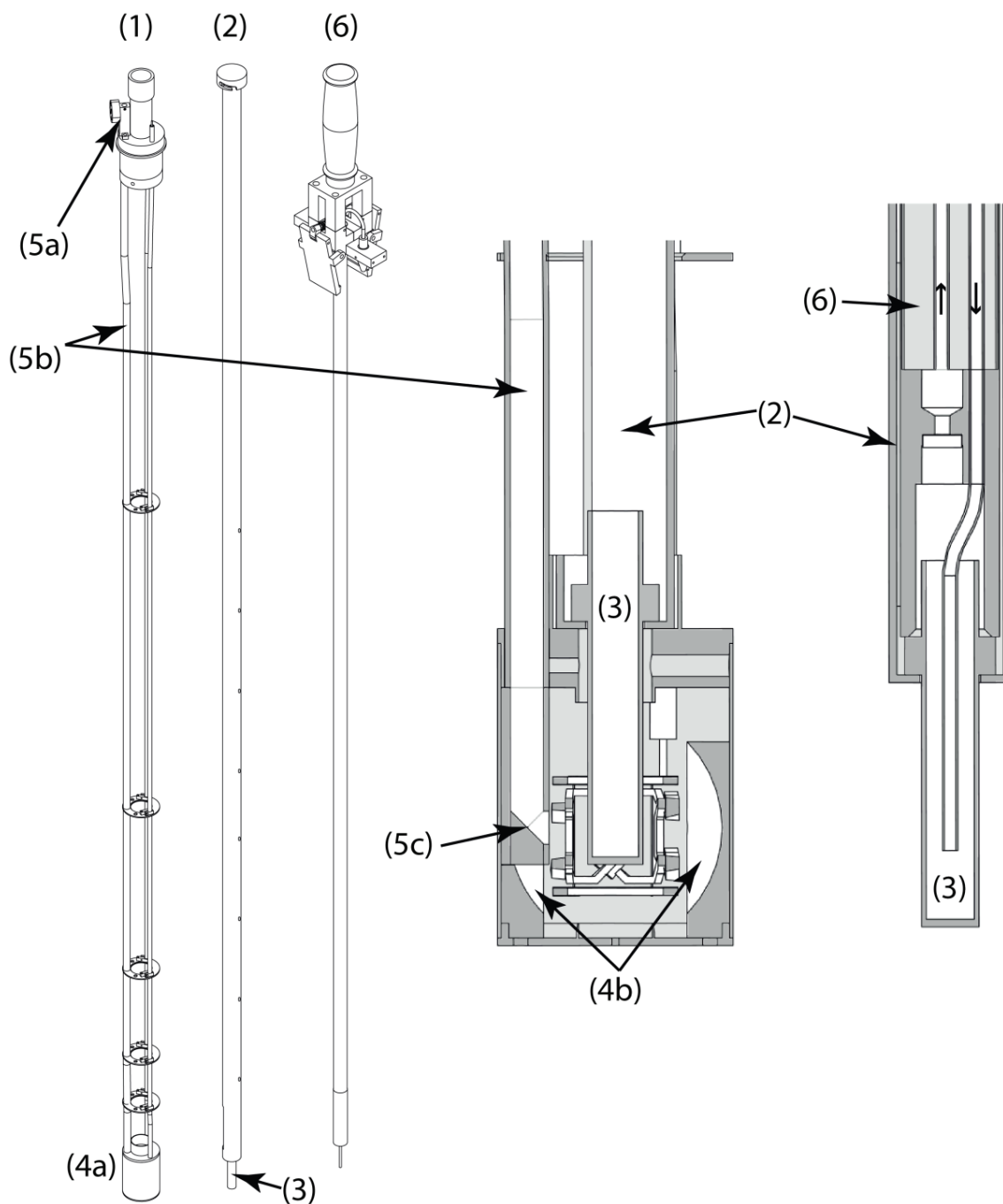


Fig. 1 The DNP probe comprises (1) a brass probe body that fits into the cryostat (cold bore with 45 mm inner diameter) and accommodates (2) a sample insertion stick made of G10 fiberglass that supports (3) a VESPEL sample holder. The gold-plated brass cavity (4a) is equipped with (4b) two concentric mirrors to focus the microwave field onto the sample. The 188 GHz microwaves are guided towards the sample through (5a) a 90° miter bend, followed by (5b) an oversized circular waveguide (5 mm inner diameter, 1.1 m long) and terminated by (5c) another 90° miter bend. After CP-DNP, a dissolution stick (6) can be used to inject hot water to melt the sample and push the liquid hyperpolarized solution to an NMR or MRI system.

a. Details of the top and bottom of the probe

The top of the probe is composed of a brass plate through which two semi-rigid coaxial pass to connect to the RF coils. The microwaves are transported through a stainless steel tube of 4.5 mm inner diameter. The microwaves are reflected by a gold-coated miter bend mirror. The gold coating prevents oxidation of the brass pieces, which would lead to detrimental attenuation of the microwaves.

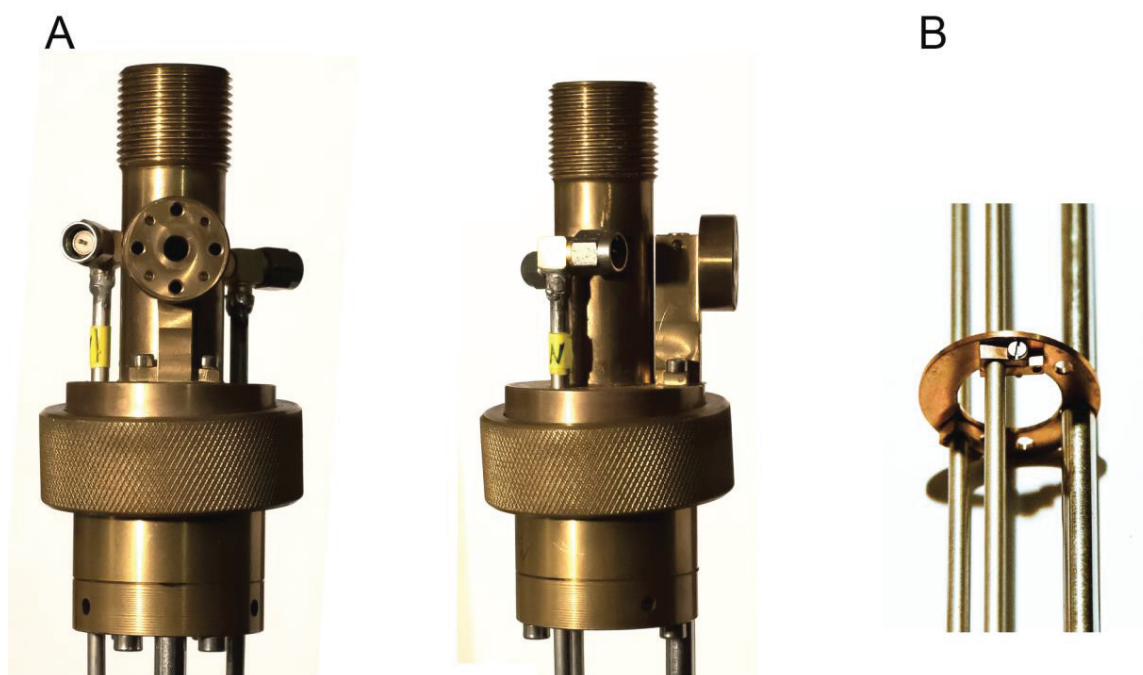


Fig. 2 (A) Upper part of the probe. The two RF semi-rigid coaxial cables of 1.1 m length are connected to the RF coils or to the LODESR coil. The microwave wave-guide is composed of a circular stainless steel tube. A gold-coated miter bend mirror is used to reflect the microwaves. (B) Along the probe, a few thermal shields are installed to prevent heat transfer from the top to the sample space. Only screws are used in these parts to prevent breaking the soldering.

In a similar way, the bottom part of the probe is composed of a brass piece held by the stainless steel tube and coaxial cables. Thermal shields placed along the probe also ensure that the structure is rigid enough. We decided to use a soldering-free construction to prevent breaking due to many hot-cold cycles. The microwaves are reflected towards the sample with a miter bend mirror placed in the cavity at the end of the waveguide.

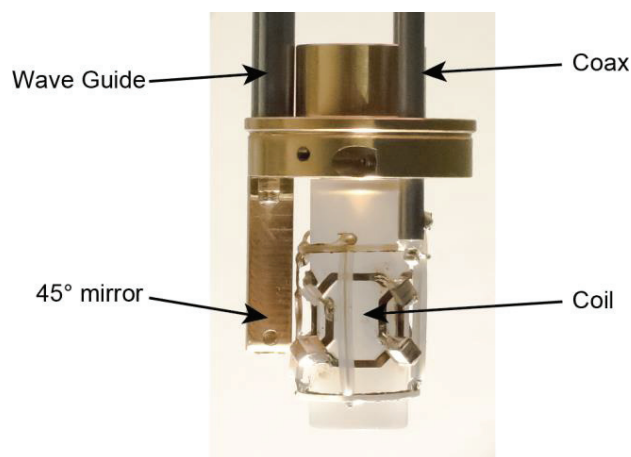


Fig. 3 Lower part of the probe composed of the cavity and coils. In the pictures we can easily identify the waveguide on the left with a gold-coated mirror to direct the microwaves to the center of the cavity where the sample is placed. On the right, the two coaxial cables are connected to the RF coils. Each piece in the cavity is gold coated. As for the thermal shield, the structure is solder-free and held by screws.

The cavity is closed with a series of gold-plated pieces. As explained in figure 4, these act as a focusing structure with a spherical mirror machined with a CNC machine, polished and gold coated.



Fig. 4 Focusing structure of the microwaves in the cavity. Much of the space is occupied by the RF coils to optimize irradiation of the sample.

The microwave path is equipped with an oversized circular waveguide including miter-bend mirrors at the input and near the DNP sample for optimal irradiation. An additional reflective structure in the DNP cavity aims at containing the microwaves close to the sample. The gold-plated mirrors have a positive effect on the ^1H signals during DNP. We gain about 20% in signal at maximum power, but the greatest advantage of this structure is that the power needed to achieve saturation is lower (figure 6).

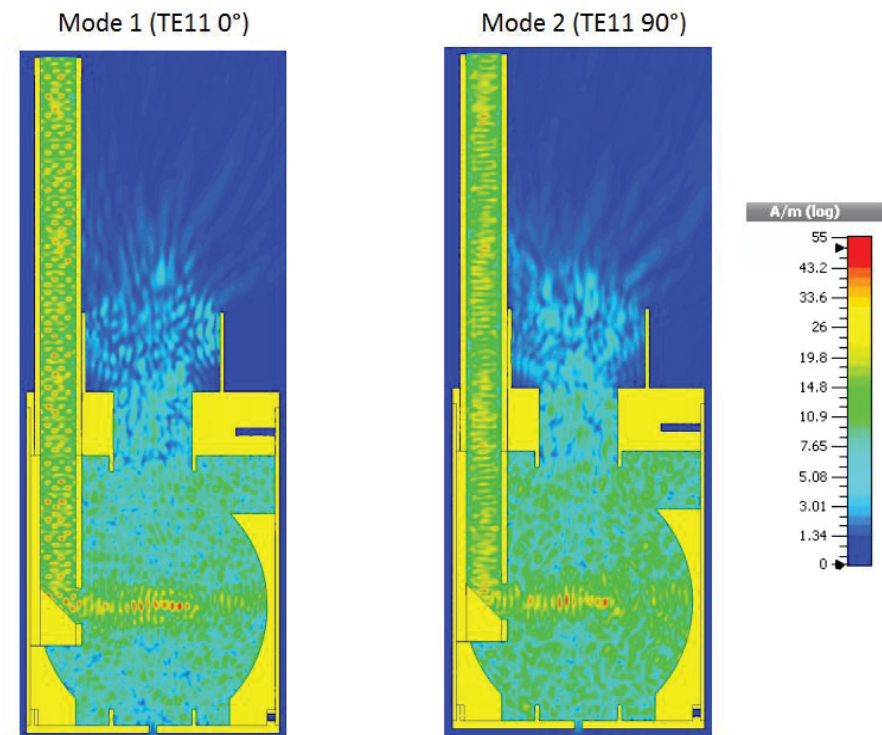


Fig. 5 The microwave propagation in our design was simulated by Armin Porea, Bruker Biospin. This focusing structure resembles an over-moded Fabry-Perrot resonator. The simulation studies the propagation of the TE11 mode (dominant in the circular wave guide) for two perpendicular conditions. The two orientations give essentially identical results. The volume of interest, in the center of the cavity, is apparently well irradiated thanks to the focusing mirrors.

This setup was designed using Solidworks software and the simulation of the magnetic component of the μw -irradiation was done by Bruker. To measure the efficiency of this design, we measured DNP with and without the focusing structure (see figure 6).

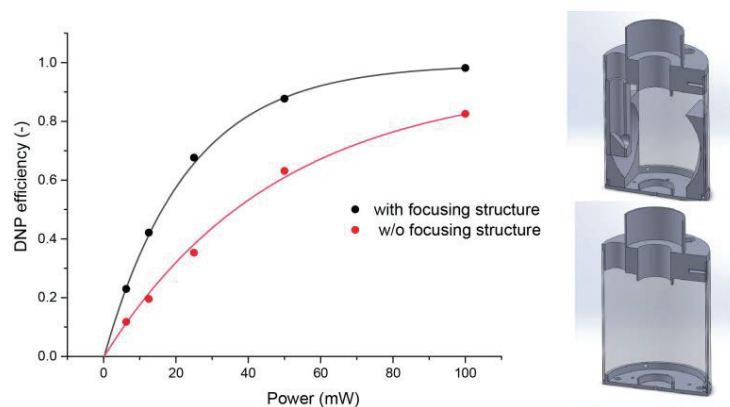


Fig. 6 The DNP efficiency depends on the power of the microwave irradiation at the sample position. Here, we show that with the reflective structure one can get higher polarization and better electron spin saturation. In other term, the B_1 field is more intense.

If we compare the build-up times with and without mirror, we also find differences. Indeed, with the mirrors, the ^1H DNP build-ups are faster. This effect is much more pronounced when the power is decreased to lower values. Figure 7 shows a plot of the build-up time τ_{bu} as a function of the maximal signal (DNP efficiency).

Power (mW)	τ_{bu} with mirrors (s)	τ_{bu} w/o mirrors (s)
100	57	77
50	74	136
25	106	224
12.5	177	442
6.25	353	696

Table 1 The build-up times are related to the microwave power. The mirrors are designed to concentrate the power in the center of the sample. The build up with a mirror is faster than without mirror.

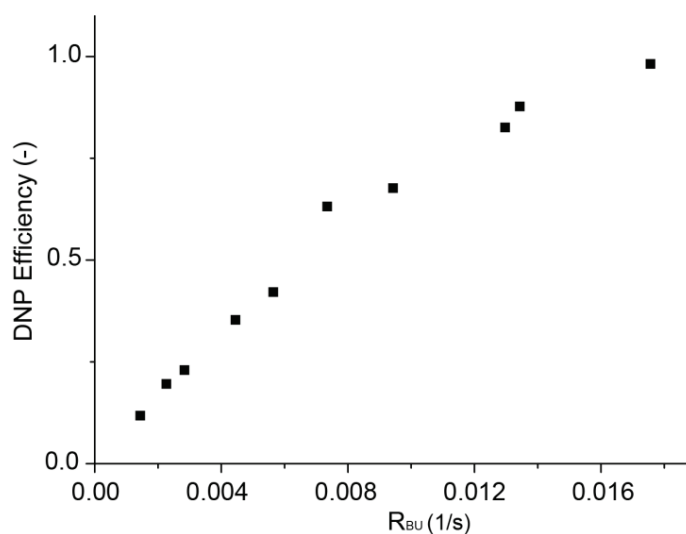


Fig. 7 DNP efficiency as a function of the build-up rates with the focusing structure. The build-up rate appears linear with the DNP efficiency.

Chapter 2: Longitudinal Detection of ESR (LODESR)

a. Introduction

DNP involves the microwave-driven saturation of electron spin transitions, usually in organic free radicals with a spin $\frac{1}{2}$. This section shows how we have implemented a simple Electron Spin Resonance (ESR) setup to measure the ESR line of our polarizing agents. Because of its high gyromagnetic ratio, under our DNP conditions, the electron spin Zeeman splitting corresponds to a few hundreds of GHz versus a few hundreds of MHz for the nuclear spins. Traditionally, EPR studies in the context of DNP are performed in resistive magnets at low field (X-band, 0.3 T) by CW irradiation and high frequency detection. In order to perform ESR under real DNP conditions at high field, and to be able to measure the real ESR spectrum under these conditions, we adopted a different strategy called Longitudinal Detection Electron Spectroscopy Resonance (LODESR) [6, 7]. It is indeed crucial to have a measure of the ESR spectrum of radicals under the exact same conditions as DNP to optimize the DNP experiment. For that purpose, we have built a home-made LODESR probe and implemented a simple excitation and detection circuit interfaced with our LabVIEW software.

b. Probe Design

The principle of LODESR is to alternatively saturate with microwaves and let the populations relax across the ESR transition, while synchronously detecting the current induced in a coil that arises from the change in global longitudinal magnetization. Therefore, the probe must comprise a solenoidal coil with an axis parallel to B_0 . The saturation is performed with microwave irradiation at frequencies $187.5 < f_{\mu w} < 188.5$ GHz. More details about the microwave source can be found in in chapter 2. The coil is made of copper wire of 0.22 mm diameter. The number of loops is approximately 570. At room temperature, the resistance is 19.5Ω and the inductance of 1.386 mH. At 4K the resistance falls to 0.9Ω .

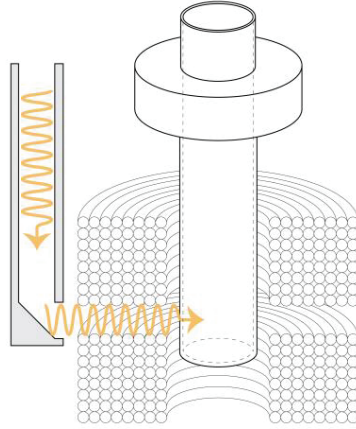


Fig. 8 Scheme of the LODESR coil. The coil is split in the middle to allow the propagation of microwaves to the sample.

During a LODESR experiment, the current is induced by the variation of the electron spin magnetization. The current or the voltage in the coil is simply detected. The relation between the current I and the electric potential U is directly related to the impedance Z of the coil:

$$Z = \frac{U}{I} \quad (2.1)$$

By irradiating the sample with microwaves, the ESR transition is saturated, so that the electron spin magnetization decreases. This change of magnetization induces a current in the coil. Just after the microwave irradiation is stopped, the magnetization comes back to its initial state with the electron spin-lattice relaxation time, i.e., the magnetization increases and a current of opposite sign is detected. This follows Faraday's law of induction:

$$\varepsilon = -\frac{d\Phi}{dt} \quad (2.2)$$

where ε is the electromotive force which induces a current in the coil, Φ the magnetic flux which correspond to $\Phi = B \cdot S$ where B is the magnetic field and S is the surface of the electric circuit, i.e., of a loop of the coil. This definition is valid for a coil which its plan is oriented perpendicular to the magnetic field and can be derived from the Maxwell equations.

$$\oint_C \vec{E} \cdot d\vec{l} = -\iint_S \frac{d\vec{B}}{dt} \cdot d\vec{S} \quad (2.3)$$

The electrons are accelerated in the electric field, the current is created and a potential can be detected. Depending on the time interval between the switching on and off of the microwave source, we can simply measure the ESR amplitude (and optionally reconstruct the whole ESR spectrum by scanning the microwave frequency in an incremental fashion) by using a short delay (typically 1 ms), or we can also record the complete saturation or relaxation curve by using a long delay (typically 1 s.)

Frequency scan: By alternating the power-attenuation of the microwave source, we can measure successively positive and negative currents during microwave on and off periods. The current intensity is directly proportional to the ESR amplitude at each specific microwave frequency. The experiment can be repeated with a frequency typically of 503 Hz (we prefer to avoid multiples of 50 Hz to average out potential artefacts coming from the electrical network). The final result is obtained by summing the absolute values of the induced current.

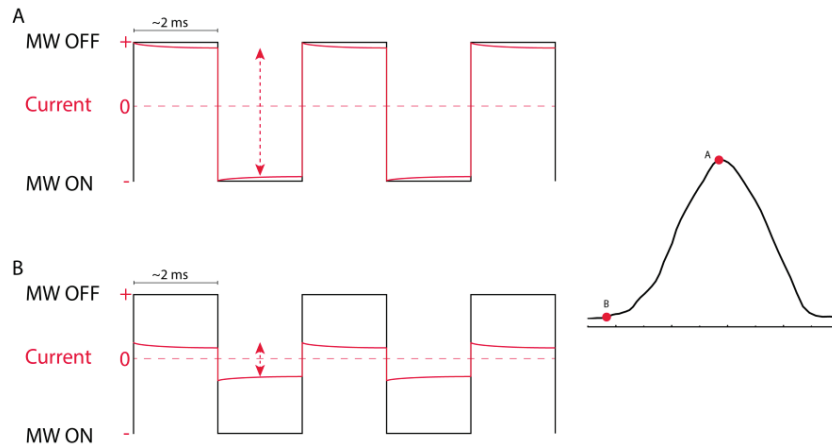


Fig. 9 The frequency scanning mode consist in saturating a small portion of the ESR spectrum (the smaller the portion the higher the resolution), and observe the change of the magnetization. Case A: The signal is maximal when the MW irradiates the full width of the ESR spectrum of the radical. The measured current is quite high. Case B: When the MW irradiates a zone outside the ESR line, only a very small current is created in the coil.

Saturation/relaxation time measurements: Similar to frequency scanning experiments, the same procedure can be applied at a fixed frequency but with a time delay long enough to allow the measurement of the complete saturation/relaxation decay. We typically use a frequency of 4 Hz.

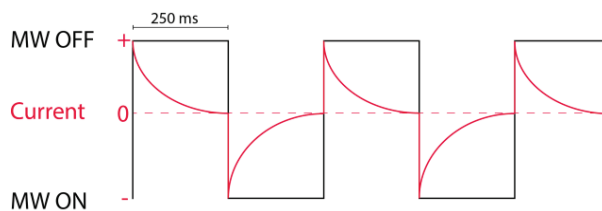


Fig. 10 The saturation/relaxation time measurements consist in measuring the change of the magnetization. To reach to that goal, the measured time is increased to about 250 ms.

c. Results (ESR spectra, T_{1e} , saturation curve)

The technique was tested with several nitroxide radicals under standard DNP condition. Samples were prepared with 100 μ L of d_6 -DMSO/ D_2O / H_2O 60/30/10 v/v/v doped with 50 mM of one of the following radicals: TEMPOL, TEMPOL- d_{12} , Diterbutyl TEMPOL, PyTEMPAMINE and Cucurbit[7]urilTEMPO (see figure 11).

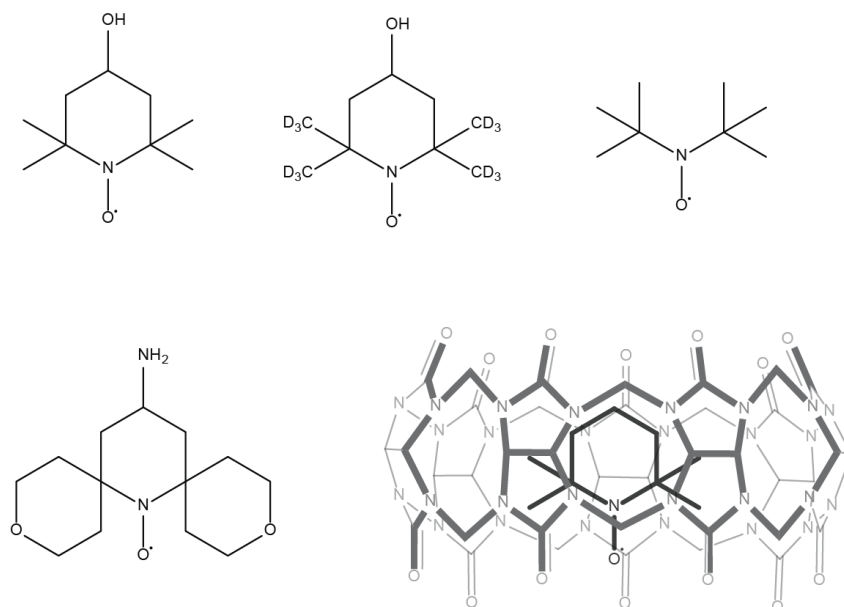


Fig. 11 Molecular structure of radicals. TEMPOL, TEMPOL- d_{12} , Diterbutyl TEMPOL, PyTEMPAMINE and Cucurbit[7]urilTEMPO.

The ESR spectra of the different radicals are rather similar, particularly for the TEMPOL, TEMPOL- d_{12} and Diterbutyl TEMPOL (figure 12). This not a surprise considering the small changes in the structures. However, the spectrum of PyTEMPAMINE is relatively narrow and that of Cucurbit[7]urilTEMPO is slightly broader.

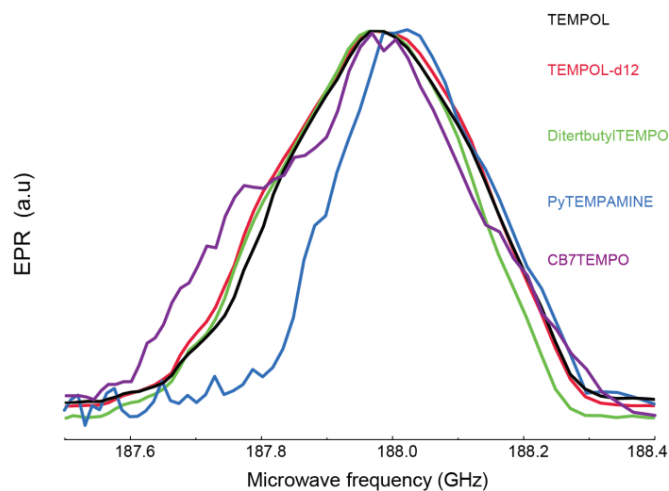


Fig. 12 Spectra of TEMPOL (black), TEMPOL-d₁₂ (red), Diterbutyl TEMPOL (green), PyTEMPAMINE (blue) and Cucurbit[7]urilTEMPO (purple). All spectra were obtained s with our home built LODESR probe.

We also measured the spectrum for TEMPOL at a higher temperature, 4 K instead of 1.2 K. We observed a broader base of the spectrum at 4 K than at 1.2 K. We suppose an effect due to the polarization of the ¹⁴N.

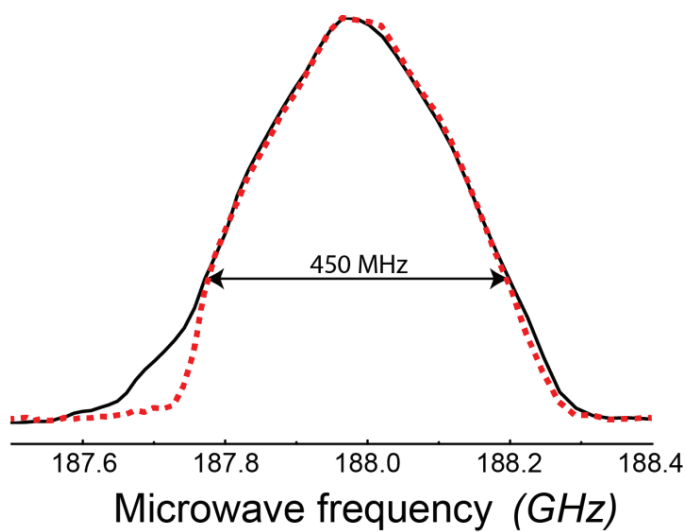


Fig. 13 Spectra of TEMPOL at 4 K (black line) and 1.2 K (red dot line).

LODESR experiments were performed to measure the saturation and relaxation curves of the electron spin resonances in TEMPOL, TEMPOL-d₁₂, Diterbutyl TEMPO and PyTEMPAMINE. The results were fitted with mono-exponential functions. During first period, the sample is irradiated with microwaves. The current measured in the coil is proportional to the derivative of the ESR magnetization.

$$\frac{dS}{dt} \propto I \tag{2.4}$$

Since the function is mono-exponential, $\frac{dS}{dt} \propto S = \exp(-\frac{t}{B})$. The parameter B gives the characteristic time constant of the decay. A simple fitting with an exponential function suffices to obtain the time constant.

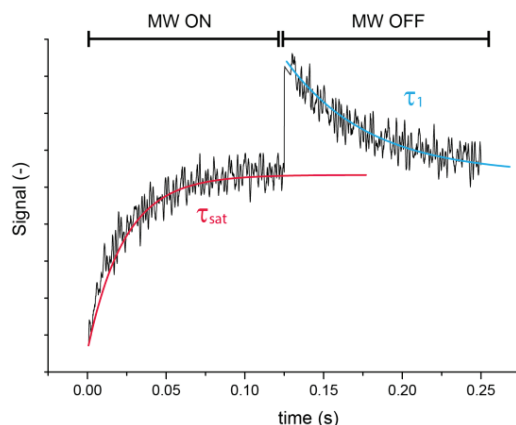


Fig. 14 LODESR measurements of the saturation and relaxation curves of TEMPOL at 1.2 K and 6.7 T, with 100 mW microwave power. During the first part, the microwaves are on, and then switched off. This cycle is repeated several times (here 800 times).

We fitted the saturation time and the relaxation time for the radicals (except for Cucurbi[7]urilTEMPO). The differences between species are not significant except for the T_1 of PyTEMPAMINE.

	(ms)	TEMPOL	TEMPOL-d ₁₂	Diterbutyl TEMPO	PyTEMPAMINE
4 K	T_{sat}	24	32	21	25
	T_1	42	44	36	66
1.2 K	T_{sat}	25	39	30	31
	T_1	63	56	38	66

Table 2 Relaxation and saturation times for TEMPOL, TEMPOL-d₁₂, Diterbutyl TEMPO and PyTEMPAMINE at 4 K and 1.2 K.

Saturation and relaxation of TEMPOL was investigated for positive frequencies (irradiation at $\nu = 187.9$ GHz) and negative frequencies (irradiation at $\nu = 188.3$ GHz). We did not detect any significant differences.

Polarization	T _{sat} 4K	T ₁ 4K	T _{sat} 1.2K	T ₁ 1.2K
Negative	24 ms	42 ms	25 ms	63 ms
Positive	26 ms	41 ms	28 ms	75 ms

Table 3 Relaxation and saturation times for TEMPOL at 188.3 GHz and 187.9 GHz microwave irradiation at 4 K and 1.2 K.

Chapter 3: Low temperature CP-DNP probe

The polarization of low-gamma nuclear spins can be boosted by DNP but the build-up times are relatively long which is a critical limitation of high-throughput applications of D-DNP. One strategy to boost the efficiency the DNP process is to perform indirect DNP by Cross Polarization (CP). CP is commonly used in the context of MAS-DNP. For D-DNP the implementation of $^1\text{H} \rightarrow ^{13}\text{C}$, $^1\text{H} \rightarrow ^{15}\text{N}$ and $^1\text{H} \rightarrow ^{29}\text{Si}$ CP was done with home-built probes described in this chapter. A probe $^1\text{H} \rightarrow ^{129}\text{Xe}$ was also built, but only its characteristic parameters were measured.

Most applications to metabolic imaging exploit the enhancement of carbon-13 nuclei, [8], but nitrogen-15 has also been successfully enhanced by D-DNP [9-12]. In small molecules where ^{15}N is bound to protons, $T_1(^{15}\text{N})$ is typically on the order of 60 s; but when ^{15}N is not directly bound to any protons, very long relaxation times $200 < T_1(^{15}\text{N}) < 800$ s have been observed near 300 K [11]. This makes D-DNP particularly attractive for nitrogen-15. Early studies of ^{15}N D-DNP report a modest efficiency of direct ^{15}N DNP when using trityl or nitroxide radicals, resulting in disappointing polarizations $P(^{15}\text{N}) < 4\%$ [11] and exceedingly long build-up times, typically $\tau_{\text{DNP}}(^{15}\text{N}) > 2$ hours. Building on our recent work on low temperature cross-polarization (CP) to carbon-13 under D-DNP conditions [13-15], we have extended the method to nitrogen-15 and have achieved polarization levels on the order of $P(^{15}\text{N}) = 20\%$ at 1.2 K and 6.7 T with short build-up times $\tau_{\text{CP-DNP}}(^{15}\text{N}) \approx 10\text{-}15$ min.

a. RF circuit details

The Q factors and 90° pulse lengths were measured for all channels at 4.2 K. The probe has been optimized for $B_0 = 6.7$ T, with microwave irradiation near 188 GHz, and for CP with Larmor frequencies $\nu(^1\text{H}) = 285.2$ MHz and $\nu(^{15}\text{N}) = 28.9$ MHz for $^1\text{H} \rightarrow ^{15}\text{N}$ probe and $\nu(^1\text{H}) = 285.2$ MHz and $\nu(^{29}\text{Si}) = 56.7$ MHz for $^1\text{H} \rightarrow ^{29}\text{Si}$ probe, using an adiabatic multiple-contact pulse sequence described elsewhere for ^{13}C [15]. Here we give the details of the RF coils and of the RF circuit in the polarizer. Figure 15 describes the assembly of the RF coils. The aim is to have two decoupled resonances in the same volume. Because we need a sample access from the top for dissolution, we chose an approach with two pairs of saddle coils that are inductively coupled with an external coil, the two being perpendicular to each other.

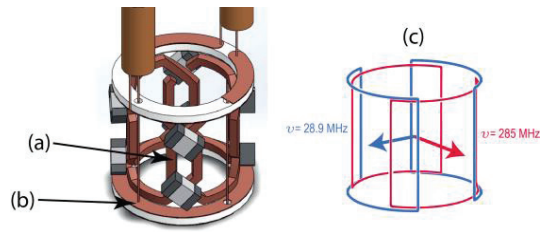


Fig. 15 The RF coils are made of a pair of perpendicular concentrically mounted outer coils (b) that are inductively coupled with a pair of inner coils (a). A schematic view of the inner coils is shown in (c).

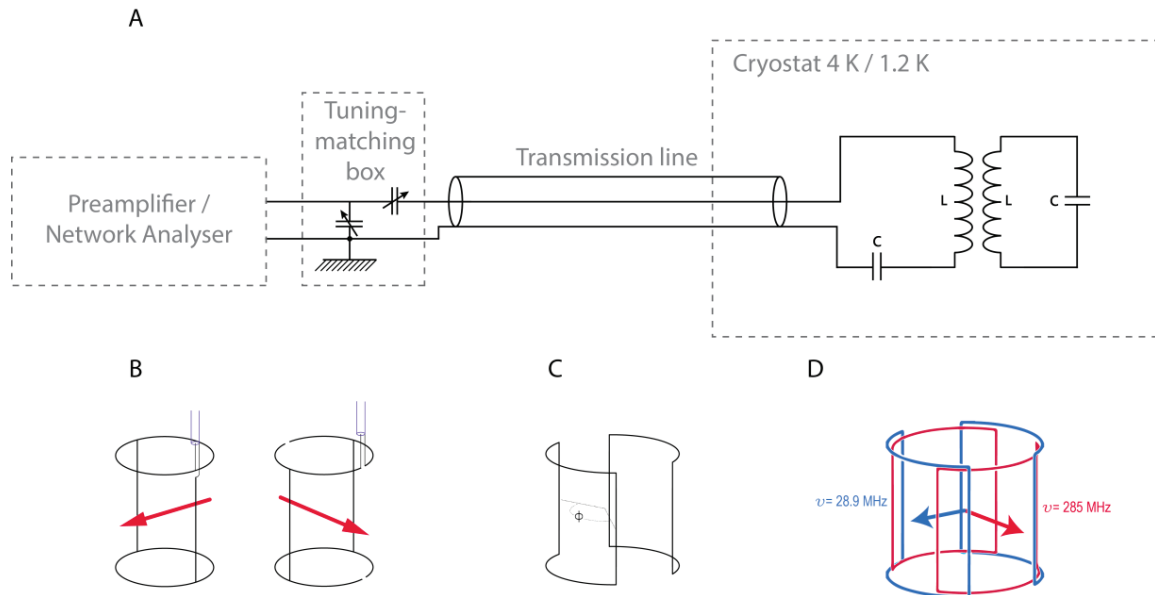


Fig. 16 A Electronic diagram of one RF channel of the probe. The inner coil is tuned at the right frequency thanks to capacitors in series. The inner coil is composed of a pair of saddle coils. Each saddle coil is designed to have an opening angle of 120° to maximize the B_1 field in the center of the assembly [4].

The outer coils have to be perfectly aligned for maximal coupling. They are built using a printed circuit PCB and assembled with copper wire that is coated with silver.

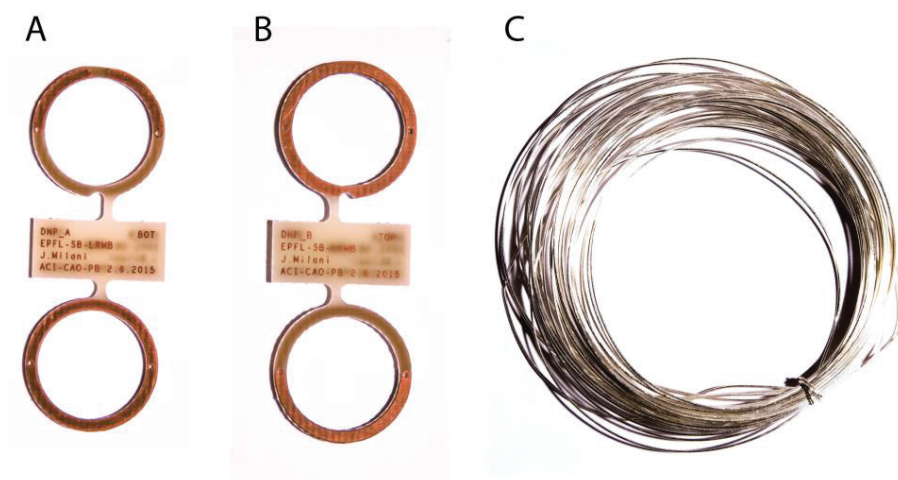


Fig. 17 To guarantee the exact perpendicularity of the two circuits, external coils are made using PCB. A and B show the two sides of the PCB plate. The assembly is completed with copper wire coated with silver to prevent oxydation (C).

The inner coil is mounted on a Polychlorotrifluoroethylene (PCTFE or PTFCE) holder, best known by its commercial name *Kel-F*. *Kel-F* was chosen because it does not contain any protons. It is also a robust polymer able to withstand rapid changes of temperature.

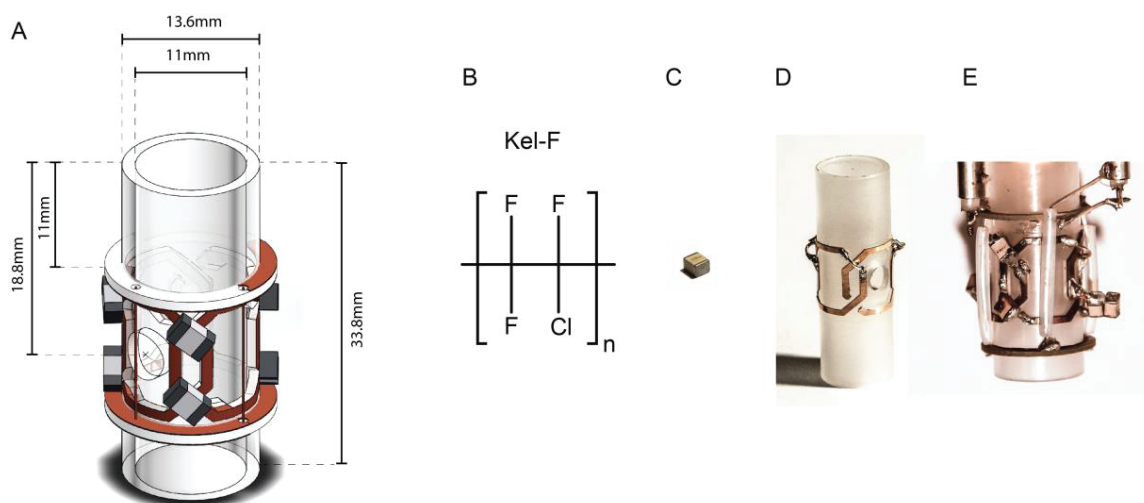


Fig. 18 (A) The coil is held by *Kel-F* material. (B) This material, Polychlorotrifluoroethylene, is ^1H free to minimize parasite ^1H signals in measurements of the thermal equilibrium. (C) Capacitor used in the inner coil to match the resonance. (D) Inner coil composed by copper pieces inserted in the *Kel-F* support. (E) Assembly of the complete coil including the outer coil.

The first generation of coils used a flexible PCB printed circuit with a copper width of $50\ \mu\text{m}$ and rolled with the help of a Teflon strap. Though this method gave good results, several temperature cycles highlighted the structural weakness of the system. From this observation we decided to develop a more robust solution. The second generation is composed of a holding piece made of *Kel-F*. The coils are made of copper wire of 1 mm thickness. A third generation is under development with thinner

copper wire of 0.2 mm thickness to avoid ringing issues. These are made by wire EDM machining. This is a very precise method to obtain such small pieces (± 0.005 mm).

	^1H channel (285.25 MHz)	^{15}N channel (28.91 MHz)
Q factor	197	137
90° pulse	6 μs with 50 W	12 μs with 100 W (or 10 at 200 W)

Table 4 Parameters of the resonant circuits for ^1H and ^{15}N of the DNP probe at 4.2 K. The parameters of the proton resonance are common to all probes.

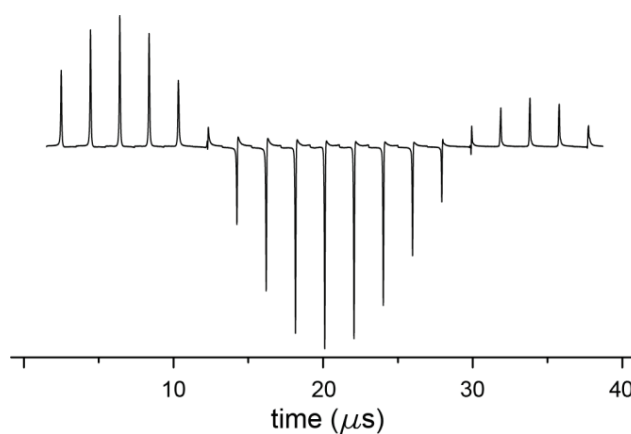


Fig. 19 ^1H nutation experiments at 4.2 K at 50 W. The pulse lengths vary from 2 to 40 μs .

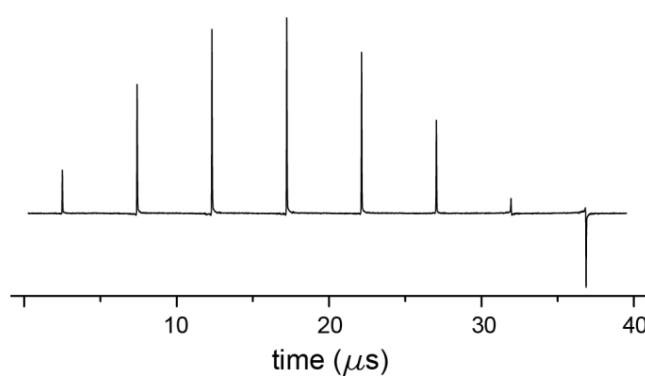


Fig. 20 ^{15}N nutation experiments at 4.2 K at 100 W. The pulse lengths vary from 2 to 40 μs .

	¹ H channel (285.25 MHz)	²⁹ Si channel (56.67 MHz)
Q factor	197	152
90° pulse	6 μs with 50 W	8.5 μs with 100 W

Table 5 Parameters of the resonant circuits for ¹H and ²⁹Si of the DNP probe at 4.2 K.

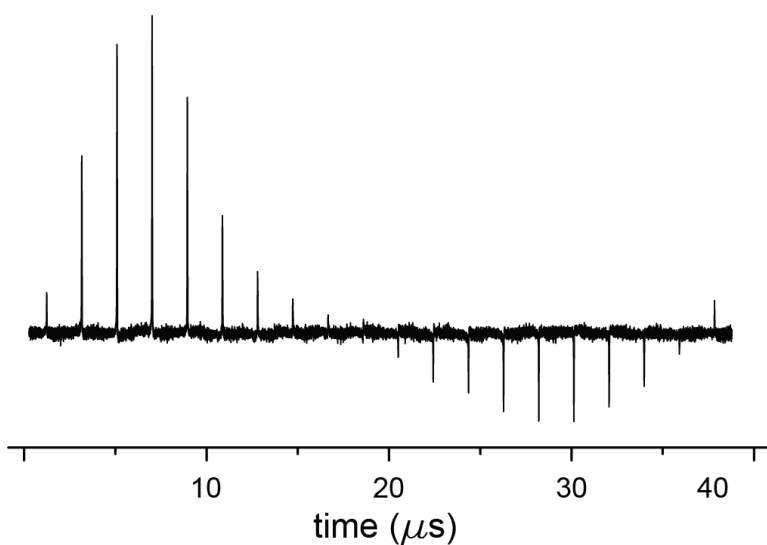


Fig. 21 ²⁹Si nutation experiments at 4.2 K at 100 W. The pulse lengths were varied from 2 to 40 μs.

b. Tuning and matching strategy

This section describes the practical methods used for tuning the coils to the desired frequencies. A Network Analyzer was used to measure the reflection of the system. One of the difficulties is to discriminate between resonances of the cable and those of the actual coil. Cable resonances are omnipresent in such a complex system composed of saddle coils, cables, connectors, etc. The aim is to find an area with minimal cable resonances. That said, cable resonances might be useful when weakly coupled to the main resonance in order to tune our system with an external tuning and matching box. With an external box, we were able to move the cable resonance. By their interaction with each

resonance in the system, the coil resonance is “pushed” by the cable resonance to the desired frequency.

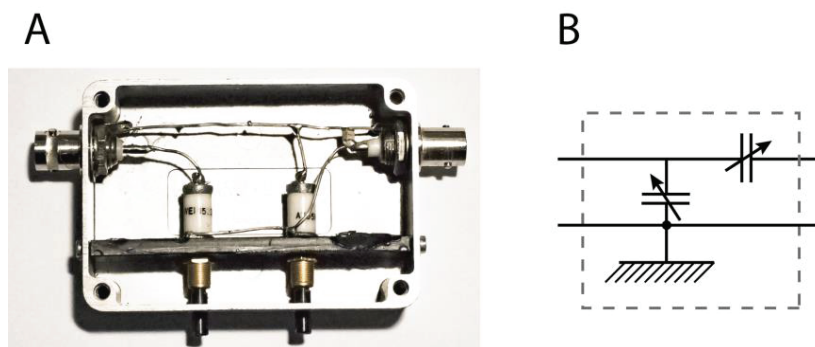


Fig. 22 The external tuning and matching box is composed by one capacitor in series and another one in parallel. It is use for fine “wobbling” in situ. A Photography of the box. B Electronic scheme of the box.

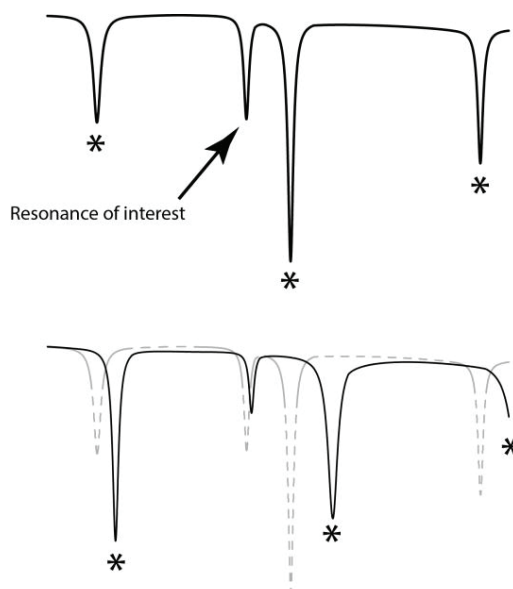


Fig. 23 The resonance of the complete system is composed of several resonances. In general, due to the external tuning and matching (TM) box, we observe cable resonances (*). The resonance of interest which is created by the coil has to be tuned to the exact frequency. By moving the cable resonances by changing the capacitors of the TM box, it is possible to change slightly the frequency of the resonance of interest.

In a system composed of two coils inductively coupled with the rest of circuit, there may be two modes of resonance, one parallel and another anti-parallel. This often happens for high frequency resonances like ^1H (285.25 MHz). To identify each resonance, one can insert a flat metal piece in the coil and see the perturbation on the resonance frequency. For the parallel mode, this creates a maximal perturbation in the center of the cavity. The antiparallel mode has a minimum perturbation in the center and two maximal perturbations close to the sides. The parallel mode is of course the appropriate mode for the purpose of NMR.

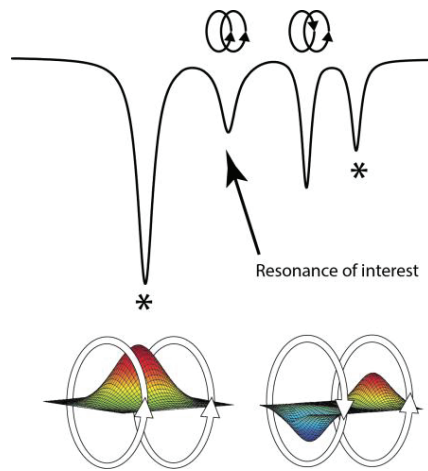


Fig. 24 We observed for ^1H resonance near 285 MHz that the coils create two distinct resonances. These are in fact two modes of the resonance of the saddle coil. The resonance of interest is the parallel mode. Stars (*) represents cable resonances.

c. Pulse sequences adapted for cross-polarization (CP)

In Magic Angle Spinning (MAS), Cross Polarization (CP) [16] is a common technique to enhance signals of low-gyromagnetic nuclei. The usual pulse sequence is composed of a 90° pulse applied to the protons (high gyromagnetic ratio), followed by locking pulses on both channels. The aim of these locking pulses is to make the two spins precess at the same frequency in the rotating frame, so as to fulfill the Hartmann-Hahn condition [17]. The precession frequency of each spin is simply equal to

$$\omega_1 = -\gamma B_1 \quad (2.6)$$

When the precession frequencies are matched for two spins, the locking time is often called the contact time because the two reservoirs of polarization are in contact and can exchange. The acquisition is usually done directly after the CP pulses.

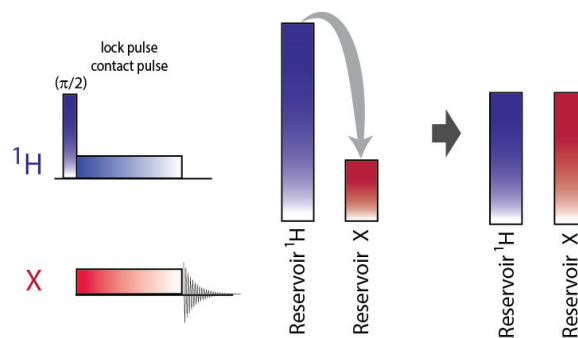


Fig. 25 The standard CP pulse is composed of two locking pulses. The aim is to force the two nuclei to precess at the same frequency. During this precession, the two spin can be considered as equivalent and can exchange their energy. Spins with high energy like ^1H will transfer part of their energy to low-energy nuclei like ^{13}C , ^{15}N , ^{29}Si ,...

In practice, because of the limited B_1 , and therefore the limited excitation bandwidth, but also because of relaxation in the rotating frame, a non-negligible part of the proton polarization is lost during the CP process. In our experiment, the CP step is repeated several times to accumulate the polarization on the low-gamma nuclear spin. In order to preserve the polarization already acquired, the sequence requires a 90° pulse on the low-gamma channel before the contact pulses. With the same logic, the magnetization is put along the z axis again after the contact pulses. To follow the complete build-up of the polarization, a pre-saturation interval is added at the beginning of the experiment. Small angle pulses are incorporated into the sequence to observe the behavior between CP contacts without destroying the whole polarization.

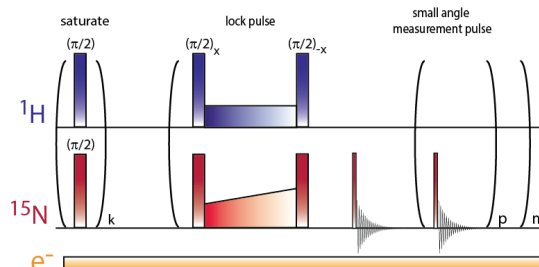


Fig. 26 For D-DNP, it is necessary to build the polarization to obtain the maximum value. The pulse sequence is composed of spin locking pulses in both channels and a 90° flip-back pulse applied to the low gyromagnetic nuclei (here ^{15}N) to preserve to polarization already gained. A small angle pulse is applied to monitor the polarization during the DNP process.

A strategy using adiabatic inversions can be used [18] to improve the excitation bandwidth when B_1 is limited.

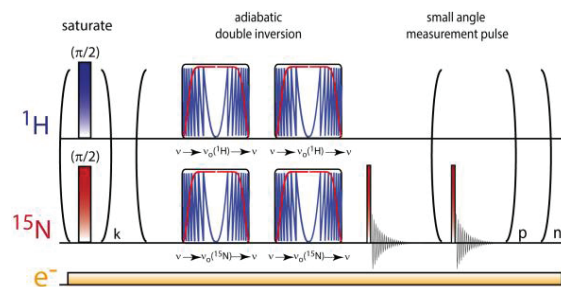


Fig. 27 The adiabatic CP sequence is composed of two pairs of adiabatic pulses. During these adiabatic pulses, like before, the two nuclei are forced to precess at the same frequency.

Figure 28 shows typical results of CP-DNP measurements with the pulse sequence presented in figure 27. This shows a simulation with parameters comparable to our measurements for ^{15}N CP DNP build up (the simulation parameters are presented in the figure caption). In figure 28 A, the red line describes the magnetization build-up of ^{15}N . Each step corresponds to a CP pulse. CP pulse is applied after 3.3 min in this example. When the signal becomes higher than its maximum value reached by direct irradiation, the magnetization tends to decrease. This is already the case after one single CP. It is important for CP DNP experiments to take in account the loss of the proton polarization during CP pulse. The black line in figure 28 A presents a simulation of the ^1H build-up. At each CP, part of the ^1H polarization is lost, partly due to the transfer to low γ -nuclei, but mainly because of the loss of polarization during spin locking because of rapid $T_{1\rho}$ relaxation in the B_1 field.

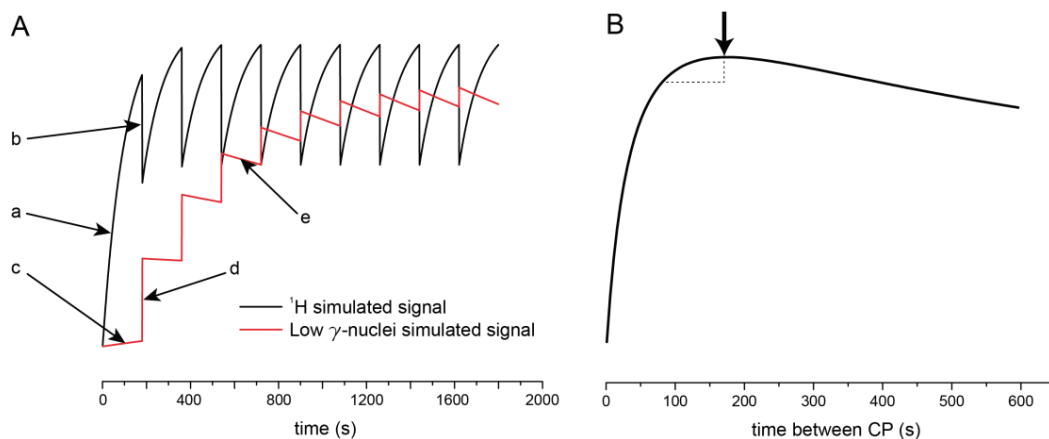


Fig. 28 A: Simulation of a build-up based on typical observed parameters. With $T_{\text{build-up}}(^1\text{H}) = 100$ s, $T_{\text{build-up}}(^{15}\text{N}) = 2000$ s, max value of $P(^{15}\text{N}) = 0.2 \cdot \text{max value of } P(^1\text{H})$. The loss of ^1H polarization is 40 % during each CP pulse. Ratio of gain of each CP of $^{15}\text{N} = 30$ % during CP pulse. The ^1H is very fast and comparable to ^{15}N , it is necessary to wait for the ^1H magnetization to become high enough before the next CP pulse (a). During CP pulses, ^1H magnetization decrease (b), here again, we have to wait to get a sufficiently high magnetization for ^1H . The ^{15}N signal begins to build up with direct DNP time constant (c). During CP, its magnetization is suddenly enhanced (d). If its value is higher than its theoretical maximum for direct DNP, the ^{15}N magnetization tends to decrease (e). Usually it reaches a steady state. **B:** It is possible to calculate the theoretical optimum time between CP contacts to get the maximal polarization. In practice, we do not wait long enough, and prefer to gain time than to get the last few percent of polarization.

d. Samples containing ^{15}N

Five samples were tested, which consisted in 0.8 M solutions of one of the following molecules: ammonium chloride, urea, glycine and trimethylphenylammonium (TMPA), all ^{15}N -labelled, and choline in natural ^{15}N abundance (0.36 %), dissolved in a d_6 -DMSO/ D_2O (60/40 v/v) glass-forming mixture doped with 50 mM TEMPOL radicals. Such samples can lead to large ^1H polarization $P(^1\text{H}) = 60$ -90% with short build-up times $\tau_{\text{DNP}} = 2$ min at 1.2 K. Several CP contacts were repeated at intervals of 3 min, leading to a final polarization $P(^{15}\text{N}) = 17$ -25% with apparent build-up times $\tau_{\text{CP-DNP}} = 7$ -16 min. Table 6 shows the polarization achieved for the four ^{15}N -labelled molecules, with and without CP, i.e., $P(^{15}\text{N})^{\text{CP}}$ and $P(^{15}\text{N})^{\text{direct}}$, and their associated apparent build-up times $\tau_{\text{CP-DNP}}(^{15}\text{N})^{\text{CP}}$ and $\tau_{\text{DNP}}(^{15}\text{N})^{\text{direct}}$, respectively. From these parameters, we determined amplification and acceleration factors brought about by CP, $\varepsilon_{\text{CP}} = P(^{15}\text{N})^{\text{CP}}/P(^{15}\text{N})^{\text{direct}}$ and $\kappa_{\text{CP}} = \tau_{\text{DNP}}(^{15}\text{N})^{\text{direct}}/\tau_{\text{DNP}}(^{15}\text{N})^{\text{CP}}$ respectively. For glycine, we could not determine the thermal equilibrium polarization, but we could nevertheless determine ε_{CP} and κ_{CP} .

	$P(^{15}\text{N})^{\text{CP}}$	$\tau_{\text{CP-DNP}}(^{15}\text{N})^{\text{CP}}$	$P(^{15}\text{N})^{\text{direct}}$	$\tau_{\text{DNP}}(^{15}\text{N})^{\text{direct}}$	$\varepsilon_{\text{CP}} = P^{\text{CP}}/P^{\text{direct}}$	$\kappa_{\text{CP}} = \tau_{\text{DNP}}^{\text{direct}}/\tau_{\text{DNP}}^{\text{CP}}$
Ammonium	17 %	15.9 min	2.3 %	27.4 min	7.4	1.72
Urea	23 %	7.6 min	1.4 %	43.9 min	16.4	5.8
TMPA	25 %	12.7 min	0.7 %	43.5 min	35.7	3.4
Glycine	N.A	7.6 min	N.A	25 min	21.5	3.2

Table 6 Indirect polarizations assisted by CP and direct polarizations with their associated build-up times and amplification and acceleration factors measured at 1.2 K in ^{15}N -labelled ammonium, urea, TMPA and glycine solutions in d_6 -DMSO/ D_2O (60/40 v/v) with 50 mM TEMPOL.

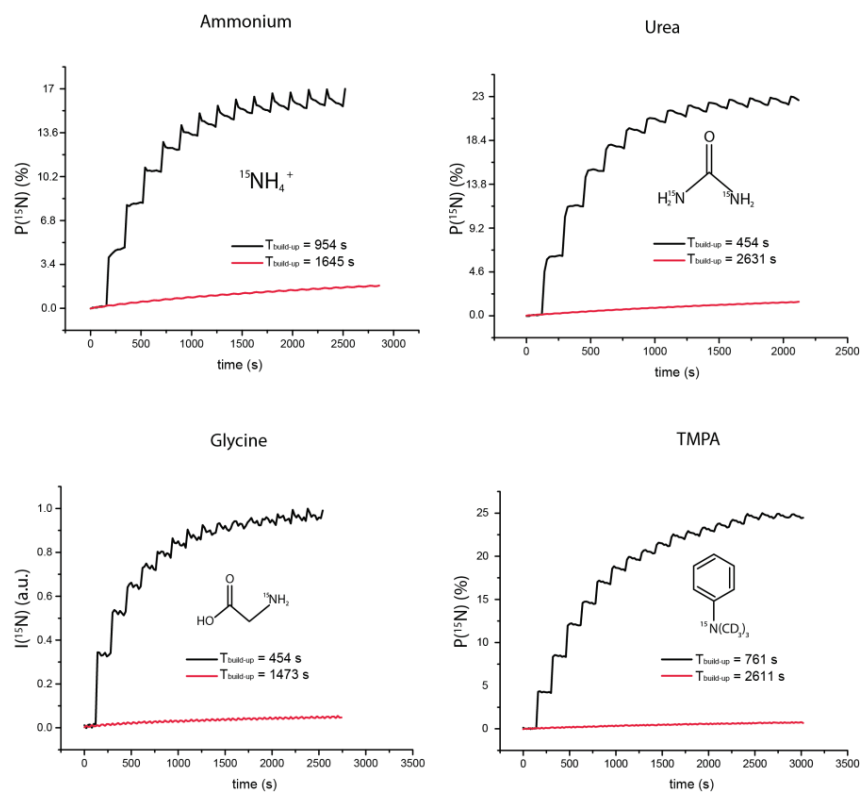


Fig. 29 Build-up of the polarization $P(^{15}\text{N})$ measured at 1.2 K in 75 % deuterated ammonium, urea, glycine and TMPA in d_6 -DMSO/ D_2O / H_2O (60/30/10 v/v) with 50 mM TEMPOL, assisted by multiple-contact CP (black lines) and by direct DNP without CP (red lines).

i. CP optimization

The CP sequence used in our study consists of two adiabatic inversions of the magnetization synchronized on both NMR channels, as previously described. The nutation frequencies of the I and S spins are made equal in the doubly rotating frame to fulfill the Hartmann-Hahn condition [17]. The length of the CP contact pulses is optimized to achieve a balance between polarization transfer and $T_{1\rho}$ relaxation. The optimum pulse length obviously depends of the magnitude of the ^1H - ^{15}N dipole-dipole (DD) coupling. The best pulse lengths for glycine, urea and TMPA are shown in figure 30.

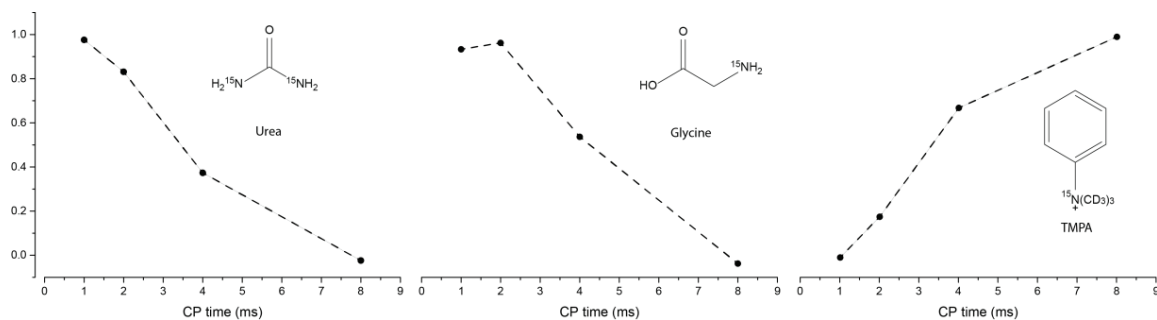


Fig. 30 The optimum duration of the CP contact pulses depends on the strength of the ^1H - ^{15}N dipole-dipole (DD) couplings. Strong couplings occur in urea and glycine where protons are only one or two bonds away from ^{15}N , respectively, so that short contact pulses of 1 or 2 ms are found to be optimal. Conversely, for TMPA where the protons are as far as three bonds away from ^{15}N , contact pulses of 8 ms are optimal (longer pulses are not recommended to avoid arching).

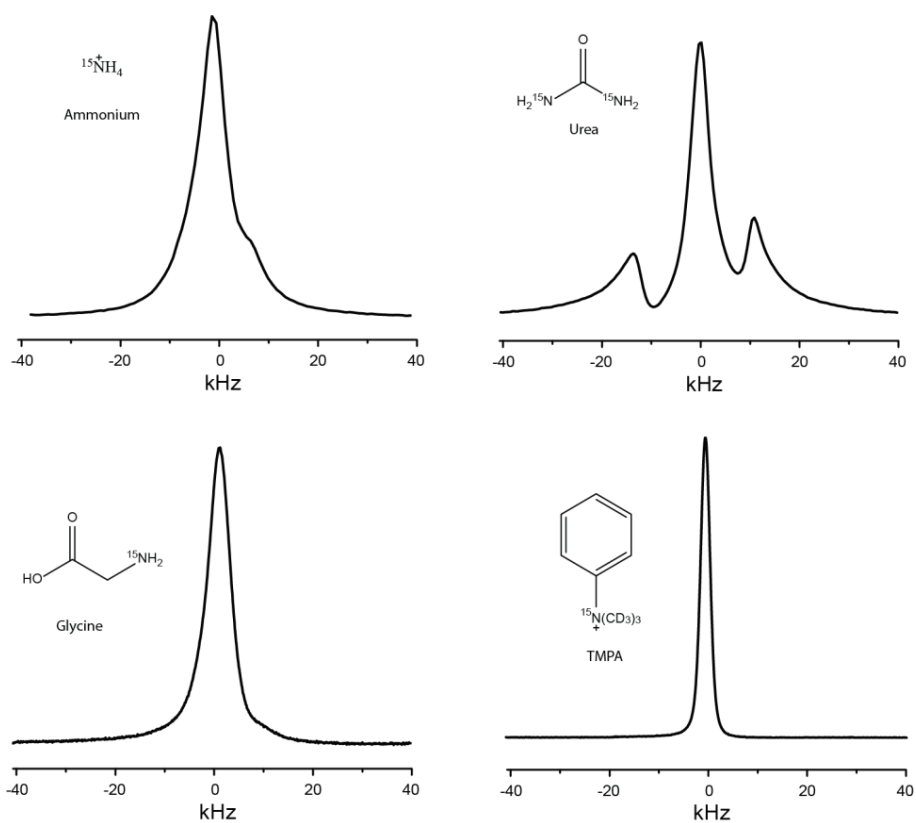


Fig. 31 ^{15}N NMR spectra enhanced by DNP in 0.8 M frozen solutions of ammonium, urea, glycine and TMPA in d_6 -DMSO/ D_2O (60/40 v/v) with 50 mM TEMPOL, recorded at 6.7 T (28.91 MHz for ^{15}N) and 1.2 K.

e. Samples containing ^{29}Si

The ^{29}Si CP probe was investigated using a solution of sodium silicate salt. The sample is composed 3 M NaSiO_3 in natural ^{29}Si abundance (4.5 %). The solvent is $\text{H}_2\text{O}/\text{D}_2\text{O}/\text{d}_8\text{-Glycerol}$ 10/50/40 v/v/v contains 50 mM TEMPOL. CP at low temperature is highly efficient (figure 32). The relaxation time is relatively long : $T_1 = 3.45 \pm 0.15$ h at 4 K. In our experiment, the calculated polarization is 33 ± 10.2 %, however, the poor thermic signal is difficult to interpret. The long T_1 forces us to wait several hours between every scans which is sometimes not possible.

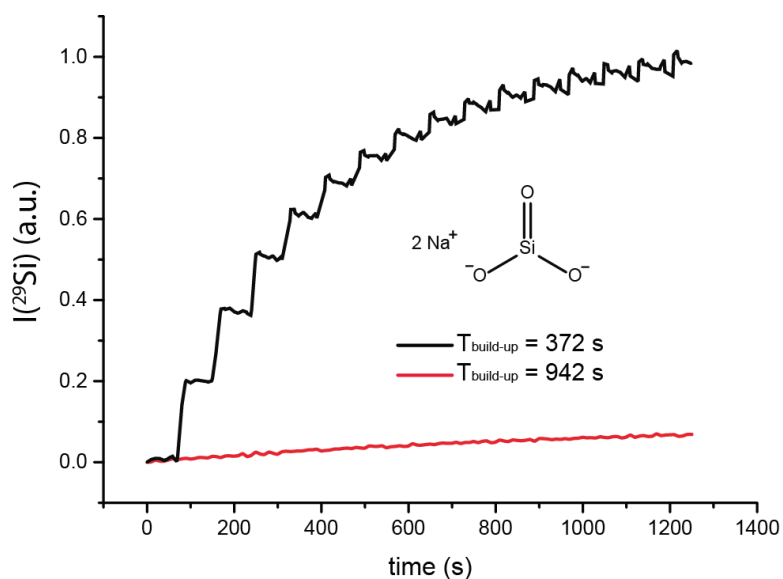


Fig. 32 ^{29}Si build up with CP in black and without CP in red. The sample is composed of 3 M NaSiO_3 dissolved in $\text{H}_2\text{O}/\text{D}_2\text{O}/\text{d}_8\text{-Glycerol}$ 10/50/40 v/v/v with 50 mM TEMPOL.

Silicium generally possesses a long T_1 , especially in nano- or micro-particles where T_1 can be a few hours in solution [19, 20]. The long T_1 is explained by the isolation of the ^{29}Si nuclei inside the particle, where they are completely isolated from dipolar relaxation with ^1H and, due to the relatively low natural abundance (4.5 %), from other ^{29}Si . DNP for ^{29}Si particles could be interesting, especially for MRI for different reasons besides the long spin lattice relaxation: silicon is compatible with *in vivo* experiments. Secondly, there is no trace of any ^{29}Si background in a body. DNP of ^{29}Si requires a long polarization time, on the order of few hours [21]. Spin diffusion allows one to polarize the core of the particles. The advantages of a CP DNP probe are not obvious. CP would enhance the polarization of ^{29}Si in contact with ^1H , so only atoms near the surface of the particle would be enhanced. Spin diffusion would have the same effect as direct DNP, i.e., a long polarization time. For a CP DNP experiment with ^{29}Si nano- or micro-particles, we should expect a higher polarization but not necessary a faster build up time.

f. Solution-state ^{15}N NMR at 300 K

After CP-DNP, when the polarization had reached a maximum, water heated to 393 K (120°C) and pressurized at 1 MPa (10 bar) was injected to dissolve the frozen sample. He gas at $6 \cdot 10^5$ Pa (6 bar) was used to push the solution through a 1.5 mm inner diameter PTFE tube of 5 m length. This tube was enclosed in a magnetic tunnel [22] connected to an 11.4 T NMR spectrometer (28.91 MHz for ^{15}N , 500 MHz for protons) with a standard 5 mm NMR sample tube. The transfer time was 5 s and the injection was done after 2 s by a homemade injector. A 5° pulse was applied every 10 s to measure the decaying hyperpolarized ^{15}N signals. Polarizations and relaxation times measured for glycine, ammonium, urea, choline and TMPA after dissolution are shown in table 7. One advantage of ^{15}N labeled molecules is the long $T_1(^{15}\text{N})$ in solution, so that the polarization $P(^{15}\text{N})$ can be preserved for prolonged periods. The magnetization can then be transferred from ^{15}N to ^1H by a reverse INEPT sequence.

	$P(^{15}\text{N})$ (%)	$T_1(^{15}\text{N})$ (s)
Glycine*	6.0	35
Ammonium	7.1	39
Urea	19.2	197
Choline	(a)	233
TMPA	16.8	750

Table 7 Polarization $P(^{15}\text{N})$ in 32 mM hyperpolarized solutions after dissolution, measured at 11.74 T and 300 K. (a) The thermal polarization and hence $P(^{15}\text{N})$ could not be determined because of poor sensitivity. The symbol * designates a basic pH.

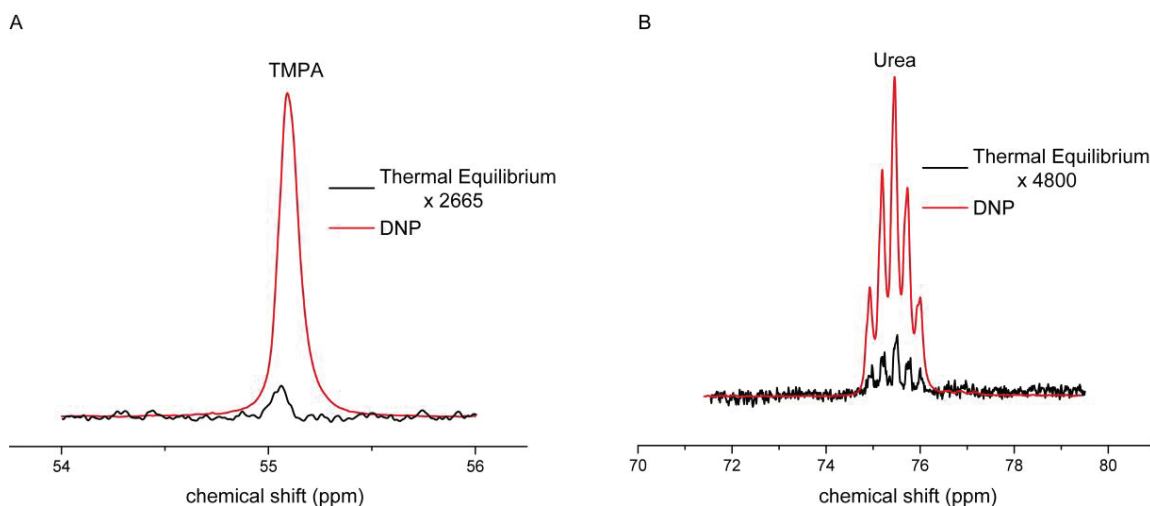


Fig. 33 A) ^{15}N -spectrum of ^{15}N -enriched of trimethylphenylammonium chloride ($(\text{CD}_3)_3\text{NC}_6\text{H}_5\text{Cl}$ (TMAPA) observed in solution at 28.91 MHz (11.4 T, 500 MHz for protons) in a single scan with a 5° pulse immediately after D-DNP (red line) and after complete return to thermal equilibrium, by accumulating 128 transients with 5° pulses at 600 s intervals in 24 hours (black line). The polarization $P(^{15}\text{N}) = 16.8\%$ was calculated by comparing with the thermal equilibrium signal. The singlet results from the isolated ^{15}N in TMAPA. (B) ^{15}N -spectrum of ^{15}N -enriched Urea (ND_2COND_2) observed in solution at 28.91 MHz immediately after D-DNP (red line), and after complete return to thermal equilibrium overnight, by accumulating 300 measurements with 5° pulses at 600 s intervals in 62 hours (2.6 days) (black line). The polarization was found to be $P(^{15}\text{N}) = 19.2\%$. The 1:2:3:2:1 multiplet is due to $^1\text{J}(^{15}\text{N}, ^2\text{D}) = 14$ Hz couplings with two deuterium nuclei which exchange with the solvent. The molecule is completely deuterated after dissolution with D_2O .

It is also possible to record ^{15}N spectra of non-enriched molecules in a single scan, as shown for choline in figure 34.

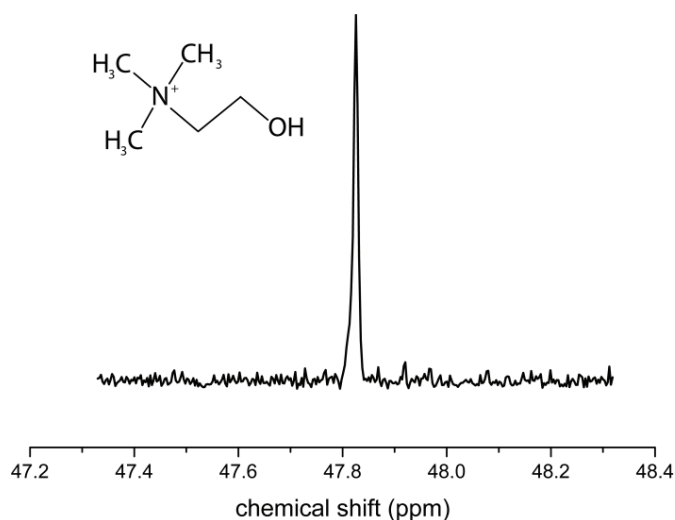


Fig. 34 Proton-decoupled ^{15}N spectrum observed with a 5° pulse immediately after D-DNP at 28.91 MHz of solution of 0.12 M choline ($\text{NH}_4^+\text{CH}_2\text{CH}_2\text{Cl}$) in D_2O with 0.36% natural ^{15}N abundance.

Using DNP from the electrons of TEMPOL to protons, followed by cross polarization from ^1H to ^{15}N , one can achieve remarkably high polarizations up to $P(^{15}\text{N}) = 25\%$ with a build-up time constant $\tau_{\text{CP-DNP}}(^{15}\text{N}) = 7\text{-}16$ min using a simple custom-built CP-DNP probe described herein. Such levels of

polarization were never attained before. The resulting NMR sensitivity and the long relaxation times $T_1(^{15}\text{N})$ observed in several compounds makes nitrogen-15 a very interesting candidate for hyperpolarization studies.

Chapter 4: Dissolution

a. Introduction

In D-DNP one uses separate devices for polarization and detection. The polarizer operates at low temperatures and moderate magnetic fields ($T = 1.2$ K and $B_0 = 6.7$ T in our laboratory) [23-26] where the electron spin polarization can be close to unity, i.e., $P(e) = 0.98$ in our system. By suitable microwave irradiation, part of the electron spin polarization can be transferred to the nuclei of the frozen sample. A burst of hot solvent is then squirted onto the hyperpolarized sample so that it rapidly melts and approaches room temperature, at which point the hyperpolarization can exceed Boltzmann's equilibrium polarization by four to five orders of magnitude. The sample is then transferred to a high-resolution NMR spectrometer or MRI scanner.

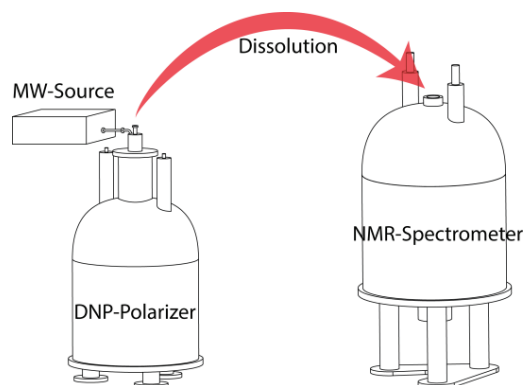


Fig. 35 Illustration of the general setup for a D-DNP experiment. On the left, the polarizer with its microwaves source. On the right the NMR spectrometer. Dissolution involves rapidly heating the sample and its transfer to an NMR spectrometer.

b. Dissolution stick

After CP-DNP, when the polarization had reached a maximum, hot water at 393 K (120°C), pressurized to 1 MPa (10 bar), was injected to dissolve the frozen sample. He gas at $6 \cdot 10^5$ Pa (6 bar) is used to push the solution through a 1.5 mm inner diameter PTFE. The setup to dissolve the sample is composed by a long carbon fiber stick that couples to the sample in the polarizer. Water is heated under pressure in a cavity which functions like an oven to reach a temperature of 120°C at a pressure of 10 bar. The stick is then rapidly inserted into the polarizer through the top of the probe. When the connection with the sample holder is established, a button on the stick is switched and the dissolution process starts. This process consists in opening the valve of the water oven and, after a delay of typically 0.5 s, in opening

another valve to push with He gas at 6 bar during 5 to 10 s, depending of the length of transfer path. The entire procedure is managed by LabVIEW software.

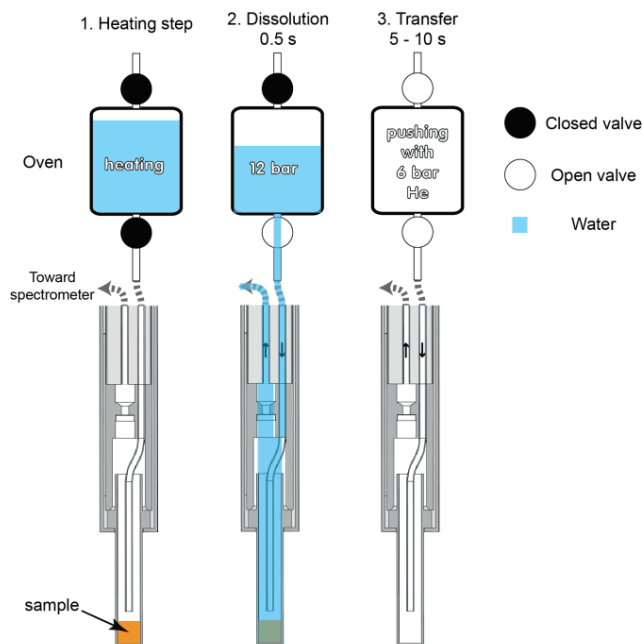


Fig. 36 The dissolution process comprises three steps. 1. Heating: 5 ml D₂O is introduced into the oven and heated to reach a temperature of 120 °C. 2: Dissolution step: the first valve is opened. The hot water goes through a Teflon tube to the sample and dissolves it. 3. Transfer: the second valve is opened to push the fluid through the canal. The pushing is done with He under 6 bar. The time of transfer is typically of 5 s. However, if a more viscous liquid is used, it is possible to increase the transfer time.

The standard design uses a long PTFE tube that does not offer any possibility to enclose it in a magnetic tunnel. Figure 37 illustrates this problem. The ambient field falls rapidly below 1 mT outside the polarizer. And because of the length of the stick necessary to reach the bottom of the probe (approximately 1.2 m), a long part of the tube is exposed to the ambient field during the dissolution process without any possibility to add a magnetic field. One disadvantage is that the fluid path and therefore the transfer time become longer, but the passage in low field is more critical since it can increase dramatically the longitudinal relaxation rate [22]. This issue is discussed in detail in chapter 4.

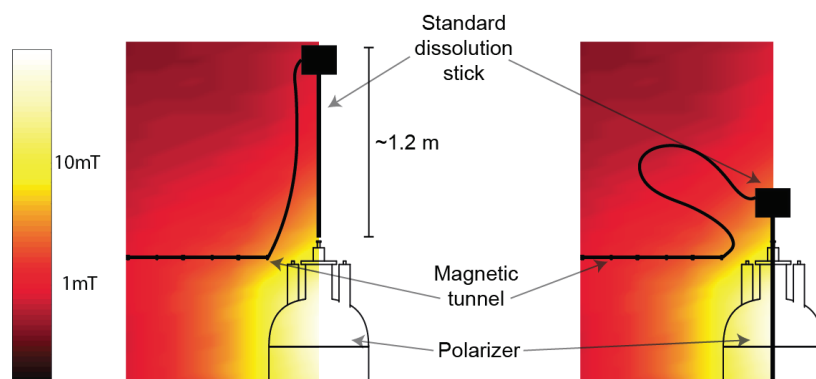


Fig. 37 The field above the polarizer dramatically decreases. The ambient magnetic field was measured (see Chapter 4, section b.i.) A long stick (1.2 m) has to be inserted from the top. The Teflon tube has to be flexible to allow this motion. Note that the Teflon tube is in a magnetic tunnel for the transfer. The magnetic tunnel is presented in detail in Chapter 4.

We designed a new dissolution insert to bypass the problem with a fast-coupling valve (see figure 38). The benefit is that the magnetic tunnel can be connected directly to the dissolution stick without any unnecessary additional tubing.

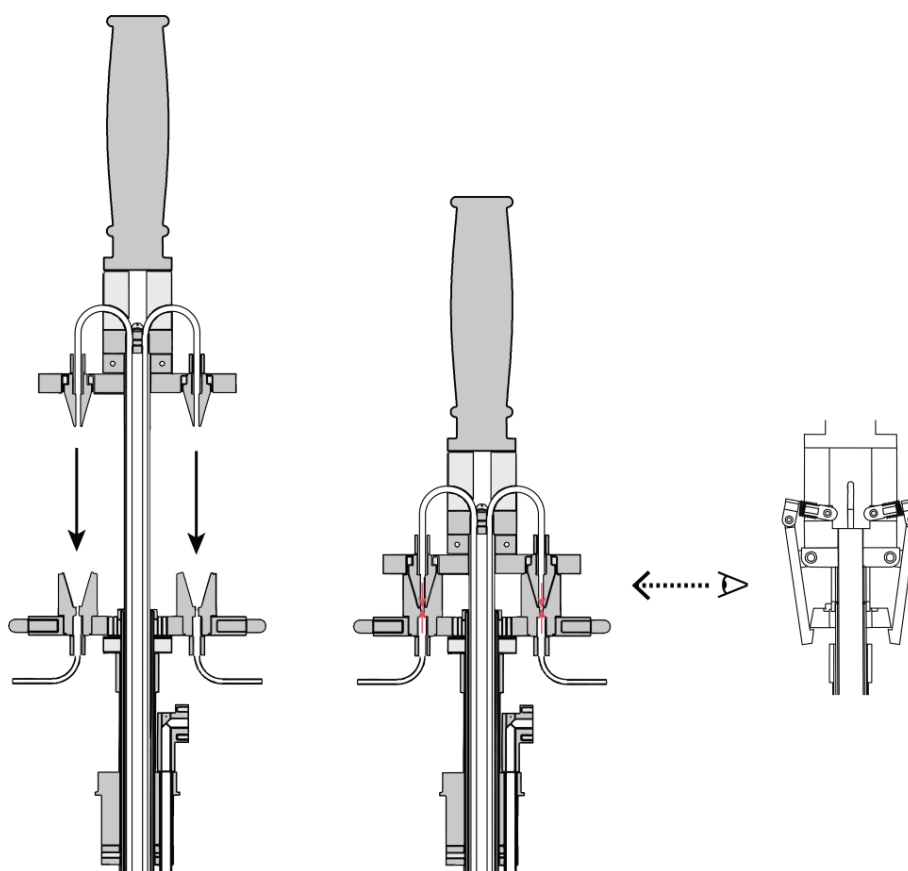


Fig. 38 A fast clipping stick has been designed. The clipping was tested and easily supports the pressure required for dissolution. On the left: side view of the fast clipping stick.

The stick is rapidly coupled and held by a fast clipping system. The system is functional and has been tested (without DNP for the moment) and can resist a pressure of 10 bar.

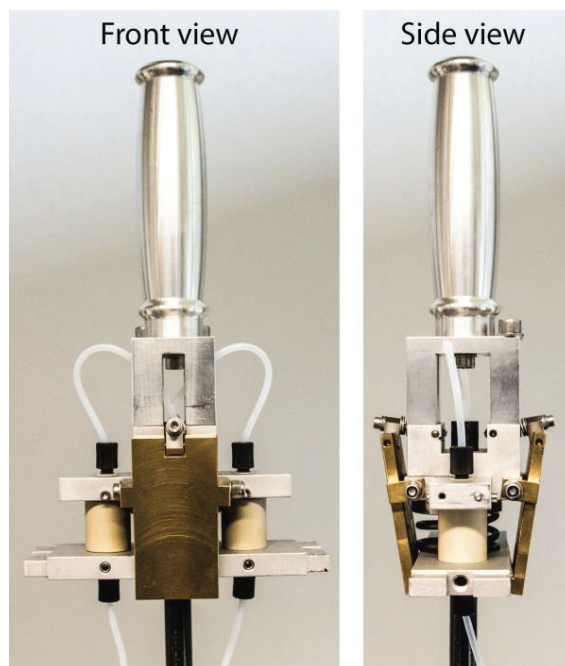


Fig. 39 Photograph of the fast clipping dissolution stick.

c. Fluid path

Decreasing the transfer time of the hyperpolarized solution from the polarizer to the detection spectrometer is crucial in order to observe nuclear species with short relaxation times. To achieve this goal, a transfer system with ultrafast switching valves was designed that allows pushing the sample with a higher pressure (until 20 bar). This configuration is inspired by the setup of Hilty's group [27]. This system used an optical sensor (TT Electronics/Optek Technology OCB350L125Z) to detect the bolus in the tube. The fast switching valves (CHEMINERT C22-6180 D) are connected to the high pressure network and can change position within 70 ms. The system is operated using LabView software. After dissolution, the high pressure pathway is automatically initialized. Figure 40 presents the three steps of the dissolution sequence. During step A, the two valves are both in position P1, i.e., in their initial state. As soon as the first optical sensor D1 has detected the passage of the bolus, the valve 1 is switched position to P2 (step B), until the second optical sensor D2 detects the passage of the bolus near to the NMR tube.

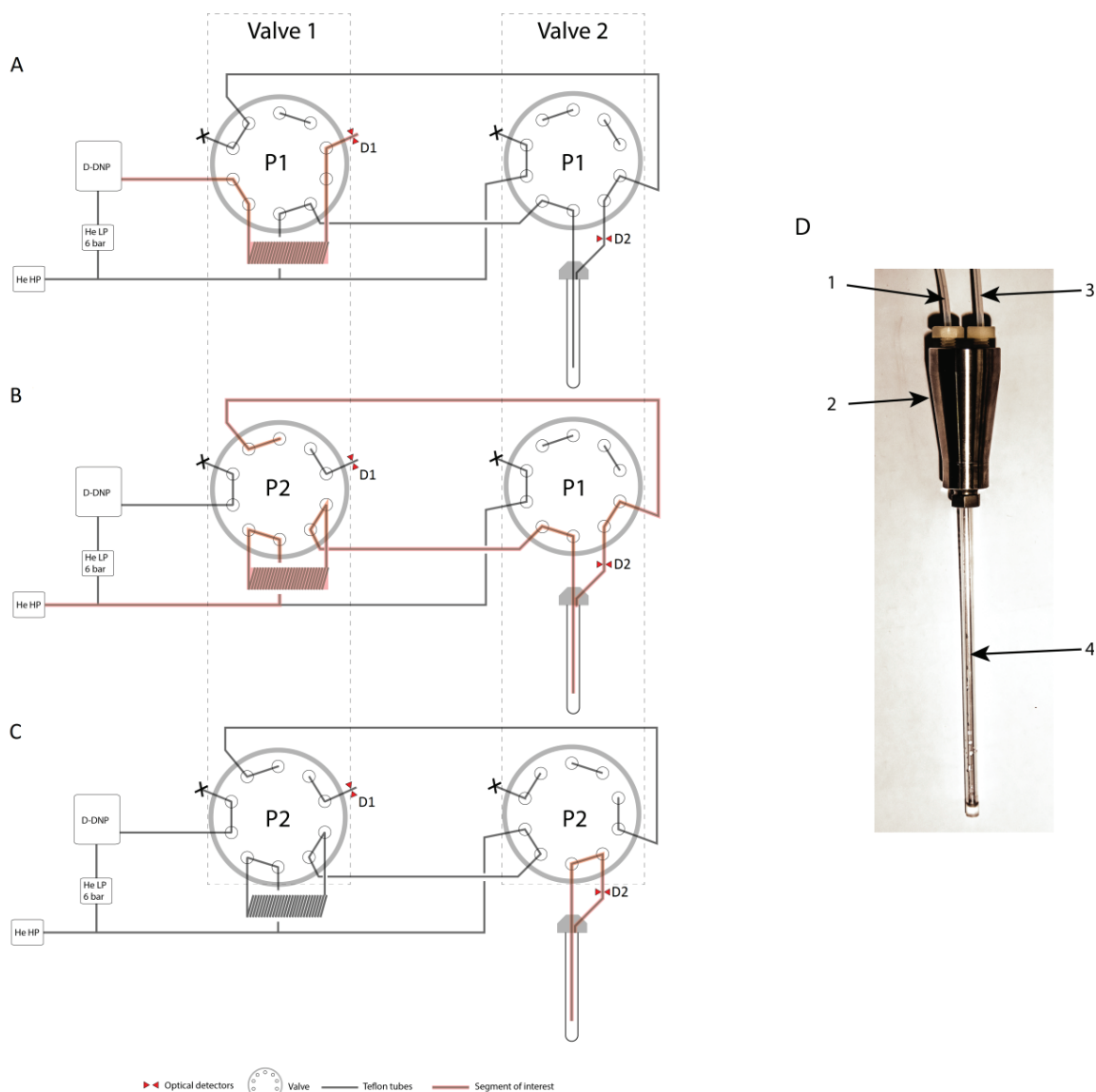


Fig. 40 Dissolution with a high pressure system comprising two fast switching valves V1 and V2. (A) The dissolution process is launched at 10 bar, with the both valves in their initial position P1. The solution passes through a tube with the desired length and volume. (B) When it reaches the first optical detector D1, valve V1 changes position from P1 to P2. The solution is pushed by helium gas at an adjustable pressure. It is pushed towards the NMR tube in the spectrometer. (C) A second optical detector D2 gives the signal to change the position of valve V2 from P1 to P2. With this configuration of both valves V1 and V2 position P2, the NMR tube is isolated while the signal is recorded. After transfer, the system is emptied by getting again the B step, V1 in P2 and V2 in P1. It is possible to clean up by injecting water and repeating the operation. (D) High pressure NMR system with (1) Teflon input tube, (2) titanium piece with two channels, (3) Teflon outlet tube and (4) 5 mm outer diameter high pressure NMR tube. This tube was tested to support a pressure of 100 bar.

Preliminary tests of the system at variables pressures were conducted with a teflon tube of 4 m length (the distance between the polarizer and the NMR magnet) with 2.5 mm inner diameter (total volume 78.5 ml.) For a pressure of 6 bar, the sample is transferred in 1.2 s. This is the interval between the moments when the bolus triggers the two detectors D1 and D2. The graph in figure 41 gives the velocity as a function of the gas pressure. In the absence of high pressure connectors, it was not possible to

test the setup at pressures above 6 bar. According to the theory of the drop in pressure, well known in fluid engineering, the curve can be fitted to the equation :

$$\Delta P = \Lambda \frac{L\rho v^2}{2D}$$

where ΔP is the difference of pressure, corresponding here to the difference between the pressure applied to push the bolus and atmospheric pressure, Λ is the pressure drop factor which gives information about the resistance encountered by the fluid in the tube, L the length, ρ the density of the solution (mostly water), v the velocity of the transfer and D the diameter of the tube. The pressure drop factor is calculated to be $\Lambda = 0.066$. This value allows us to extrapolate the data to higher pressures ΔP . The extrapolation $\Delta P = 18$ bar, compared with the reference [27], give a velocity) $v = 5.8$ m/s, meaning that the sample could be transferred in ca. 0.7 s over a distance of 4 m. It would be possible to achieve such pressures when using special connectors like Flangless Fitting from *IDEX Health & Science LLC* that allows pressures up to 34 bar.

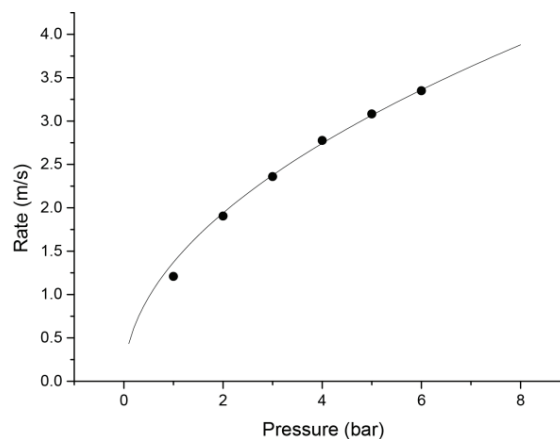


Fig. 41 Velocity v of the transfer as a function of the pressure of helium gas applied to push the liquid. The data are fitted to a parabola.

We noticed that the sample remains in one bolus during the transfer, which was not the case with our earlier design, where the sample was split into numerous droplets during the transfer. According to our visual observations, there is no turbulence between the liquid and gas phases with the new setup, so there that no droplets appear. However, we notice creation of drop after the first bolus transfer, staying in the Teflon tube.

Chapter 4: Transfer through a magnetic tunnel

As previously explained, the D-DNP experiment needs the sample to be dissolved. During the pushing to the NMR-spectrometer, the hyperpolarization inexorably returns to its equilibrium state. The decay follows a decreasing exponential function with the characteristic rate $R_1 = \frac{1}{T_1}$. The next section presents in detail the mechanisms of spin lattice relaxation and their interactions with different magnetic fields, especially low fields that occur during transfer.

a. Introduction

Following a perturbation of a spin system (by saturation or polarization by DNP), relaxation to its thermal equilibrium state occurs with a characteristic spin-lattice relaxation time T_1 .

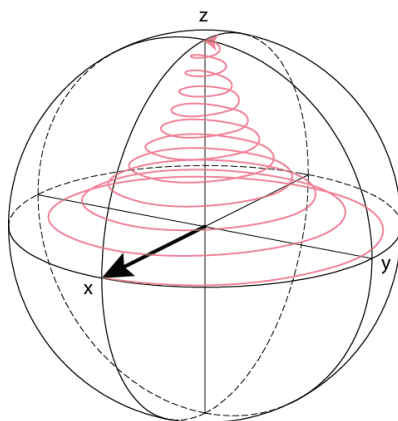


Fig. 41 Illustration of the return of the magnetization during relaxation.

After dissolution In D-DNP experiments, the hyperpolarized magnetization inexorably relaxes to the Boltzmann equilibrium through several mechanisms.

i. *Relaxation Mechanisms*

Several mechanisms are responsible for the longitudinal or spin-lattice relaxation ($R_1 \equiv T_1^{-1}$).

$$T_{Tot}^{-1} = T_{1,DD}^{-1} + T_{1,CSA}^{-1} + T_{1,Para}^{-1} + T_{1,SCQ}^{-1} \quad (2.7)$$

Where $T_{1,DD}^{-1}$, $T_{1,CSA}^{-1}$, $T_{1,Para}^{-1}$ and $T_{1,SCQ}^{-1}$ are respectively the contributions of dipolar relaxation (*DD*), chemical shift anisotropy (*CSA*), coupling with paramagnetic centers (*Para*) and scalar coupling with quadrupolar nuclei (*SCQ*). The dipolar coupling between two spins is given by Solomon's theory [28] :

$$T_{1,DD}^{-1} = \frac{6\pi}{10} b_{IS}^2 [J(\omega_I) + 4J(\omega_I + \omega_S)] \quad (2.8)$$

With

$$b_{IS} = -\frac{\mu_0 \gamma_I \gamma_S}{4\pi r_{IS}^3} \quad (2.9)$$

$$J(\omega_i) = \frac{\tau_c}{2\pi(1+\omega_i^2\tau_c^2)} \quad (2.10)$$

where γ_I and γ_S are the gyromagnetic ratios of spins *I* and *S* respectively, r_{IS} is the distance between the two spins and τ_c the correlation time. The CSA relaxation has a field-dependent effect according to Redfield theory [28]:

$$T_{1,CSA}^{-1} = \frac{2}{15} (\gamma_I B_0)^2 (\Delta\sigma)^2 \frac{\tau_c}{1+\omega_0^2\tau_c^2} \quad (2.11)$$

where γ_I is the gyromagnetic tensor, B_0 the external magnetic field, $\Delta\sigma$ the chemical shielding anisotropy and τ_c the correlation time.

Paramagnetic relaxation (Borah and Bryant [29]):

$$T_{1,Para}^{-1} = T_{1,trans}^{-1} + T_{1,rot}^{-1} \quad (2.12)$$

$$T_{1,trans}^{-1} = [M_{para}] J_d(0) \left[\frac{4}{3} j_d(\omega_I - \omega_S) + 4j_d(\omega_I) + 8j_d(\omega_I + \omega_S) \right] \quad (2.13)$$

With $[M_{para}]$ is the concentration of the paramagnetic species in spins per cm^3 ,

$$j_d(\omega) = \frac{J_d(\omega)}{J_d(0)} = \frac{15}{2} I(u) \quad (2.14)$$

and

$$J_d(0) = \pi \gamma_I^2 \gamma_S^2 \hbar^2 \frac{\tau_t}{50d^3} \quad (2.15)$$

τ_t is defined as $\tau_t = \frac{d^2}{D}$, with d the closest approach and D the diffusion coefficient.

$$T_{1,rot}^{-1} = \frac{\gamma_I^2 \gamma_S^2 \hbar^2}{10b^6} \left(\frac{nN}{N_0} \right) \left[\frac{3\tau_c}{1+\omega_I^2\tau_c^2} + \frac{\tau_c}{1+(\omega_I-\omega_S)^2\tau_c^2} + \frac{6\tau_c}{1+(\omega_S-\omega_I)^2\tau_c^2} \right] \quad (2.16)$$

Scalar coupling with quadrupolar nuclei [28, 30, 31] :

$$T_{1,SCQ}^{-1} = \frac{2(2\pi J_{IS})^2 S(S+1)}{3} \frac{T_{1(Q)}}{1+(\omega_I-\omega_S)^2 T_{1(Q)}^2} \quad (2.17)$$

With J_{IS} the scalar coupling and $T_{1(Q)}$ the relaxation time of quadrupolar spin.

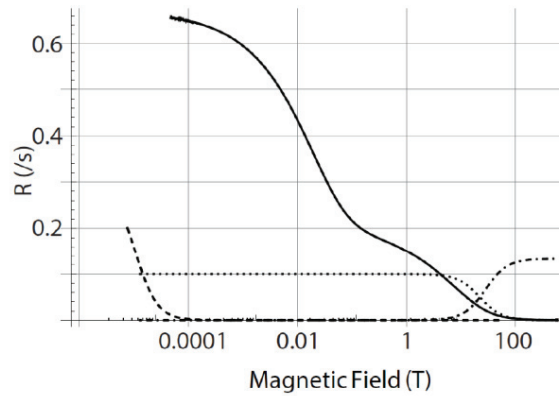


Fig. 42 Plots of relaxation mechanisms as a function of the magnetic field. Full line: paramagnetic relaxation. Dotted line: dipole-dipole relaxation. Continuous line: quadrupolar relaxation. Dashed-dotted line: CSA relaxation.

b. Designs of magnetic tunnels

The transfer of the hyperpolarized fluid from the polarizer to the detection magnet may cause dramatic losses of polarization since the magnetization decays through inexorable longitudinal spin-lattice relaxation with a field-dependent time constant T_1 . Apart from a system based on a dual magnet [32] where the transfer can occur in less than a second, most polarizers are placed at a few meters distance from the NMR or MRI apparatus. The transfer times can therefore vary between a few seconds [33] and about a minute [34], depending on the handling of the hyperpolarized fluid, which may be pushed by a pressurized gas, carried manually, or filtered and neutralized. During the transfer, the hyperpolarized solution is no longer immersed in the magnetic field of the polarizer (typically between 3.35 and 6.7 T) and not yet sheltered by the field of the detection magnet (typically 1.5 to 18.6 T). During the transfer, the hyperpolarized sample may be exposed to very low magnetic fields (e.g., the Earth's magnetic field) or even to a vanishing field (e.g., if the two magnets have opposite polarity), depending on many parameters such as the design of the magnets (unshielded or actively shielded) and their relative

orientations (fields pointing up or down). In field shuttling experiments this low-field region has pertinently been referred to as '*death valley*' [35]. The hyperpolarization is likely to perish in this a hostile territory because various nuclear spin-lattice relaxation pathways may be exacerbated at low fields, including paramagnetic effects, scalar relaxation, etc.

In order to shield hyperpolarized solutions from such relaxation mechanisms, we have designed a modular '*magnetic tunnel*' to interface our home-built 6.7 T polarizer either to an unshielded 300 MHz or to an ultra-shielded 500 MHz high-resolution NMR spectrometer (see figure 43).

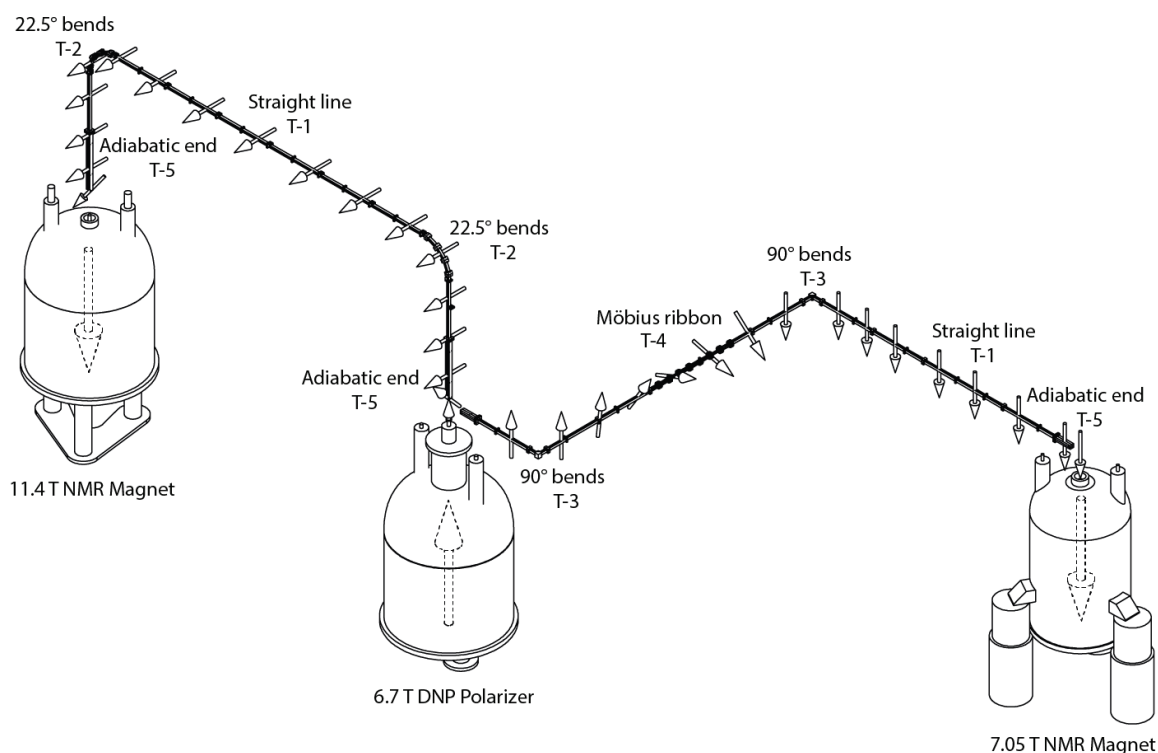


Fig. 43 Experimental arrangement in our laboratory consisting of a 6.7 T DNP polarizer (middle) coupled to an unshielded 300 MHz spectrometer (left) or to an ultra-shielded 500 MHz magnet (right), either through a 'vertical' magnetic tunnel, i.e., with a vertical entrance and exit (left) or through a 'horizontal' magnetic tunnel (right). The arrows that show the adiabatic changes of the direction of the magnetic field along the path are not drawn to scale. Since the two magnets on the right side have opposite static fields, the direction of the field is rotated adiabatically in a series of segments arranged in the manner of a Möbius ribbon. This is not necessary for the two magnets on the left side.

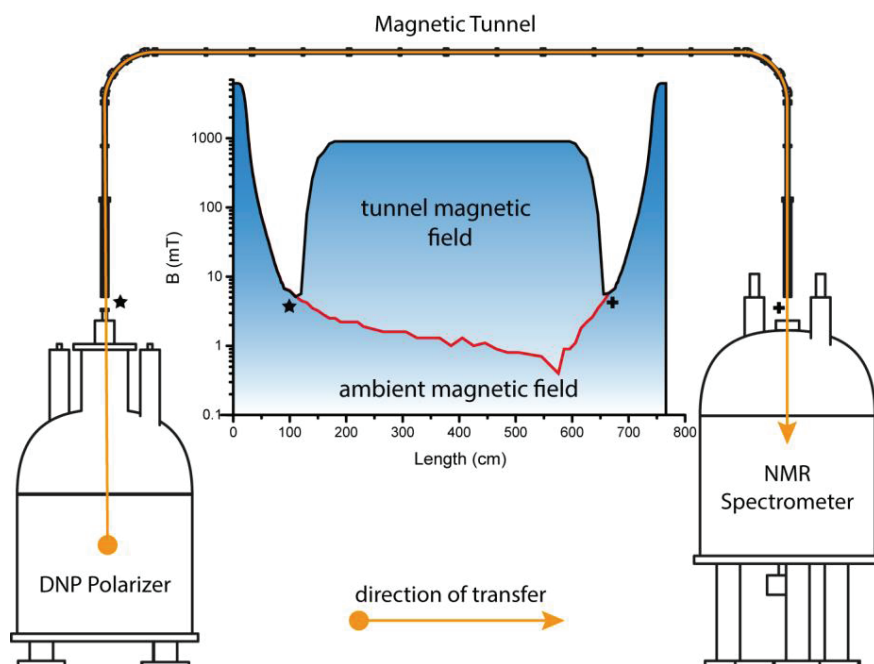


Fig. 44 The magnetic field strength in the course of the transfer of the hyperpolarized fluid from the DNP polarizer to the unshielded 300 MHz NMR spectrometer through a magnetic tunnel (black line) or without tunnel (red line). The star and cross indicate the polarizer-tunnel and tunnel-spectrometer junctions. Details of the orientation of the magnetic fields at the entrance and exit of the tunnel are shown in Figs. 47 and 49.

i. Magnetic field mapping

The stray magnetic fields in an NMR or MRI laboratory depend on many parameters. During a dissolution-DNP experiment, the hyperpolarized fluid must travel through the space between two magnets. The fate of the hyperpolarization depends on the strength and orientation of the stray fields. We have mapped the field between our polarizer and an unshielded 300 MHz NMR spectrometer using a triple-axis Hall probe (Sentron Digital 3D Teslameter, Type: 3MS1-A2-D3) using custom-designed National Instrument LabVIEW software.

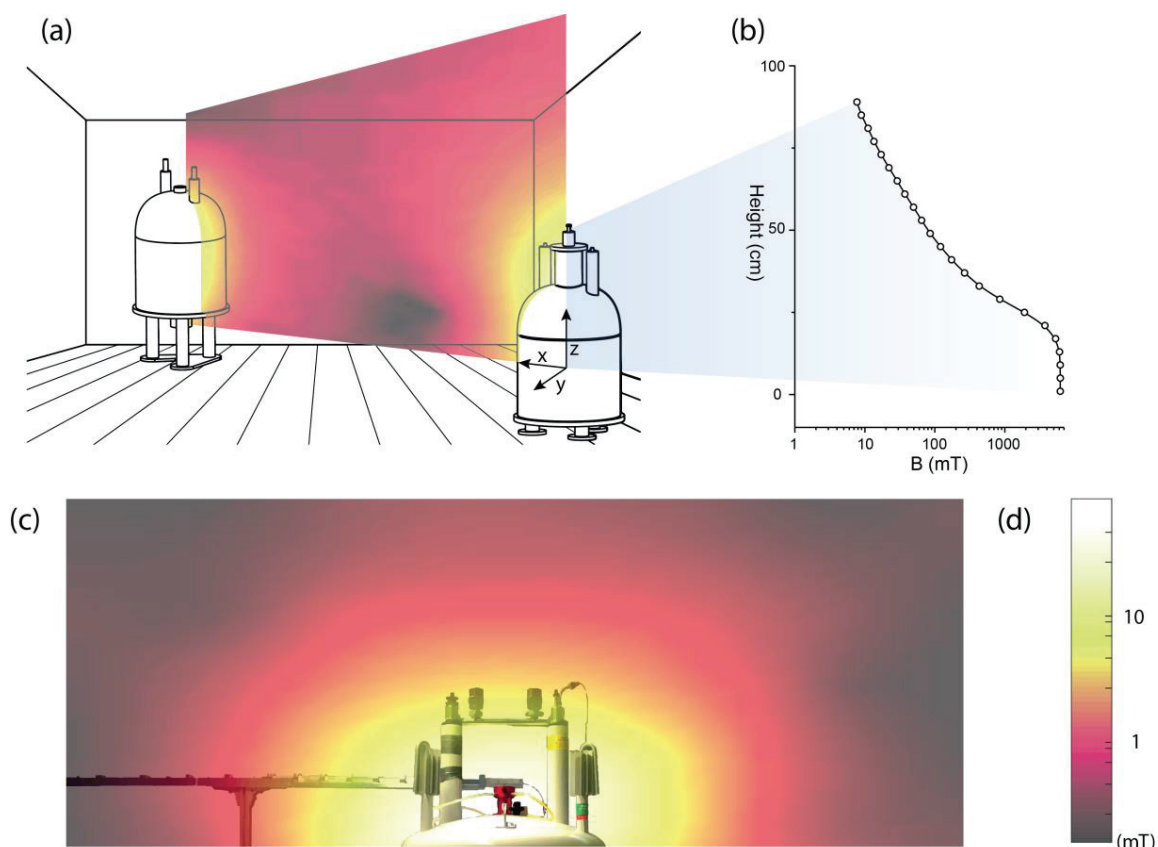


Fig. 45 a) The complete space between our 300 MHz spectrometer and the polarizer has been measured. The two supraconducting magnets have opposite directions. This explains the *zero field hole*. The ambient field decrease rapidly under 1 mT after just 1 m. b) the field along the vertical line in the polarizer. c) The field in the proximity of our ultrashielded 500 MHz magnet. Here the field decreases dramatically under 0.5 T (the limit of detection of our Hall probe). d) The color scale used for mapping.

ii. *Relaxometry*

Paramagnetic impurities affect the longitudinal relaxation of nuclei. This phenomenon is exploited in MRI by using contrast agents such as gadolinium complexes. But in our case, relaxation is undesirable, and losses of polarization during the transfer must be kept to a minimum. For DNP we obviously need polarizing agents such as TEMPO, Trityl, etc., but their presence is no longer desirable after dissolution. With a custom-built shuttle relaxometer [5] operating in the stray field of an unshielded 300 MHz wide-bore Oxford Instruments magnet, we have studied the ^1H nuclear spin-lattice relaxation of bromothiophene carboxylate (BTC) (Sigma Aldrich) over a range $1 \text{ mT} < B_0 < 7.05 \text{ T}$. The shuttle can lift the NMR sample with a stepper motor so that it reaches a field of 1 mT within *ca.* 1 s. Details about such measurements are given elsewhere [5]. Three samples were prepared, based on a 50 mM stock

solution of bromothiophene carboxylate in non-degassed D₂O. Sample 1 without any additions, sample 2 with the addition of 0.25 mM 4-hydroxy-2,2,6,6-tetramethylpiperidine 1-oxyl (TEMPO) (Sigma Aldrich), and sample 3 with the addition of 50 mM sodium ascorbate (Sigma Aldrich) which acts as scavenger that quenches both TEMPO and dissolved O₂ [36]. As discussed below, dissolution-DNP experiments are usually performed with frozen pellets containing 50 mM TEMPO in addition to the analyte, with a typical volume $0.1 < v < 0.5$ mL, that are subsequently dissolved with 5 mL of hot D₂O or H₂O. The final TEMPO concentration therefore usually ranges between 1 and 5 mM. In order to minimize relaxation during the relatively slow displacements of the shuttle, we decreased the TEMPO concentration to 0.25 mM (4 to 20 times below the usual concentrations in routine dissolution-DNP experiments) so that the paramagnetic contribution to the relaxation rate is $R_1^{\text{para}} < 1 \text{ s}^{-1}$. The relaxation rates $R_1(^1\text{H})$ of bromothiophene carboxylate were measured in ten different magnetic fields $B_0 = 7.05, 1.0, 0.4, 0.10, 0.022, 0.01, 0.004, 0.002, \text{ and } 0.001 \text{ T}$. A single acquisition of the ¹H spectrum at 7 T sufficed for each data point.

Figure 46 shows the longitudinal relaxation rates $R_1(^1\text{H}) = 1/T_1(^1\text{H})$ in bromothiophene carboxylate (BTC.) In sample 3, where the paramagnetic oxygen has been scavenged by sodium ascorbate, $T_1(^1\text{H})$ is independent of the magnetic field down to 1 mT. However, samples 1 and 2 show a pronounced field dependence, which can be attributed to the presence of dissolved paramagnetic oxygen and TEMPO. One can distinguish three different contributions to relaxation: (1) a field-independent intramolecular contribution $R_1^{\text{intra}} = 0.1 \pm 0.01 \text{ s}^{-1}$, (2) a field-dependent paramagnetic contribution due to dissolved oxygen, increasing from $R_1^{\text{para}} = 0.08 \pm 0.01 \text{ s}^{-1}$ at $B_0 = 1 \text{ T}$ to $R_1^{\text{para}} = 0.1 \pm 0.01 \text{ s}^{-1}$ at 1 mT, and (3) a field-dependent paramagnetic contribution due to 0.25 mM TEMPO increasing from $R_1^{\text{para}} = 0.1 \pm 0.05 \text{ s}^{-1}$ at $B_0 = 1 \text{ T}$ to $R_1^{\text{para}} = 0.4 \pm 0.05 \text{ s}^{-1}$ at 1 mT. For a more realistic TEMPO concentration of 2 mM expected after dissolving 200 μL of frozen pellets with 5 ml of D₂O, this can be extrapolated to $R_1^{\text{para}} = 0.8 \pm 0.4 \text{ s}^{-1}$ at $B_0 = 1 \text{ T}$ and $R_1^{\text{para}} = 3.2 \pm 0.4 \text{ s}^{-1}$ at 1mT.

This example is representative of the exacerbated relaxation at low magnetic fields during transfer in dissolution-DNP experiments. As a remedy to this detrimental effect, we have proposed the use of vitamin C (sodium ascorbate) as a scavenger [36] during dissolution, which turned out to be a useful approach when hyperpolarizing nuclei with long T_1 such as ¹³C. However, the scavenging process may takes several seconds to complete, an interval during which paramagnetic relaxation is still active and drives the hyperpolarization back towards thermal equilibrium. Obviously, as illustrated in figure 46 for the case of ¹H spins in BTC, and more generally for protons in small molecules, the interval where hyperpolarized molecules are exposed to the effects of concentrated radicals at low magnetic field cause painful losses of priceless polarization.

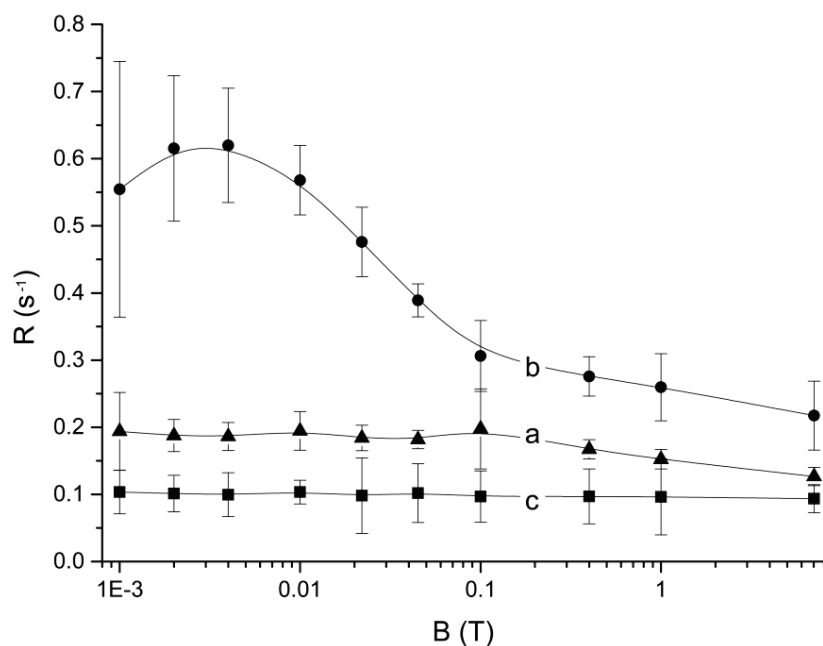


Fig. 46 Longitudinal proton 'spin-lattice' relaxation rates $R_1(^1\text{H}) = 1/T_1(^1\text{H})$ of bromothiophene carboxylate (BTC) (Sigma Aldrich) determined with a home-built relaxometer [5] as a function of the static field B_0 expressed on a logarithmic scale. (a) Triangles for sample 1 containing 50 mM bromothiophene carboxylate in D_2O with naturally dissolved O_2 ; (b) Dots for sample 2 after addition of 0.25 mM TEMPOL; (c) Squares for sample 3 after addition of 30 mM sodium ascorbate to scavenge radicals and paramagnetic oxygen

iii. Magnetic tunnel structure

Our magnetic tunnel consists of an assembly of permanent neodymium boron magnets (Supermagnete Webcraft GmbH, 5x5x100 mm, NdFeB, N52, with Ni-Cu-Ni coating) securely maintained by several home-built aluminum structures. The permanent magnets are positioned in four rows following a simplified Halbach design [37], and oriented to maximize the magnetic field strength in the center, where $B_{\text{tunnel}} > 0.9 \text{ T}$ (see figure 47a). A hollow cylinder with a 3 mm inner diameter runs through the center of the aluminum structure to guide a 2.5 mm outer diameter PTFE ('Teflon') tube (Maagtechnic AG 10075652) that carries the hyperpolarized fluid. The design comprises five different modular segments T-1 to T-5: straight sections of 50 cm length (T-1, see figure 47b), bent sections with an angle of 22.5° (T-2, see figure 47c) or 90° (T-3, see figure 47d) where the magnetic field is perpendicular to the plane of the bend, so that the field vectors remain parallel. The choice between a single 90° bend or a series of 22.5° bends depends the constraints of the laboratory. To minimize the loss of charge during fluid transfer, it is optimize to a small angle than 90° .

Special attention must be paid to variations of the magnetic field at the entrance and exit of the tunnel. The adiabatic condition (*vide infra*) must be fulfilled throughout, and zero-field crossings should be avoided, in particular at the entry and exit of the tunnel. In order to avoid zero-field crossings when the stray fields have opposite orientations (as for our DNP polarizer and NMR magnets), we have designed a 22.5° axial twist section of 10 cm length (T-4, see figure 47e). A cascade of eight axial twist sections allows one to achieve a 180° rotation of the field, in the manner of a Möbius ribbon (see figure 43.) Without 180° rotation, the magnetic field would inevitably cross through zero at one of the ends of the tunnel. Finally, we have designed a tunnel section (T-5, see figure 47f) where the magnetic field is gradually increased from 0 to 0.9 T, so as to fulfill the adiabatic condition even if the sample is transferred very rapidly at a velocity of, say, 10 m.s⁻¹. These segments can be assembled in a flexible way to accommodate the dimensions of individual laboratories.

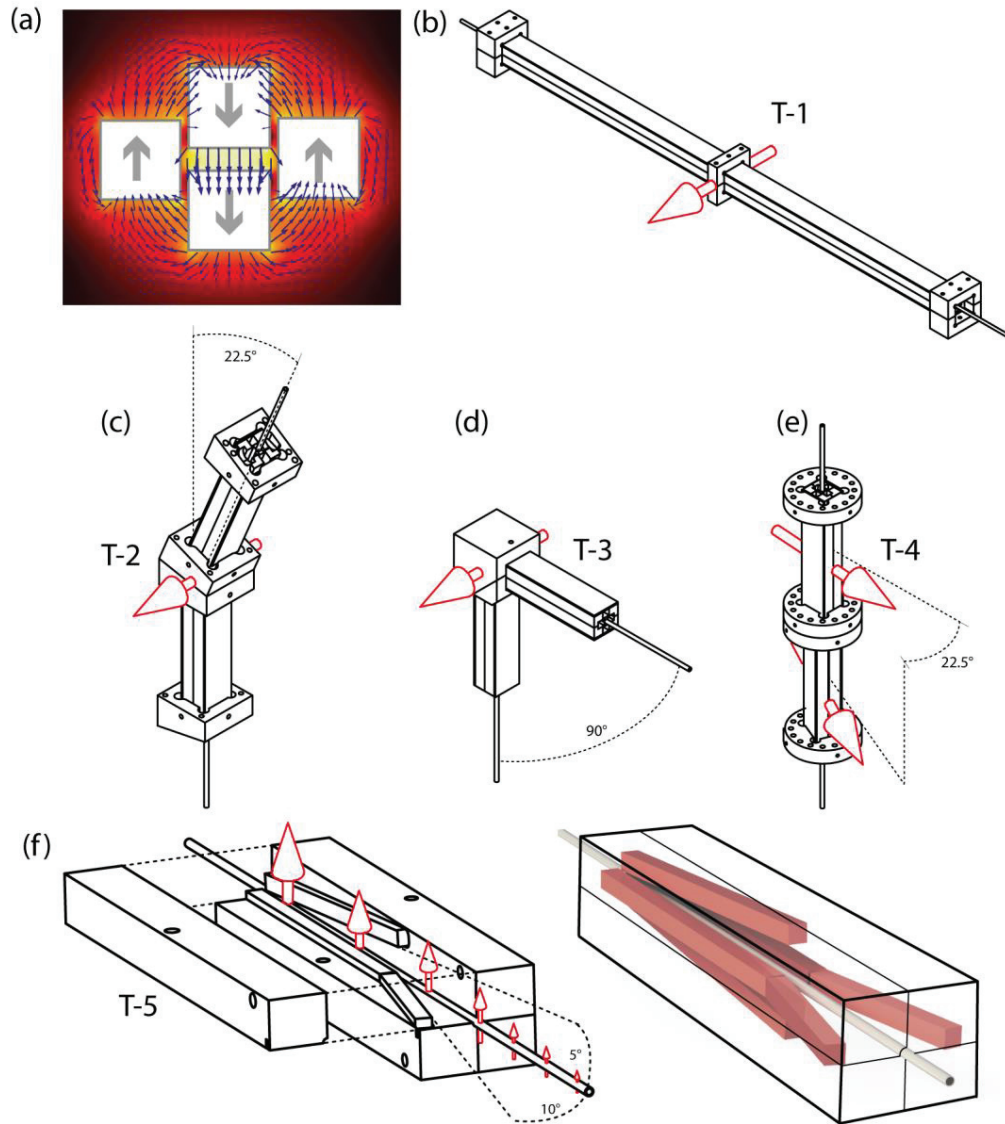
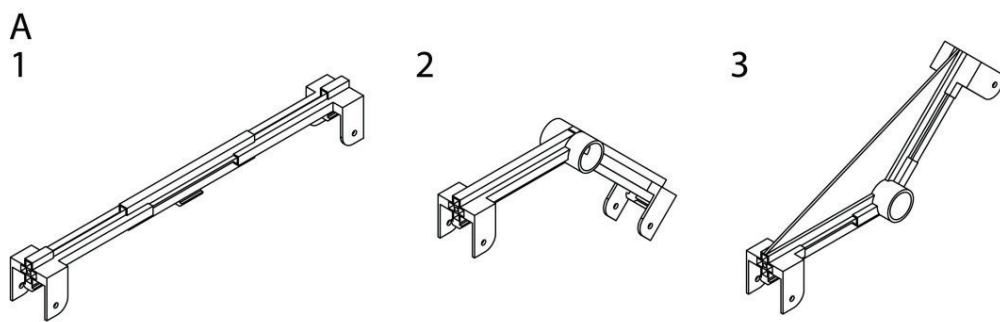


Fig. 47 (a) Simulations (Comsol Multiphysics) showing the magnetic field vectors in a magnetic tunnel where permanent magnets (5x5x100 mm, NdFeB) are positioned in four rows following a simplified Halbach design. The magnets are positioned to maximize the magnetic field strength in the center ($B_{\text{tunnel}} > 0.9$ T.) A 2.5 mm outer diameter PTFE ('Teflon') tube carries the hyperpolarized fluid. Various magnetic tunnels can be assembled using four different modular segments: (b) Linear segment of 50 cm length. (c) Segment with 22.5° bend. (d) Element with 90° bend. (e) Segment with 22.5° axial twist. (f) Adiabatic section at the entrance or exit of the tunnel where the magnets are positioned so as to diverge from the central tube. The left figure shows the aluminum support where one quarter has been removed to show the internal structure. The right figure shows the internal arrangement of the magnets. The red arrows show the direction of the field.

The first generation of our tunnels was built in aluminum, A second generation of magnetic tunnels is now printed in 3D. The first 3D printed system was built at EPFL and installed at ENS in Paris. There are three different parts (figure 48 A): a linear segment of 30 cm length, a segment with a bend 135° and a segment with a bend 225°. The pieces are designed to be inserted into a commercial aluminum structure commonly used in scientific or industrial domains.



B



C



Fig. 48 A : Linear segment of 30 cm length (1), segment with a bend smaller than 45° and a segment with a bend larger than 45° . B: photograph of an implementation of this kind of tunnel, here the tunnel to the 800 MHz spectrometer installed at ENS Paris. C: photograph of the last part of the same tunnel.

iv. *Adiabatic condition*

The main purpose of the magnetic tunnel is to prevent losses of polarization at low fields, by providing a minimum field ($B_{\text{tunnel}} > 0.9$ T) that is sufficient to sustain the hyperpolarization during transfer. However, a sudden change of the direction of the magnetic field may cause a loss of magnetization if the rate of change is comparable to the Larmor frequency. Therefore, particular care has been taken to design the entrance and exit of the tunnel where the magnetic field may change abruptly. The T-5 segment (see figure 42f) offers a way to increase or decrease the magnetic field in such a way that the following condition of adiabaticity is always fulfilled [38] :

$$\frac{1}{B^2} \left| \vec{B} \times \frac{d\vec{B}}{dt} \right| \ll \gamma B \quad (2.18)$$

where $B = |\vec{B}_{\text{stray}} + \vec{B}_{\text{tunnel}}|$ is the total magnetic field. The Larmor frequency is $\gamma B / (2\pi) = 4.26$ kHz for protons if $B = 100$ μ T. The adiabatic condition is obviously more critical for low-gamma nuclei such as carbon-13 or nitrogen-15 that are popular for dissolution DNP. We define a dimensionless adiabatic ratio

$$A = \left| \vec{B} \times \frac{d\vec{B}}{dt} \right| / \gamma B^3 \quad (2.19)$$

which should be kept as small as possible, preferably $A < 1$. Note that A is proportional to the speed of the transfer of the sample through the PTFE tube. Figure 49 illustrates how the entrance and exit of the magnetic tunnel raises delicate issues that can be solved by inserting an adiabatic T-5 section. Figure 49b shows the magnetic field profile (black line) at the entrance of a straight T-1 section. The first striking feature is that, just before the entrance, the magnetic field has a sign that is opposite ($B_{\text{out}} = -60$ μ T) to the magnetic field inside the section ($B_{\text{tunnel}} > +0.9$ T). A hyperpolarized sample entering into such a straight T-1 section therefore inevitably undergoes a detrimental zero-field crossing. This does not matter if the entrance of the tunnel is placed in a stray field of a superconducting magnet $B_{\text{stray}} > B_{\text{out}}$, provided that B_{stray} is not anti-parallel with respect to B_{tunnel} . A second striking feature of figure 49b is the sudden increase in magnetic field at the entrance. The magnetic field increases to $B_{\text{tunnel}} > +0.9$ T in a quasi-instantaneous manner. Unless the magnetic field outside the tunnel $B_{\text{out}} +$

B_{stray} is parallel to B_{tunnel} , such an abrupt change in the strength of the magnetic field will be accompanied by a sudden change in its direction. Figure 49 also shows (red lines) the adiabatic factor A of Eq. (2) calculated for a scenario where B_{stray} is perpendicular to B_{tunnel} . We show in figure 49a that both issues of zero-field crossings and abrupt field changes can be overcome by using an adiabatic T-5 section rather than a simple straight T-1 section. In this example, $A \sim 10^{-3}$. Unfortunately, as shown in figure 43, the DNP polarizer (Oxford instruments) has a polarity opposite to both 300 and 500 MHz NMR spectrometers (Bruker BioSpin). For the 300 spectrometer we used a 'vertical' tunnel (see figure 43) where B_{stray} and B_{tunnel} are perpendicular so that no zero-crossings occur. For the 500 MHz NMR spectrometer, space restrictions forced us to use a 'horizontal' configuration. If B_{stray} and B_{tunnel} are anti-parallel, the only way to avoid a zero-field crossing is to reverse the direction of B_{tunnel} . This was achieved by inserting eight 22.5° axial twist sections (T-4) to rotate the magnetic field through 180° , so as to match the opposite orientations of the stray fields at the two ends of the tunnel.

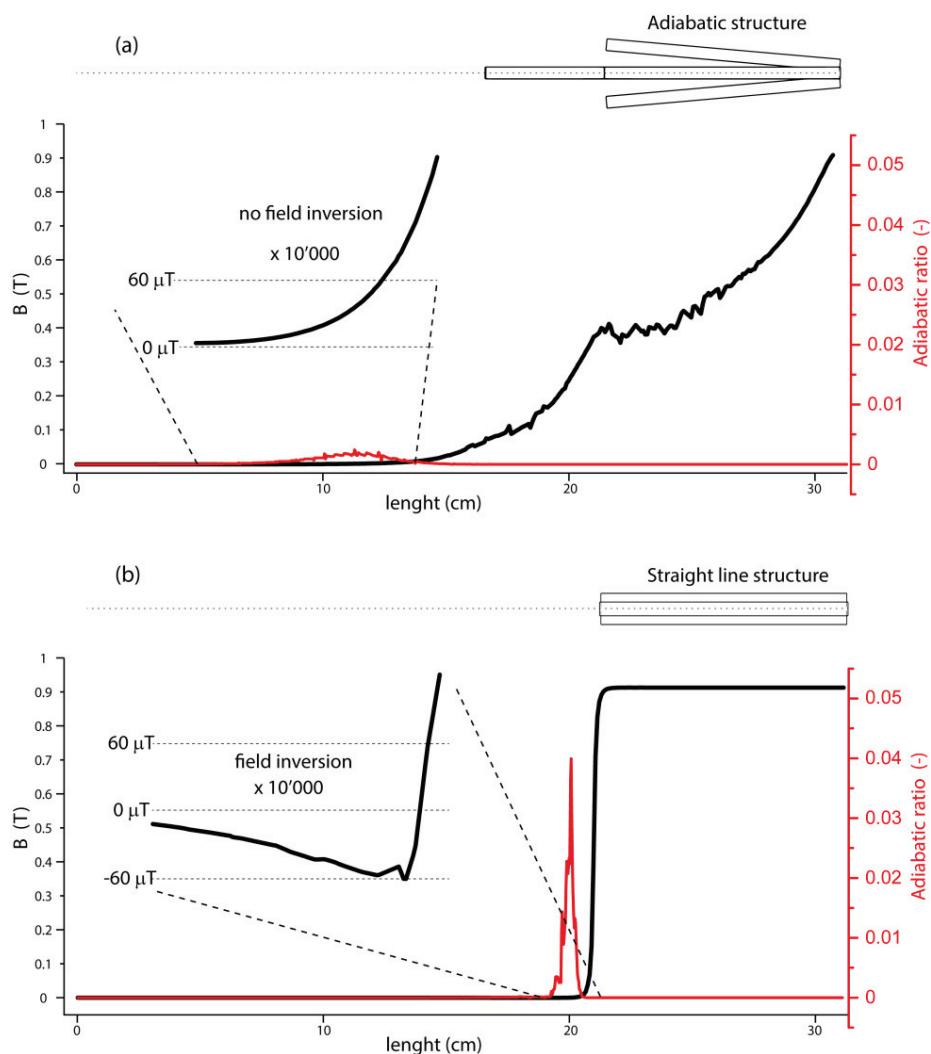


Fig. 49 Simulations of the magnetic field (black lines) and of the adiabatic ratio A of Eq. (2) (red lines) at the entrance or exit of the magnetic tunnel for (a) an adiabatic section (see figure 42f) and (b) a straight section (see figure 42b). The adiabatic ratio A , which must be smaller than 1, is proportional to the speed of the sample transfer. It is shown here for a realistic speed of 10 m/s.

(d) Dissolution-DNP experiments. Three DNP solutions were prepared to test the advantages of the magnetic tunnel for dissolution-DNP experiments. Solution 4 contained 1 M bromothiophene carboxylate (BTC) (Sigma Aldrich) and 50 mM TEMPOL in DMSO- d_6 /D $_2$ O (60/40 v:v). Solution 5 contained 1 M alanine-glycine (Sigma Aldrich) and 50 mM TEMPOL in ethanol- d_6 /D $_2$ O (50/50 v:v), and solution 6 contained 3 M 13 C-labeled Urea and 50 mM TEMPOL in DMSO- d_6 /D $_2$ O (60/40 v:v). The DNP solutions were rapidly frozen to form 10 μ L pellets in liquid nitrogen, and 20 pellets (total sample volume of 200 μ L) were loaded in the cryostat of our 6.7 T polarizer that was pre-cooled to $T = 4.2$ K. The cryostat was further cooled down to $T = 1.2$ K and microwave irradiation was applied during 20 minutes with an input power $P_{\mu w} = 87$ mW at a monochromatic irradiation frequency $f_{\mu w} = 188.3$ GHz to induce the strongest possible (negative) proton polarization. The proton DNP build-up curves were

measured at $T = 2.2$ K and $B_0 = 6.7$ T with 5° pulses applied every 5 s. Dissolution was subsequently performed with 5 mL D_2O preheated to *ca.* $T = 450$ K at a pressure of 1 MPa. The hyperpolarized liquid bolus was propelled with helium gas at 0.6 MPa to either 300 or 500 MHz spectrometers, both at a distance of *ca.* 5 m. Two distinct PTFE ('Teflon') transfer tubes, both with 1.5 inner diameters, were used: one running through one of the magnetic tunnels, the other running loosely between the polarizer and either of the two spectrometers. After settling for *ca.* 2 s, the sample was injected into 5 mm NMR tubes using home-built injection devices. The typical intervals in this sequence are: dissolution in 0.7 s, transfer in 5 s, and injection in 2.5 s. The decay of the 1H NMR signal was measured every 5 s with 5° pulses.

v. *Results and Discussion*

The field along the magnetic tunnel depends on the configuration of the superconducting magnets and their shielding. The graphs in figures 44 and 45a show the magnitude of the magnetic field (without magnetic tunnel) in the plane between our DNP polarizer (unshielded 6.7 T magnet) and our 300 MHz NMR spectrometer (unshielded 7.05 T magnet). Even though the two magnets are unshielded in this case, the magnetic field drops below $B_0 = 1$ mT. A similar measurement between our polarizer and ultra-shielded 500 MHz magnet (shown in figure 45c) indicates that the field drops as low as $B_0 < 0.5$ mT.

In order to study the detrimental effects of increased relaxation at low field during transfer, we have performed dissolution-DNP experiments with solutions 4 and 5 containing 1H spins in an assortment of molecules, with and without magnetic tunnel. In all cases, the polarization process yielded a nuclear spin polarization $P(^1H) > 60\%$ with a typical build-up time constant $\tau_{DNP} = 280 \pm 10$ s. The advantage of a transfer through a magnetic tunnel, compared to a transfer through a low field region, can be expressed in terms of an enhancement factor $\epsilon_{tunnel}(^1H)$ or $\epsilon_{tunnel}(^{13}C)$. Figures 50 and 51 show 1H and ^{13}C spectra and molecular structures of various hyperpolarized molecules in solutions 4, 5, and 6, obtained with and without magnetic tunnel. The spin-lattice relaxation times $T_1(^1H)$ or $T_1(^{13}C)$ measured in high field and the tunnel enhancement factors $\epsilon_{tunnel}(^1H)$ or $\epsilon_{tunnel}(^{13}C)$ are reported in tables 7 and 8.

Molecule	DMSO-d ₆ (HD ₂ C)	BTC (H ^a)	BTC (H ^b)	AlaGly (H ^α Gly)	AlaGly (H ^α Ala)	AlaGly (CH ₃)	ETOH-d ₆ (CDH)	ETOH-d ₆ (HD ₂ C)	HDO
$T_1(^1\text{H})$ (s)	13.2±0.02	5.7±0.1	6.0±0.1	6.0±0.1	4.1±1.4	-	4.0±0.4	4.3±0.3	3.6±0.1
$\epsilon_{\text{tunnel}}(^1\text{H})$	2.1	1.5	12.2	1.8	9.0	1.0	10.2	8.6	25.3

Table 8 Longitudinal relaxation times $T_1(^1\text{H})$ and enhancement factors $\epsilon_{\text{tunnel}}(^1\text{H})$ measured after hyperpolarization and dissolution at room temperature at 500 MHz ($B_0 = 11.7$ T) in solutions containing approximately 2 mM TEMPOL. BTC stands for bromothiophene carboxylate.

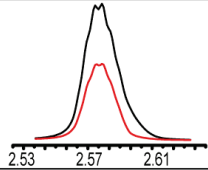
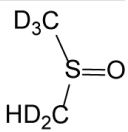
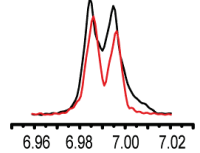
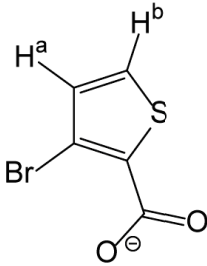
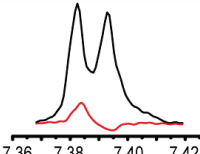
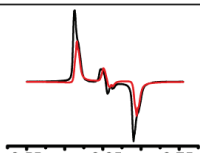
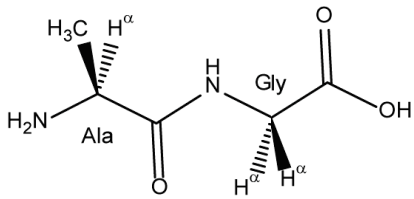
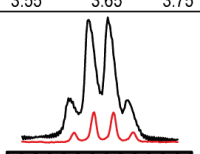
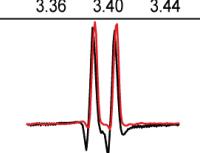
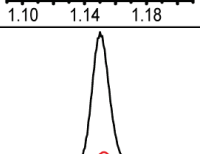
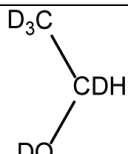
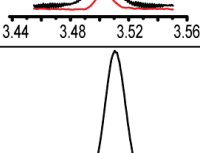
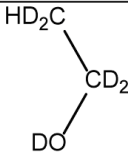
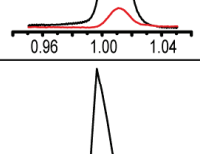
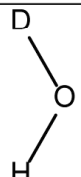
¹ H spectra with/without tunnel	Molecule	Structure
	DMSO-d ₆ (HD ₂ C)	
	BTC (H ^a)	
	BTC (H ^b)	
	AlaGly (H ^α Gly)	
	AlaGly (H ^α Ala)	
	AlaGly (CH ₃)	
	ETOH-d ₆ (CDH)	
	ETOH-d ₆ (HD ₂ C)	
	HDO	

Fig. 50 Proton NMR spectra obtained after hyperpolarization and dissolution with and without magnetic tunnel, shown in black and red, respectively.

Molecule	Urea	DMSO-d ₆
$T_1(^{13}\text{C})$ (s)	31.5 ± 1.9	26.9 ± 1.4
$\epsilon_{\text{tunnel}}(^{13}\text{C})$	1.3	1.2

Table 9 Longitudinal relaxation times $T_1(^{13}\text{C})$ and enhancement factors $\epsilon_{\text{tunnel}}(^{13}\text{C})$ measured after hyperpolarization and dissolution at room temperature at 500 MHz ($B_0 = 11.7$ T) in solutions containing approximately 2 mM TEMPOL.

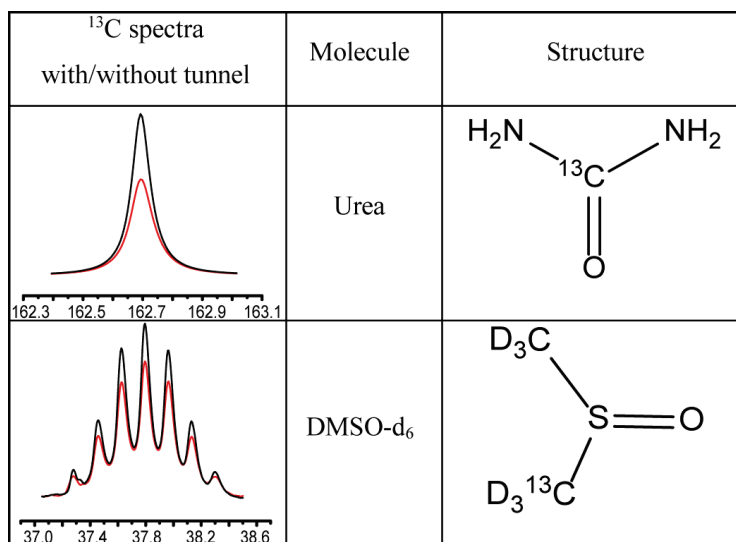


Fig. 51 ¹³C NMR spectra obtained after hyperpolarization and dissolution with and without magnetic tunnel (black and red lines, respectively).

To our surprise, the enhancement factors vary significantly from case to case, with two extreme examples of the fully protonated methyl group of AlaGly with $\epsilon_{\text{tunnel}}(^1\text{H}) = 1.0$ and the residual protons in 99.9% deuterated water with $\epsilon_{\text{tunnel}}(^1\text{H}) = 25.3$ (table 8). These two examples are instructive and can be readily understood. The relaxation of the fully protonated methyl group of AlaGly is not significantly affected by the presence of free radicals since relaxation through intramolecular ¹H-¹H dipolar interactions is dominant. On the other hand, the residual protons in HDO mainly relax through paramagnetic interactions with dissolved oxygen and TEMPOL. Indeed, when TEMPOL and oxygen are scavenged by vitamin C, the spin-lattice relaxation time in HDO at 7 T increases from $T_1(^1\text{H}) = 3.6$ to 14 s. As an alternative to scavenging, we have shown recently that paramagnetic relaxation can also be prevented by replacing the soluble TEMPOL by hybrid polarizing solids (HYPSOs) that can be eliminated by on-line filtration during the dissolution process [39].

It is therefore natural that hyperpolarization losses during transfer are largely alleviated by using a magnetic tunnel in the case of HDO, but not in the case of CH₃. A more detailed analysis could be performed from case to case, with a full calculation of paramagnetic relaxation which would depend

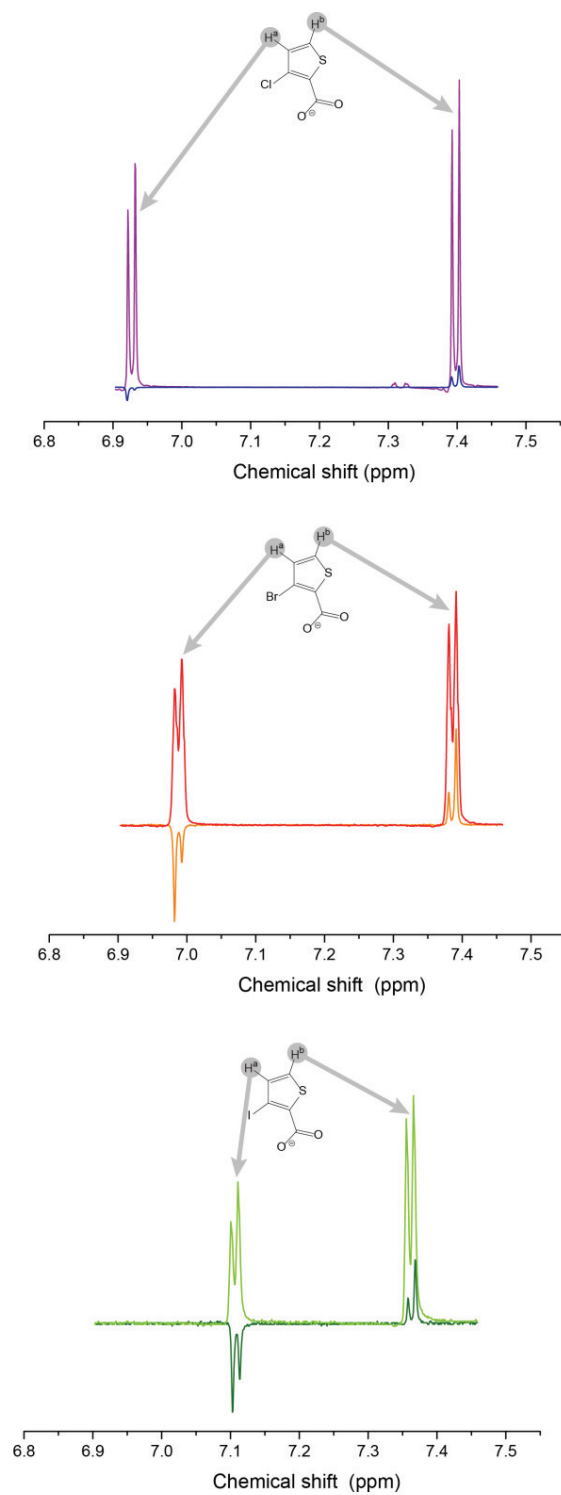
on a myriad of parameters such as (1) the distance d of closest electron-proton approach, (2) the mutual electron-proton translational diffusion constant D , (3) the magnetic field along the transfer and (4) the speed of the transfer. The results for ^{13}C nuclei reported in table 9 are far less impressive in terms of enhancements, with $\epsilon_{\text{tunnel}}(^{13}\text{C}) \leq 1.3$. This can be explained by the ^{13}C nuclear spin-lattice relaxation times that tend to be longer than the transfer times, even at low magnetic fields. It is worth stressing that for extended transfer times (for example when hyperpolarized fluids must be manipulated for filtration, etc., in fairly low magnetic fields) relaxation effects can become significant even for ^{13}C , as recently reported by Chiavazza *et al.*[30]. The general trend in table 8 is that for isolated ^1H spins as well as for pairs of equivalent ^1H spins, the use of our magnetic tunnel can be recommended. However, there are some cases that deserve further investigation: (1) the H^{a} proton of the Gly residue in AlaGly benefits from the use of the magnetic tunnel since $\epsilon_{\text{tunnel}}(^1\text{H}) = 1.8$, although its antiphase pattern (which suggests an admixture of I_z and $2I_zS_z$ terms) has not been rationalized so far; (2) the signal of H^{b} in BTC was almost completely wiped out when the magnetic tunnel is not used (hence the favorable ratio $\epsilon_{\text{tunnel}}(^1\text{H}) > 12$), whereas the signal of H^{a} merely suffered moderate losses in the absence of magnetic tunnel ($\epsilon_{\text{tunnel}}(^1\text{H}) = 1.5$). Previous studies suggest that these effects could be due to scalar couplings with quadrupolar nuclei at low field, [30] in this example bromine or nitrogen-14. Such scalar relaxation effects can be attenuated by using our magnetic tunnel. Another interesting way to make hyperpolarization immune to very low fields, so that there would be no need for a magnetic tunnel, is to store the polarization in the form of 'equivalent hyperpolarized long-lived states' (HELLS)[39]. However, these approaches are limited to analytes that fulfill demanding conditions of molecular symmetry. The use of magnetic tunnels appears to offer a more universal solution at the time of writing.

c. Effects in systems with quadrupolar nuclei

The study of bromothiophene gave astonishing results for H^b (figure 50) as well as H^a Gly in AlaGly (figure 50). We notice that this antiphase term is only observed in two spin systems. Another observation, mentioned in *Chapter 4, Section b.v.*, is the fast relaxation at low field of protons coupled with quadrupolar nuclei. We therefore decided to investigate different thiophenes with a variety of quadrupolar nuclei. To enhance the effects of quadrupolar relaxation, we used an anti-tunnel composed by two iron tubes to create a magnetic shield. The field inside the anti-tunnel is smaller than we can detect with our Hall probe ($B < 0.5$ mT). Solutions 1, 2, and 3, contained 1 M bromothiophene carboxylate (BTC) (Sigma Aldrich), 1 M chlorothiophene carboxylate (Sigma Aldrich), and 1 M iodothiophene carboxylate (Sigma Aldrich), respectively. All three solutions contain 50 mM TEMPOL in DMSO- d_6 /D $_2$ O (60/40 v:v) for 200 μ l. Table 10 gives the properties of the Br, Cl and I isotopes.

	Chloride	Bromine	Iodine
Atomic number	17	35	53
Spin	$3/2$ (^{35}Cl and ^{37}Cl)	$3/2$ (^{79}Br and ^{81}Br)	$5/2$ (^{127}I)
Typical T_1	$\sim 10 \mu\text{s}$	$< 1 \mu\text{s}$	$< 1 \mu\text{s}$

Table 10 Properties of Chloride, Bromine and Iodine isotopes, all of which have large quadrupole interactions. According to Lindman and Forsen [3] their typical T_1 's are very short, on the order of a few μs .



AT = Anti-Tunnel ($B < 0.0005$ T) — Chloro AT — Bromo AT — Iodo AT
 MT = Magnetic Tunnel ($B=0.9$ T) — Chloro MT — Bromo MT — Iodo MT

Fig. 52 ^1H spectra of bromothiophene, chlorothiophene and iodothiophene in D-DNP experiments using a magnetic tunnel (MT) ($B = 0.9$ T) or an anti-tunnel (AT) ($B = < 0.0005$ T).

The difference between the spectra is spectacular. With the tunnel, a relatively normal spectrum is measured. However, the anti-tunnel gives interesting results, since one observes antiphase peaks. A beginning of an answer is given here. The experiment here uses a simple 90° pulse. The detected terms are I_x and $I_x S_z$. Initially, before the 90° pulse, one has I_z and $I_z S_z$ along the z-axis. In standard NMR experiments, without using specific pulse sequences, the $I_z S_z$ term is negligible. However, the importance of $I_z S_z$ varies as a function of the polarization [40]. During DNP, at high polarization, the $I_z S_z$ becomes important and is directly measurable with a 90° pulse. During the transfer, different parameters come into play. The initial state includes I_z and $I_z S_z$ states. At low field, the protons could couple with the quadrupolar nuclei. This induces on only faster relaxation, but also an evolution of the operators. To deepen this point, simulations including the field dependence and the J -couplings between all nuclei is necessary to understand this effect better.

We can say is that a term is not killed by a passage at low field. Another observation is that the relaxation at high field in the 500 MHz spectrometer is affected by the transfer (see table 11). Each term can have a different T_1 at the same magnetic field, and $T_1(I_z)$ is not necessary equal to $T_1(I_z S_z)$. This is what comforts us in the fact that the passage through low field acts like a filter that retains only specific terms.

	Peak (ppm)	T_1 with Tunnel (s)	T_1 with Anti-Tunnel (s)	Ratio $T_{1\text{ tunnel}}/T_{1\text{ anti-tunnel}}$
Chlorothiophene	7.40	7.3	10.0	1.4
	6.93	6.4	8.5	1.3
Bromothiophene	7.39	6.8	8.9	1.3
	6.99	5.7	8.1	1.4
Iodothiophene	7.36	4.7	5.6	1.2
	7.11	3.2	6.2	1.9

Table 11 T_1 relaxation times in bromothiophene, chlorothiophene and iodothiophene after D-DNP in a 500 MHz spectrometer.

We have demonstrated that the hyperpolarization of protons can be better preserved in dissolution-DNP by using magnetic tunnels. The benefits have been illustrated by several examples with improvement factors ranging between $1 < \epsilon_{\text{tunnel}} < 25$ for protons and carbon-13 nuclei. The enhancement factors depend on many parameters and vary greatly from one nucleus to another, from one molecule to another, and most probably from one laboratory to another. However, we have never witnessed any detrimental effects of our magnetic tunnels.

Chapter 5: Laser excitation for D-DNP

The use of stable radicals in DNP lead to severe constraints. DNP needs unpaired electronic spins in the sample. A challenging solution to overcome the presence of permanent radicals has been proposed by Wenkebach at PSI. They use a laser to excite a dye to promote an electron to a higher electronic state. If the Inter Crossing System (ICS) is efficient enough, and if the lifetime of the resulting triplet state enough long, DNP can be performed in such system.

Such experiments were successfully done at PSI [41] with a crystal of pentacene in naphtalene at 77 K in liquid nitrogen in a relatively low field 0.3 T. Pentacene is known to have a high ICS efficiency.

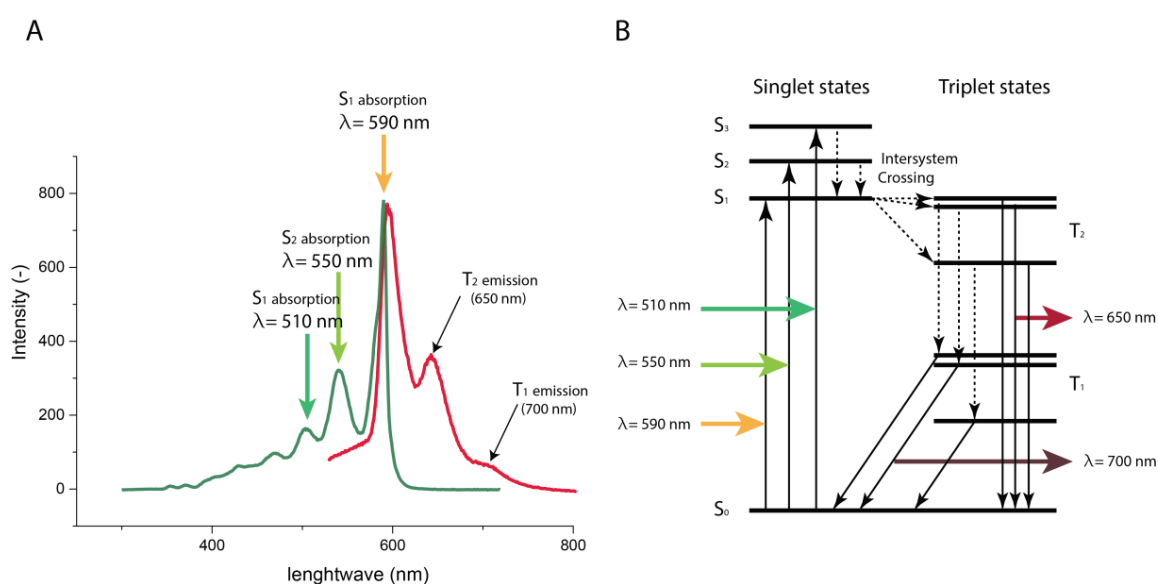


Fig. 53 A: UV-vis absorption and emission spectra of pentacene in paraterphenyl. B: Possible Jablonski diagram in agreement with the UV-vis spectrum.

At EPFL, we built a setup with a Jenoptik laser (wavelength of 1030 nm). With a lithium triborate (LiB₃O₅ or LBO) crystal, the frequency is doubled to a wavelength of 515 nm. LBO crystals are known to have nonlinear optical effects. This means that by interacting with the crystal lattice, at high power, two photons can be merged to create a new photon with twice the energy. The setup is composed of a laser at 1030 nm, a $\lambda/2$ plate, an LBO crystal in an oven to maintain it at a constant temperature, a mirror to reflect only the 515 nm beam, and a filter to stop the residual 1030 nm beam, an optical filter and a collimator.

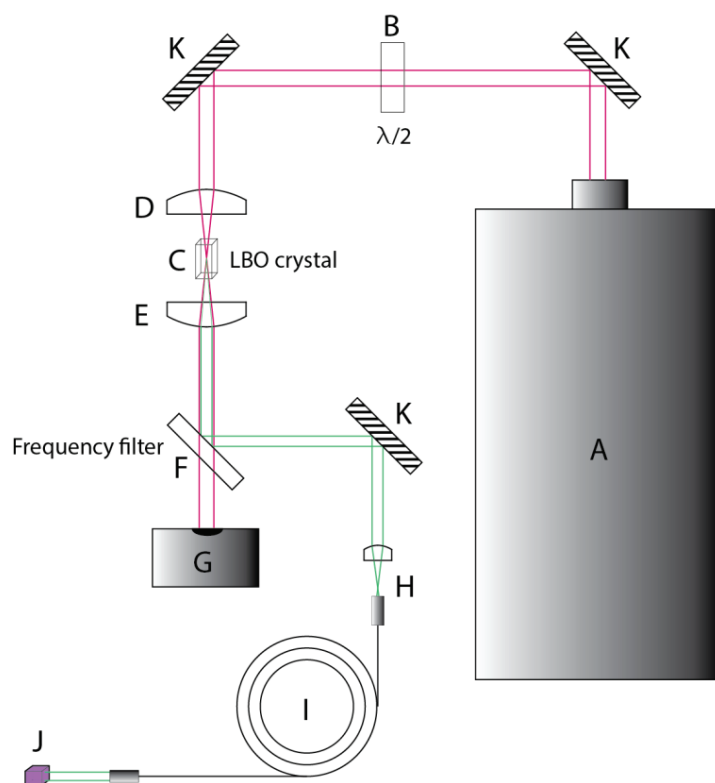


Fig. 54 Optical mounting to double the laser frequency. The laser has an initial wavelength of 1030 nm (A). The beam passes through a $\lambda/2$ lens (B), an LBO crystal mounted in an orientable structure (C). The LBO crystal is held in an oven to control its temperature. One lens focuses the beam in the LBO crystal (D). A second lens puts the beam in straight line (E). The frequency filter reflects only the 515 nm beam (F). The residual 1030 nm beam is lost in a waste box (G). The green beam reaches the optical fiber (H). The optical fiber (I) is long enough to reach the DNP polarizer. After passing through a collimator to readjust the beam, the sample (J) is irradiated. Three mirror (K) are used to finish the optical mounting.

The laser with the frequency doubling was successfully installed. The output power at 515 nm is measured for difference pulse lengths (200 nm to 600 nm) with a repetition frequency of 8 kHz. A power of 3 W is easily reached, which corresponds to the limit of our power meter. Figure 55 presents all possible power levels. Power above 3 W can be calculated by fitting for lower powers. A nonlinear fit is observed due to the nonlinear efficiency of the doubling process. The doubling process in LBO crystals is highly efficient at high power.

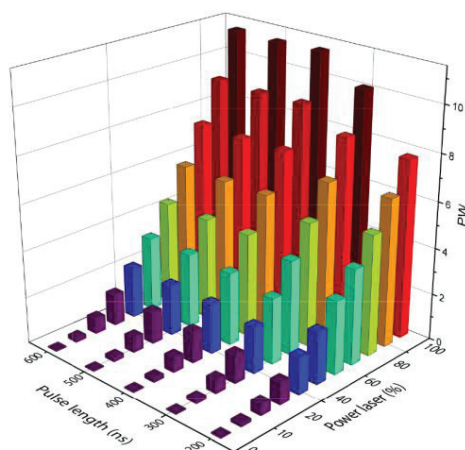


Fig. 55 This graph presents the measured power. Values higher than 3 W have been calculated by extrapolation because our power-meter is limited to a maximum power of 3 W.

DNP was not yet performed in our system. At present we are not able to tell if there is a technical reason for this failure, or if there is physical reason. Few papers [42, 43] give a dependence of the ISC rate on the magnetic field, but the difference is only a few percent, which is not sufficient to explain the failure of DNP in our system at high magnetic field (6.7 T). Low temperatures (4 K) can be discarded as a reason of failure because we ran tests at 77 K in liquid nitrogen. Note that the setup of our cryostat is absolutely adapted for liquid nitrogen.

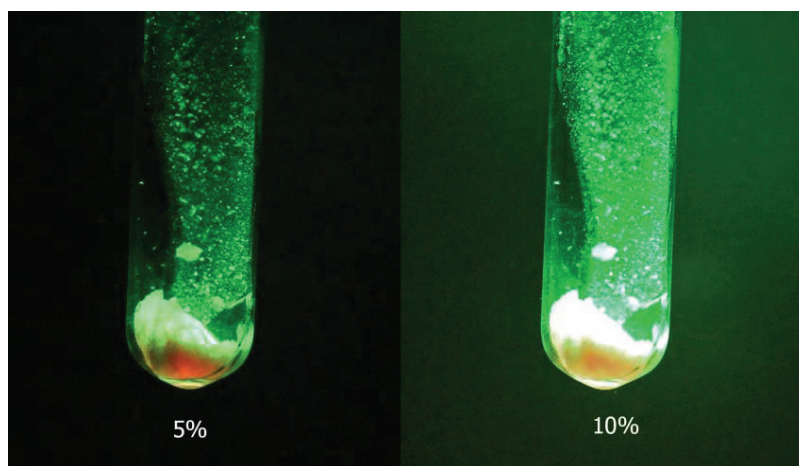


Fig. 56 A polycrystal of pentacene in para-terphenyl is irradiated with 5 or 10% of the power output, or 0.05 W and 0.18 W respectively. The red color (650 nm) confirms the presence of phosphorescence: according to the UV-vis emission spectra in figure 53, this color comes from the T_2 electronic level.

References

1. Bornet, A.; Melzi, R.; Linde, A.J.P.; Hautle, P.; van den Brandt, B.; Jannin, S.; Bodenhausen, G. *Journal of Physical Chemistry Letters*, **2013**, 4(1),111-114.
2. Comment, A.; van den Brandt, B.; Uffmann, K.; Kurdzesau, F.; Jannin, S.; Konter, J.A.; Hautle, P.; Wenckebach, W.T.H.; Gruetter, R.; van der Klink, J.J. *Concepts in Magnetic Resonance Part B-Magnetic Resonance Engineering*, **2007**, 31B(4),255-269.
3. Lindman, B.r.; Forsén, S., *Chlorine, bromine, and iodine NMR : physico-chemical and biological applications*. Nmr. 1976, Berlin ; New York: Springer-Verlag. xiii, 368 p.
4. Ginsberg, D.M.; Melchner, M.J. *Review of Scientific Instruments*, **1970**, 41(1),122.
5. Mieville, P.; Jannin, S.; Bodenhausen, G. *J. Magn. Reson.*, **2011**, 210(1),137-40.
6. Granwehr, J.; Leggett, J.; Kockenberger, W. *Journal of Magnetic Resonance*, **2007**, 187(2),266-276.
7. Batel, M.; Krajewski, M.; Weiss, K.; With, O.; Dapp, A.; Hunkeler, A.; Gimersky, M.; Pruessmann, K.P.; Boesiger, P.; Meier, B.H.; Kozerke, S.; Ernst, M. *Journal of Magnetic Resonance*, **2012**, 214,166-174.
8. Golman, K.; Zandt, R.I.; Lerche, M.; Pehrson, R.; Ardenkjaer-Larsen, J.H. *Cancer Res*, **2006**, 66(22),10855-60.
9. Sarkar, R.; Comment, A.; Vasos, P.R.; Jannin, S.; Gruetter, R.; Bodenhausen, G.; Hall, H.; Kirik, D.; Denisov, V.P. *Journal of the American Chemical Society*, **2009**, 131(44),16014.
10. Kuzma, N.N.; Hakansson, P.; Pourfathi, M.; Ghosh, R.K.; Kara, H.; Kadlecsek, S.J.; Pileio, G.; Levitt, M.H.; Rizi, R.R. *Journal of Magnetic Resonance*, **2013**, 234,90-94.
11. Nonaka, H.; Hata, R.; Doura, T.; Nishihara, T.; Kumagai, K.; Akakabe, M.; Tsuda, M.; Ichikawa, K.; Sando, S. *Nat Commun*, **2013**, 4,2411.
12. Cudalbu, C.; Comment, A.; Kurdzesau, F.; van Heeswijk, R.B.; Uffmann, K.; Jannin, S.; Denisov, V.; Kirik, D.; Gruetter, R. *Phys Chem Chem Phys*, **2010**, 12(22),5818-23.
13. Bornet, A.; Jannin, S.; Bodenhausen, G. *Chemical Physics Letters*, **2011**, 512(4-6),151-154.
14. Bornet, A.; Melzi, R.; Jannin, S.; Bodenhausen, G. *Applied Magnetic Resonance*, **2012**, 43(1-2),107-117.
15. Jannin, S.; Bornet, A.; Melzi, R.; Bodenhausen, G. *Chemical Physics Letters*, **2012**, 549,99-102.
16. Metz, G.; Wu, X.L.; Smith, S.O. *Journal of Magnetic Resonance Series A*, **1994**, 110(2),219-227.
17. Hartmann, S.R.; Hahn, E.L. *Physical Review*, **1962**, 128(5),2042.
18. Hediger, S.; Meier, B.H.; Kurur, N.D.; Bodenhausen, G.; Ernst, R.R. *Chemical Physics Letters*, **1994**, 223(4),283-288.
19. Aptekar, J.W.; Cassidy, M.C.; Johnson, A.C.; Barton, R.A.; Lee, M.; Ogier, A.C.; Vo, C.; Anahtar, M.N.; Ren, Y.; Bhatia, S.N.; Ramanathan, C.; Cory, D.G.; Hill, A.L.; Mair, R.W.; Rosen, M.S.; Walsworth, R.L.; Marcus, C.M. *Acs Nano*, **2009**, 3(12),4003-4008.
20. Dementyev, A.E.; Cory, D.G.; Ramanathan, C. *Physical Review Letters*, **2008**, 100(12).
21. Cassidy, M.C.; Chan, H.R.; Ross, B.D.; Bhattacharya, P.K.; Marcus, C.M. *Nature Nanotechnology*, **2013**, 8(5),363-368.
22. Milani, J.; Vuichoud, B.; Bornet, A.; Mieville, P.; Mottier, R.; Jannin, S.; Bodenhausen, G. *Review of Scientific Instruments*, **2015**, 86(2).
23. Comment, A.; van den Brandt, B.; Uffmann, K.; Kurdzesau, F.; Jannin, S.; Konter, J.A.; Hautle, P.; Wenckebach, W.T.H.; Gruetter, R.; van der Klink, J.J. *Concepts Magn. Reson. B*, **2007**, 31B(4),255-269.
24. Comment, A.; van den Brandt, B.; Uffmann, K.; Kurdzesau, F.; Jannin, S.; Konter, J.A.; Hautle, P.; Wenckebach, W.T.; Gruetter, R.; van der Klink, J.J. *Appl. Magn. Reson.*, **2008**, 34(3-4),313-319.

25. Jannin, S.; Comment, A.; Kurdzesau, F.; Konter, J.A.; Hautle, P.; van den Brandt, B.; van der Klink, J.J. *J. Chem. Phys.*, **2008**, 128(24),241102.
26. Jannin, S.; Bornet, A.; Melzi, R.; Bodenhausen, G. *Chem. Phys. Lett.*, **2012**, 549,99-102.
27. Bowen, S.; Hilty, C. *Physical Chemistry Chemical Physics*, **2010**, 12(22),5766-5770.
28. Kowalewski, J.z.; Mäler, L., *Nuclear spin relaxation in liquids : theory, experiments, and applications*. Series in chemical physics. 2006, New York: Taylor & Francis. 426 p.
29. Borah, B.; Bryant, R.G. *Journal of Chemical Physics*, **1981**, 75(7),3297-3300.
30. Chiavazza, E.; Kubala, E.; Gringeri, C.V.; Duwel, S.; Durst, M.; Schulte, R.F.; Menzel, M.I. *J. Magn. Reson.*, **2013**, 227,35-8.
31. Korchak, S.E.; Ivanov, K.L.; Pravdivtsev, A.N.; Yurkovskaya, A.V.; Kaptein, R.; Vieth, H.M. *Journal of Chemical Physics*, **2012**, 137(9).
32. Leggett, J.; Hunter, R.; Granwehr, J.; Panek, R.; Perez-Linde, A.J.; Horsewill, A.J.; McMaster, J.; Smith, G.; Kockenberger, W. *PCCP*, **2010**, 12(22),5883-92.
33. Bowen, S.; Hilty, C. *PCCP*, **2010**, 12(22),5766-70.
34. Nelson, S.J.; Vigneron, D.; Kurhanewicz, J.; Chen, A.; Bok, R.; Hurd, R. *Appl. Magn. Reson.*, **2008**, 34(3-4),533-544.
35. Reese, M.; Lennartz, D.; Marquardsen, T.; Hofer, P.; Tavernier, A.; Carl, P.; Schippmann, T.; Bennati, M.; Carlomagno, T.; Engelke, F.; Griesinger, C. *Appl. Magn. Reson.*, **2008**, 34(3-4),301-311.
36. Mieville, P.; Ahuja, P.; Sarkar, R.; Jannin, S.; Vasos, P.R.; Gerber-Lemaire, S.; Mishkovsky, M.; Comment, A.; Gruetter, R.; Ouari, O.; Tordo, P.; Bodenhausen, G. *Angew. Chem. Int. Edit.*, **2010**, 49(35),6182-6185.
37. Halbach, K. *Nucl. Instrum. Methods*, **1980**, 169(1),1-10.
38. Melton, B.F.; Pollak, V.L.; Mayes, T.W.; Willis, B.L. *J. Magn. Reson. A*, **1995**, 117(2),164-170.
39. Gajan, D.; Bornet, A.; Vuichoud, B.; Milani, J.; Melzi, R.; van Kalkeren, H.A.; Veyre, L.; Thieuleux, C.; Conley, M.P.; Gruning, W.R.; Schwarzwald, M.; Lesage, A.; Coperet, C.; Bodenhausen, G.; Emsley, L.; Jannin, S. *Proc. Natl. Acad. Sci. USA*, **2014**, 111(41),14693-14697.
40. Tayler, M.C.D.; Marco-Rius, I.; Kettunen, M.I.; Brindle, K.M.; Levitt, M.H.; Pileio, G. *Journal of the American Chemical Society*, **2012**, 134(18),7668-7671.
41. Eichhorn, T.R.; Haag, M.; van den Brandt, B.; Hautle, P.; Wenckebach, W.T.; Jannin, S.; van der Klink, J.J.; Comment, A. *Journal of Magnetic Resonance*, **2013**, 234,58-66.
42. Corval, A.; Kryschi, C.; Astilean, S.; Trommsdorff, H.P. *Journal of Physical Chemistry*, **1994**, 98(30),7376-7381.
43. Astilean, S.; Chitta, V.; Corval, A.; Miller, R.J.D.; Trommsdorff, H.P. *Chemical Physics Letters*, **1994**, 219(1-2),95-100.

Part C:

Applications

In this chapter, different applications of D-DNP that benefit from the hardware developments described in the previous part are described. It will be shown how the magnetic tunnel and the CP circuits in the polarizer developed in this thesis can overcome some limits of the standard D-DNP method. This will allow us to see applications of these pieces of hardware in some concrete practical experiments. D-DNP was originally developed and is most widely used for medical imaging [1], where the rates of metabolization of hyperpolarized substrates such as pyruvate can be monitored in different locations. Such metabolic processes can be reporters for potential cancerous degeneration of the observed tissues. Even if it is not developed in our laboratory, hyperpolarized medical imaging should surely benefit from the CP enhanced build-up of the ^{13}C polarization, especially from faster build-ups and higher SNR. Preserving fast relaxing water, using the magnetic tunnel, could also be of interest for DNP enhanced angiographic studies [2].

D-DNP could potentially be of interest for applications to drug screening studies in the pharmaceutical domain [3, 4]. In order to ensure the generality of screening methods of ligand-protein interactions, isotope labelling should be avoided. Therefore, hyperpolarized protons of potential ligands appear to be a better target for drug screening than hyperpolarized ^{13}C or ^{15}N . In this context, the magnetic tunnel developed in *Chapter 4, Part B* permits one to overcome the relaxation of hyperpolarized ^1H at low field during the transfer, resulting in significant SNR gain in ligand screening studies. An alternative ensuring an even better generality is to use water as a source of hyperpolarization. Hyperpolarized ligand screening can then be performed with the so-called Water-LOGSY technique [5]. The polarization of water molecules is a challenge. Its observation after dissolution is almost impossible without a magnetic tunnel. Moreover, it appears to be attractive to be able to obtain pure hyperpolarized water. Different strategies to do so will be presented in the next chapter.

In a second part, benefits of the use of Cross Polarization to enhance the hyperpolarization of low gamma nuclei are presented with a few examples. An enzymatic study of the phosphorylation of glucose monitored by CP-DNP enhanced ^{13}C spectroscopy will be first presented. In a second example, non-labeled samples used for metabolomic studies (tomato extracts and cancer cell extracts) are hyperpolarized with CP from ^1H to ^{13}C . Information that is not accessible without DNP, such as ^{13}C spectra of slowly relaxing carboxyl groups of metabolites, or single scan 2D HMBC, can be obtained in a short experimental time using Cross-Polarization DNP.

Finally, in the last part, unusual coupling patterns in ^{13}C spectra that are visible at high polarization are shown. The study of such patterns allows rapidly determining the ^{13}C polarization.

Chapter 1: ^1H DNP with a magnetic tunnel

Hyperpolarized protons are useful in different domains. Drug screening, which is one of them, will be highlighted. One of the big drawbacks of hyperpolarized protons is their fast relaxation and their strong dependence on the magnetic field. The magnetic tunnel presented before appears as a great advantage for this kind of study.

a. Drug Screening by hyperpolarized ligands

In the pharmaceutical domain, the drug discovery process goes through several steps. The first step is the identification of potential molecules. The technique consists in recognizing ligands or fragments in extensive libraries of chemical compounds. Several methods like enzyme-linked immunosorbent assays (ELISA) [6], surface plasmon resonance [7] (SPR, also known under the trade name Biacore), isothermal titration calorimetry (ITC) [8], fluorescence anisotropy [9], and an ever-expanding range of nuclear magnetic resonance (NMR) techniques are applied in pharmaceutical industry [10].

In NMR, one strategy consists in measuring the perturbation of different NMR parameters of the free ligands in fast exchange (such as T_1 , $T_{1\rho}$, T_2 or the chemical shifts) by the small fraction of ligands that are bound to the protein [11]. The deviation of these parameters from those of the free ligand depends on the concentrations of both protein and ligand, and also on the dissociation constant K_D . Therefore, it is possible to measure the strength of the binding by recording the deviation of a chosen NMR parameter while titrating either the ligand or the protein.

The choice of the observed NMR parameter is important. For a fixed protein-ligand ratio, a large difference between the free and bound parameters will induce a more pronounced contrast. It was shown by Roberto Buratto et al. [12, 13] that the use of the relaxation time constant of so-called Long-Lived States (T_{LLS}) [14] as observable allows one to obtain such high contrast in protein-ligand studies. Using T_{LLS} as a reporter of ligand binding made it possible to decrease both ligand and protein concentration while keeping the same precision. More details of the experiment can be found in the PhD thesis of Dr. Roberto Buratto.

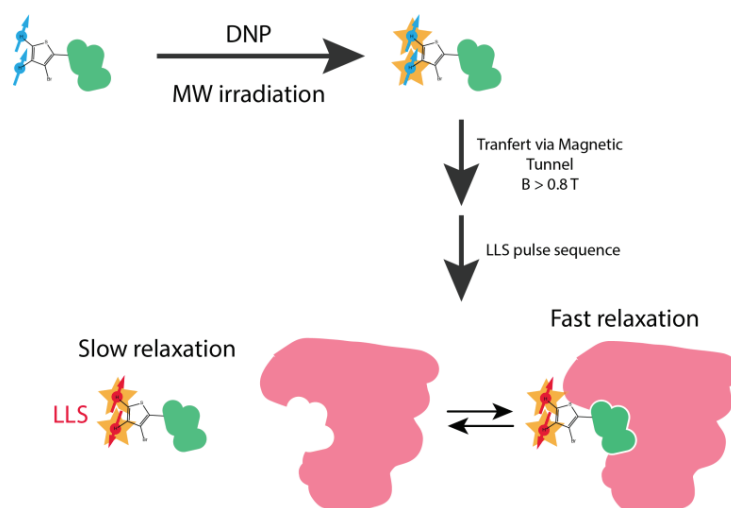


Fig. 1 The protons of the bromothiophene derivative of the tri-peptide Glycine-Glycine-Arginine (BT-GGR) are hyperpolarized using a standard D-DNP protocol. The two protons in the thiophene group are detected. The magnetic tunnel is important to preserve the magnetization during the transfer. The ligand mixture is then injected into the protein solution. The LLS pulse sequence is applied to optimize the contrast between the “fast” and “slow” relaxation regimes.

To make the method general, so-called spin-pair labels, i.e., fragments of molecules containing a pair of ^1H capable of carrying LLS such as bromothiophene, can be covalently bound to the ligands. Such ligands with covalently attached spin-pair labels contain isolated spins with long T_1 values and are therefore suitable for hyperpolarization by dissolution DNP. Provided $T_1(^1\text{H}) > 1$ s, a sufficient fraction of the hyperpolarized magnetization can be preserved during transfer from the DNP polarizer to the NMR spectrometer. In this context, the use of a magnetic tunnel ($B > 0.8$ T) has proven to be crucial for the experiment. Bromothiophene linked to a weak ligand of the protein trypsin, the tri-peptide Glycine-Glycine-Arginine (BT-GGR) was used as a test of DNP-enhanced LLS screening [15]. Thanks to the passage through the magnetic tunnel during the transfer, the DNP enhancements of the aromatic protons of the spin-pair-labeled spy ligand BT-GGR were on the order of $\epsilon_{\text{DNP}} = 100\text{--}200$, relative to their Boltzmann equilibrium at 25 °C and 11.7 T (500 MHz for protons). A significant fraction of the proton hyperpolarization was lost during the 10 s interval between dissolution and signal acquisition, but the SNR was sufficient to observe the ligand at a concentration between 10 μM (SNR = 16) and 100 μM (SNR = 130). Without voyage through the tunnel, it was not possible to observe any enhanced proton signals. Once in the spectrometer, the hyperpolarized magnetization is converted into Long-Lived States using a dedicated pulse sequence [16]. The signal remaining after a fixed relaxation delay is a direct reporter of the ligand affinity. In a more general version of the experiment, a weak hyperpolarized ligand can be used as a probe, reporting for the presence of stronger competitors added at low concentration to the system.

Figure 2 shows DNP-enhanced LLS spectra of 120 μM of the spin-pair-labeled spy ligand BT-GGR in the absence of protein (black line), the same upon addition of 1.4 μM trypsin (red), and the same with

further addition of 1.4 μM myricetin as competitor [17] (green). A dramatic decrease of the LLS signal intensity stemming from BT-GGR is observed upon adding trypsin. As the hyperpolarized ligand binds to the protein, its LLS lifetime is shortened by fast relaxation in the PL complex, leading to a weaker signal after the fixed LLS sustaining delay. Addition of an equimolar amount of the competitor myricetin [17] leads to a partial displacement of the spy ligand that can be readily detected by the revival of its LLS signal. With only 120 μM of the spin-pair-labeled spy ligand BT-GGR, the DNP-enhanced LLS spectrum of figure 2 recorded in a single scan after a LLS sustaining delay of 3 s has a signal-to-noise ratio (SNR) of 130. Under the same conditions, but without DNP, an accumulation of 225 transients for ~ 1 h was necessary to reach the same SNR. A DNP-enhanced LLS spectrum of BT-GGR with a concentration as low as 10 μM could be recorded with an SNR of 16.

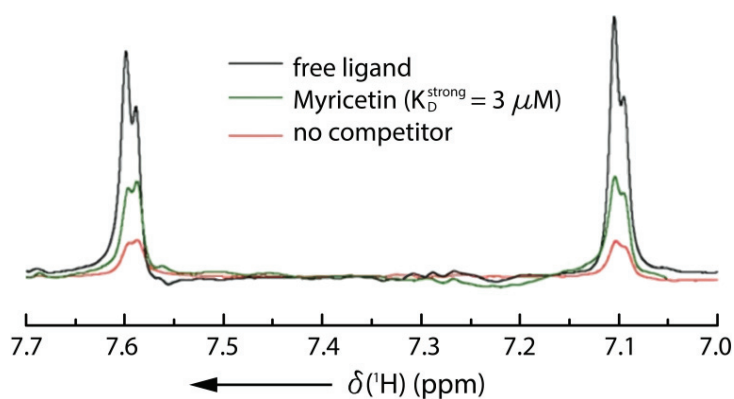


Fig. 2 DNP-enhanced LLS competition binding experiments. DNP-enhanced LLS spectra of the two aromatic protons of bromothiophene in BT-GGR 120 μM after 3 s, without protein (black), in the presence of 1.4 μM trypsin (red), and with 1.4 μM trypsin and 1.4 μM myricetin as competitor (green). All spectra were acquired in a single scan in D_2O , at 25 $^\circ\text{C}$ and 11.7 T (500 MHz for protons).

A dedicated LLS-DNP screening apparatus could be made commercially available in the near future. This approach allows one to decrease the concentrations of spy ligands, competitors and target proteins.

b. Hyperpolarized water without contaminants

The use of a magnetic tunnel between the polarizer and the detection spectrometer allows one to access hyperpolarized protons in solution. A molecule of particular interest, which is also particularly challenging, is the simple H₂O molecule. Hyperpolarized water can be used for angiography [2]. Another promising research field consists in the transfer of the polarization stored in water to proteins in order to acquire hyperpolarized ¹H - ¹³C or ¹H - ¹⁵N spectra with SOFAST [18] methods of acquisition [19]. Finally, water magnetization is intensively used in pharmaceutical industry for ligand screening, using the so-called Water-LOGSY technique [5]. The hyperpolarized version of this experiment will be developed in the next chapter. A common need of these three experiments is to be able to get pure hyperpolarized water, free of any contaminants. This will prevent fast paramagnetic relaxation of hyperpolarized water during acquisition. It will also avoid paramagnetic species and glassing agent from interacting with the protein in solution. To reach this aim, two methods based on filterable materials were developed.

A first class of materials that were developed for this purpose are called Hybrid Polarizing Solids (HYPSOs) and are composed of porous silicate polymers with radicals as polarizing agents covalently attached to the walls of the pores [20]. Because they are also used for CP DNP experiments, HYPSOs are treated in *Chapter 2.a, Part C*.

A second way of obtaining pure hyperpolarized solutions that was developed in our laboratory consists in using a thermo-sensitive polymer [21] that becomes insoluble at higher temperatures in the dissolution process. This material, composed of poly(N-isopropylacrylamide), also known as pNiPAM-COOH, is covalently linked to nitroxide radicals. The details of the synthesis and the operation with this polymer for DNP applications will be presented in detail in Basile Vuichoud's thesis. Using filterable spin-labeled thermos-sensitive polymers as polarizing agents to polarize H₂O, and transferring the sample through a magnetic tunnel, it was possible to obtain a proton polarization estimated to be $P(^1\text{H}) \approx 5\%$ after dissolution. The absence of paramagnetic species is confirmed by the long relaxation time of the hyperpolarized HDO, $T_1(\text{HDO}) = 36.6$ s, as shown in figure 3b.

On figure 3a, one can see a huge broadening of the HDO peak at high polarization (with a FWHM = 1500 Hz). This broadening is reduced as the hyperpolarization relaxes toward Boltzmann equilibrium. This broadening is arises from a phenomenon called Radiation Damping (RD) [22]. The phenomenon is caused by the interaction between the RF coil and the bulk magnetization of the sample. RD is normally observed in experiments with high proton concentration, as for protein NMR. It also occurs here in the case of hyperpolarized water, as the number of spins is relatively high compared to standard DNP

samples, with a 2.2 M concentration of HDO, but mainly because the protons spins are hyperpolarized, resulting in a large bulk magnetization. After RF excitation, the precessing magnetization is so intense that it generates an oscillating current in the receiver coil, which itself induces a resonant magnetic field. This acts as a selective pulse on HDO and broadens the water peak. RD induced by magnetization excited by a small flip angle pulse does not have the same effect on water if it is positively or negatively polarized by DNP. If the ^1H are polarized positively, RD will merely relax the small transverse magnetization toward the hyperpolarized state, shortening the FID, and broadening its resulting Fourier transformed peak. In the case of negative polarization on the other hand, RD will cause a complete relaxation of the hyperpolarized bulk magnetization that is antiparallel with respect to B_0 toward its equilibrium orientation along the quantization axis. For this reason, a positive polarization is mandatory for water experiments.

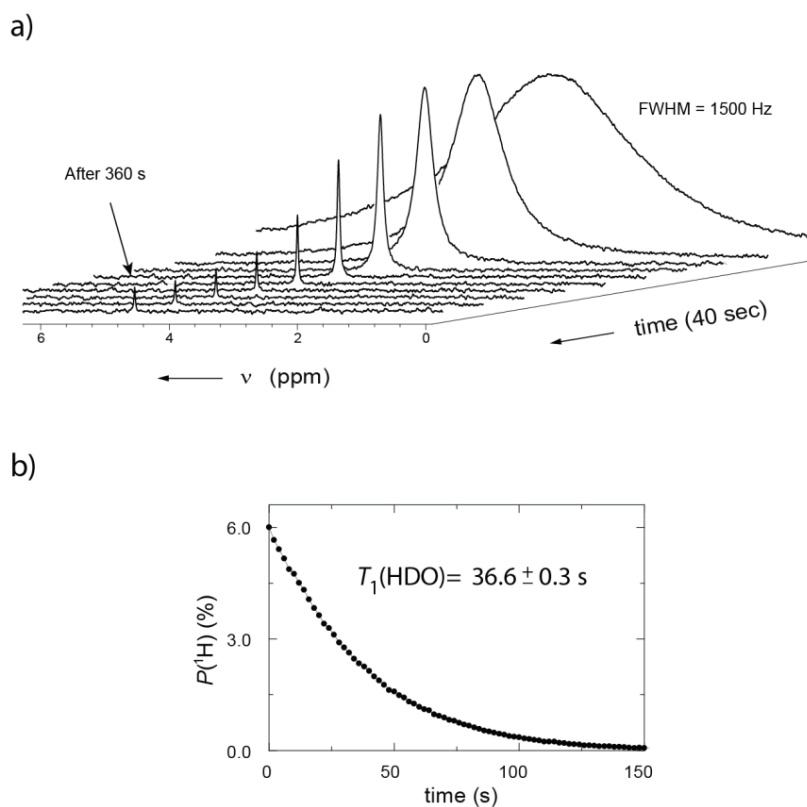


Fig. 3 a) Hyperpolarized magnetization of water leads to an intense signal with a Full Width at Half Maximum (FWHM) that is very broad. The magnetization is so intense that induces a current in the coil. A positive signal, where the water magnetization is parallel to the B_0 field, acts as a selective pulse that drives the return of the magnetization to the quantization axis. b) The signal of HDO (resulting from H_2O diluted in D_2O) decays with $T_1 = 37$ s in 11.7 T. This is possible only in the absence of paramagnetic impurities.

It appears that the magnetic tunnel is especially efficient to maintain the polarization of water during transfer even if the radicals are completely filtered. Due to the dilution by D_2O used as dissolution solvent, the form of hyperpolarized water molecule is mostly HDO. As explained in *Chapter 4, Part B*,

the scalar coupling with the quadrupolar deuterium nucleus could have a huge relaxing effect at low magnetic fields, thus explaining the advantage of the tunnel, even if the hyperpolarized solution is free of paramagnetic species.

c. Water-LOGSY

We saw in *Section a* the possibility of hyperpolarizing ligands for drug screening. Here, an alternative DNP-enhanced drug screening method is presented. It is based on Water-LOGSY (water-ligand observed via gradient spectroscopy) [5]. The protocol of the method can be made more repeatable, since only water is hyperpolarized, the ligand and the protein being dissolved at low concentration in the NMR tube waiting in the detection spectrometer.

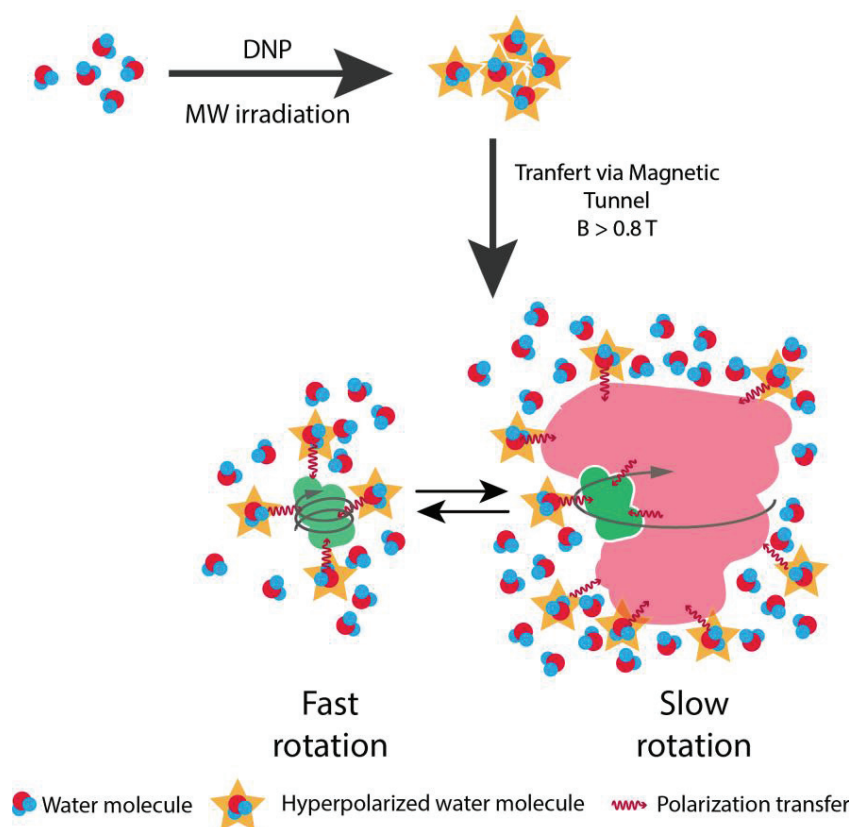


Fig. 4 Hyperpolarized water is prepared by a standard D-DNP protocol. The water molecule is represented by a red circle with two blue circles. A star represents the enhanced polarization. The DNP sample is then injected into a solution containing both the protein and the ligand. By NOE exchange, the hyperpolarized water distributes its polarization to the ligand and protein. The protein signal will have a signal with an opposite sign with respect to the ligand signal because of its different of motional regime.

The detection of ligand binding by Water-LOGSY relies on the spontaneous transfer of polarization from hyperpolarized water to ligands via either of two pathways, either via the nuclear Overhauser effect (NOE) or via exchange of labile protons, though signals due to exchange are generally not

considered as reliable reporters of binding. The transfer can either occur directly from the solvent to the fast tumbling free ligand, or indirectly, relayed via a slow tumbling protein to bound ligands (figure 4). The sign of the NOE transfer depends on the rotational correlation time. Inspecting the energy level diagram of two coupled spins I and S in figure 5a, which is contrary to NOE experiments described in many standard textbooks [23], the intensity of the spin I (the potential ligand) is not affected by NOE after saturation of spin S , but by the hyperpolarized proton spin S of water. This implies that in the case of Water-LOGSY, the signal of the ligand is increased if the W_0 relaxation pathway is dominant, and negative if the W_2 pathway dominates. Using a spectral density as a function of the rotational correlation time τ_c , one can plot the dependence of the W_2 and W_0 rates on the motion of the molecule, as shown in figure 5b. It follows that rapidly tumbling free ligands acquire negative enhancements, while slowly tumbling ligand–protein complexes feature positive enhancements (figure 5c). Therefore, the difference between free and bound ligands can be readily identified.

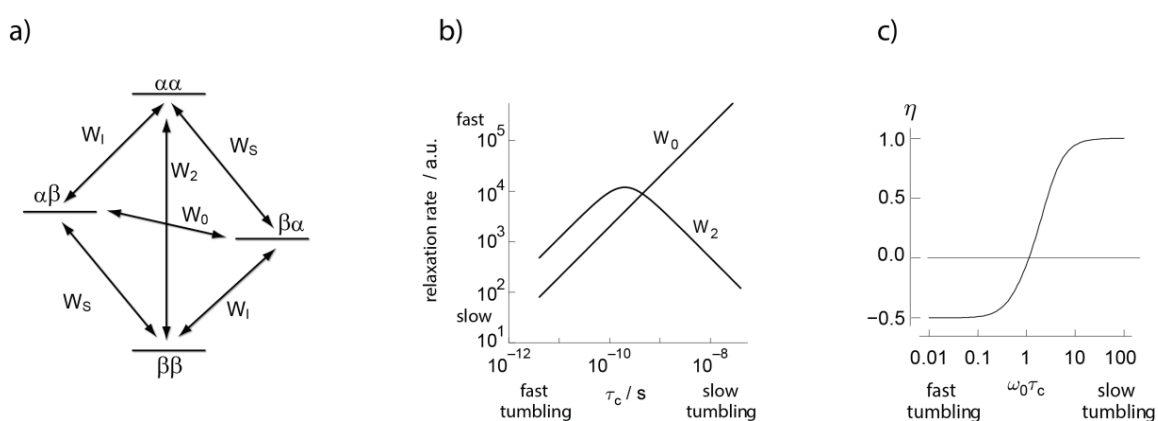


Fig. 5 a) A two spin system is composed by four energy levels. The Overhauser effect describes the transfer of populations through the rates W_0 and W_2 . b) Dependence of the rates W_0 and W_2 on the rotational correlation time. The rate W_0 gives a positive enhancement of the I signal, while the rate via W_2 gives negative enhancement of I signal. c) Water-LOGSY effect as function of the tumbling of the molecule. Picture adapted from *Nuclear Magnetic Resonance* by P.J. Hore.

NMR signals observed in conventional Water-LOGSY experiments (without DNP) are typically 20–30 times weaker than signals in traditional one-dimensional NMR experiments, because only magnetization transferred by NOE and/or exchange from water is selectively detected. This method therefore suffers from low sensitivity, and from false positives caused by aggregated or denatured proteins. By applying D-DNP, this method can be greatly boosted by injecting hyperpolarized water into solutions of proteins and ligands. Ligand binding can be detected in a few seconds, whereas about 30 min is usually required without hyperpolarization. Hyperpolarized water also enhances proton signals of proteins at concentrations below 20 μM so that one can verify in a few seconds whether the proteins remain intact or have been denatured [24].

As explained in part *b*, the excitation of hyperpolarized water can lead to massive radiation damping (RD) and demagnetizing effects of distant dipolar fields (DDF). Therefore, frequency-selective pulses are used in order to preserve the water resonance while detecting ligand and protein signals with full sensitivity.

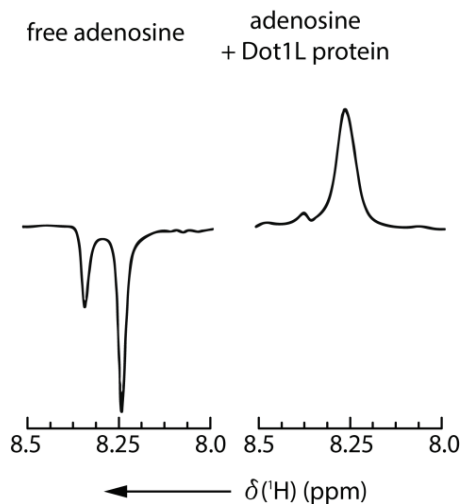


Fig. 6 Water-LOGSY signals of the two aromatic protons of adenosine, which binds weakly to the protein Dot1L. The spectrum of free adenosine is in antiphase in contrast to the in-phase spectrum of the adenosine bound to Dot1L.

Chapter 2: Cross Polarization (CP)

a. Hyperpolarized Glucose

NMR is commonly used to study kinetics of chemical reactions. In many applications, the signal has to be strong enough to be detected in a single scan. Once again, DNP appears to have a great advantage. D-DNP experiments enabled us to study the kinetics of the enzymatic phosphorylation reaction of glucose to form glucose-6-phosphate (G6P) by hexokinase (HK), with or without the presence of an excess of G6P, which is known to be an inhibitor of the enzyme.

Glucose is a substrate of paramount importance for living cells and organisms. It is involved in glycolysis and serves as the precursor of the Pentose Phosphate Pathway (PPP). The metabolism of glucose can be altered under various pathological circumstances. Hyperpolarization by dissolution-DNP may provide a way to witness such alterations, as was recently shown for cancer cell cultures [25]. In this context, kinetic studies of individual enzymes contributing to the metabolism of glucose are obviously of crucial interest for detailed investigations of metabolic chains.

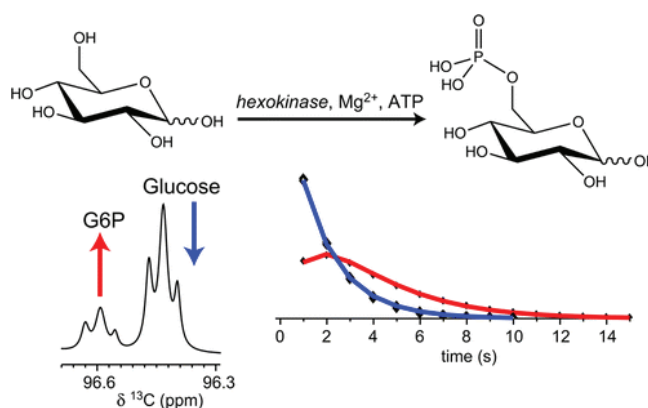


Fig. 6 The production of G6P catalyzed by hexokinase is studied by D-DNP. The signal decay is a function of T_1 relaxation and $pf k$, the characteristic reaction constant. The blue curve shows the glucose signal and the red curve the creation of G6P. Both curves tend to zero due to the loss of hyperpolarization.

The main goal of this work [26] is to characterize the phosphorylation kinetics of glucose by hexokinase (HK) on a time scale that is sufficiently short, on the order of 20 s, so that one can neglect the interconversion of the α and β anomers of both glucose and glucose-6-phosphate (G6P). The phosphorylation of glucose represents the initial enzymatic transformation that is common to both glycolysis and PPP. This reaction consumes one molecule of adenosine triphosphate (ATP) and requires the presence of magnesium ions Mg^{2+} (figure 7).

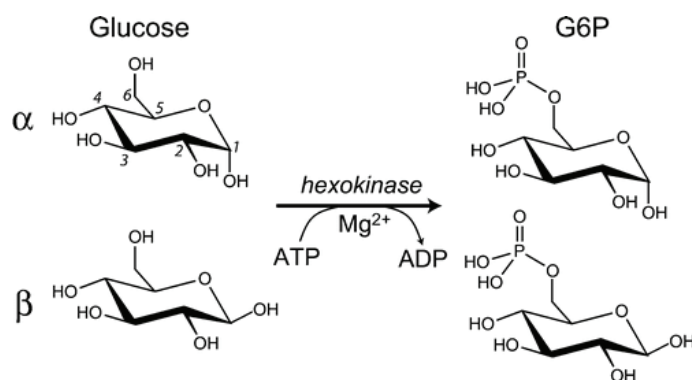


Fig. 7 Phosphorylation of the α and β anomers of glucose by hexokinase. Both α and β anomers, and the numbering of the carbon atoms, are indicated.

A solution containing 7.5 M [$^{13}\text{C}_6\text{-d}_7$] D-glucose was dissolved in 20% H_2O and 80% D_2O with 50 mM TEMPOL. The sample was then polarized by DNP using CP from ^1H to ^{13}C . After dissolution, the phosphorylation of the two anomers by hexokinase was followed by ^{13}C NMR using pulses with small angles. We determined the rate constants of this reaction by fitting the build-up and decay of the signals. Our analysis of the experiments assumes a pseudo-first order reaction (equations 3.1 and 3.2), justified by the presence of a large excess of ATP, and takes into account the known inhibition of hexokinase by G6P.

$$\frac{d[G]}{dt} = -k[G] \quad (3.1)$$

$$\frac{d[G6P]}{dt} = -\frac{d[G]}{dt} \quad (3.2)$$

The kinetic rate constants of the reactions can be determined thanks to a dramatic sensitivity enhancement of uniformly ^{13}C - and ^2H -labeled glucose afforded by D-DNP. The catalytic rate constants k and the dissociation constants K_D of the HK-G6P complex are determined to characterize the kinetic reaction.

anomer	α	β
K_D (mM)	35.0	22.5
k ($\text{s}^{-1}\text{M}^{-1}$)	11613	18453

b. Hybrid polarizing solids (HYPSOs) for pure hyperpolarized liquids

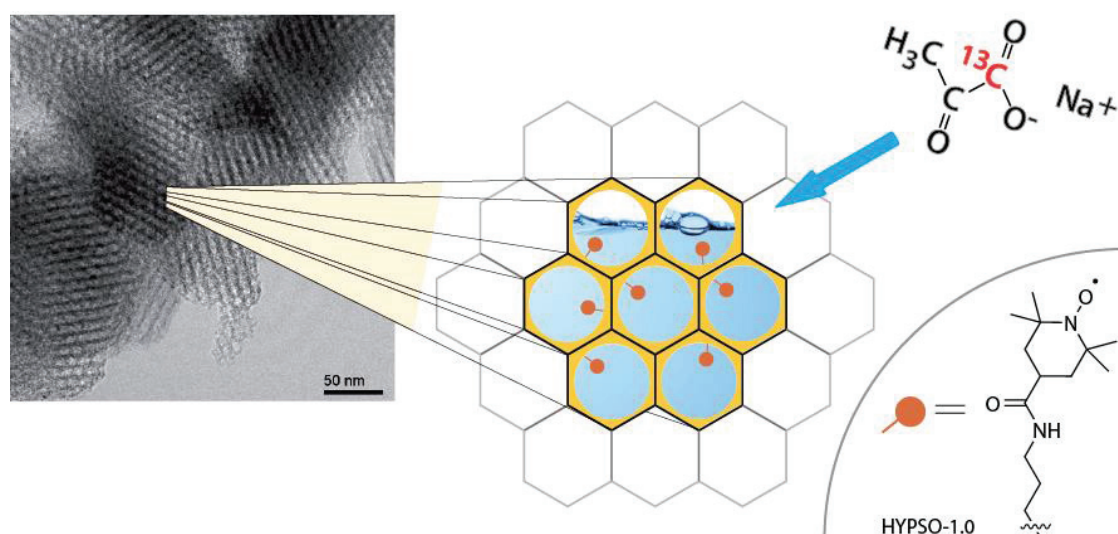


Fig. 8 HYPSO materials are composed of porous silica materials. The TEMPO radicals are attached by covalent bonds inside the pores. Molecules of interest like acetate can be loaded in the pores.

As discussed before, the presence of PAs and/or glassing agents in the sample after dissolution can raise concerns for *in vivo* MRI applications, since they may perturb molecular interactions, and may induce the erosion of hyperpolarization in spectroscopy and MRI. To answer these concerns, filterable hyperpolarizing media with immobilized radicals were developed in collaboration with Dr. Chloé Thieuleux (C2P2, Lyon), Prof Lyndon Emsley (at that time at ENS, Lyon) and Prof. Christoph Copéret (ETHZ) [20]. D-DNP can be performed efficiently with hybrid polarizing solids (HYPSOs) with 2,2,6,6-tetramethyl-piperidine-1-oxyl radicals incorporated in a mesostructured silica material and homogeneously distributed in its pore channels (figure 8). The powder can be wetted with a solution containing molecules of interest (for example, metabolites for MRS or MRI) to fill the pore channels (“incipient wetness impregnation”), and DNP can be performed at low temperatures in a very efficient manner. Using a first generation of HYPSOs, $P(^1\text{H}) = 49\%$ could be reached with a build-up time constant $\tau_{\text{DNP}}(^1\text{H}) = 129 \text{ s}$ and $P(^{13}\text{C}) = 33\%$ could be obtained using $1\text{H} - ^{13}\text{C}$ CP. This approach allows one to obtain a high polarization without the need for glass-forming agents and is applicable to a broad range of substrates, including peptides and metabolites. During dissolution, HYPSO is physically retained by simple filtration in the cryostat of the DNP polarizer, and a pure hyperpolarized solution is collected within a few seconds. The resulting solution contains the pure substrate, is free from any paramagnetic or other pollutants, and is ready for *in vivo* infusion.

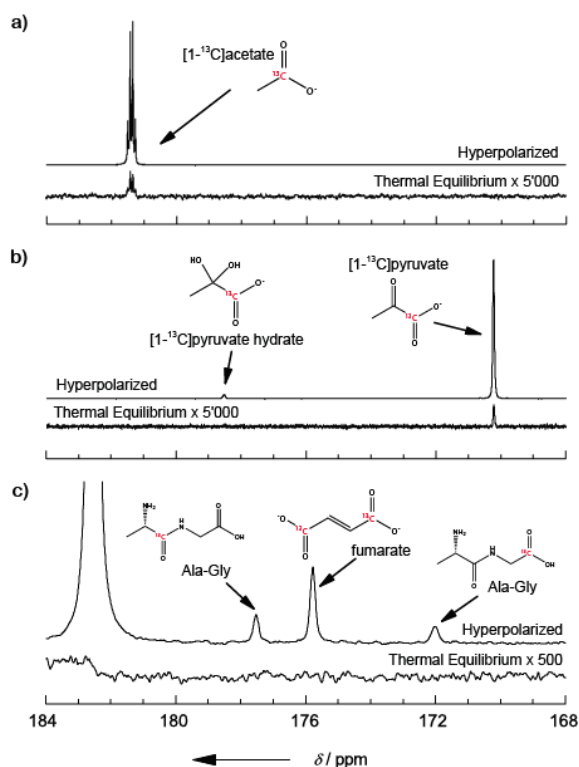


Fig. 9 Results of D-DNP performed with HYPSON with a) $[1-^{13}\text{C}]$ -acetate, b) $[1-^{13}\text{C}]$ -pyruvate and c) natural abundance fumarate and the dipeptide Alanine-Glycine (Ala-Gly)

Using HYPSON polarizing matrices, it was possible to hyperpolarize small metabolites, such as $[1-^{13}\text{C}]$ -pyruvate, to achieve $P(^{13}\text{C}) = 25.3\%$, i.e., an enhancement factor $\epsilon_{\text{DNP}} = 32500$ compared to its thermal equilibrium signal after complete relaxation. For $[1-^{13}\text{C}]$ -acetate, we obtained $P(^{13}\text{C}) = 16.5\%$ and for both carbonyl carbons in natural abundance fumarate, we observed $P(^{13}\text{C}) = 19.9\%$. For the dipeptide Alanine-Glycine we obtained $P(^{13}\text{C}) = 15.0\%$ for the alanine carbonyl carbon and $P(^{13}\text{C}) = 13.6\%$ for the glycine carboxyl carbon. (Figure 9). Hyperpolarization was performed as described in *Chapter 2, Part B* by $^1\text{H} \rightarrow ^{13}\text{C}$ CP-DNP using HYPSON 1.0, followed by dissolution. The hyperpolarized signals were acquired with 5° nutation angle pulses, whereas the thermal equilibrium signals, scaled by a factor of 5 000, were measured with 27, 128, and 512 scans for $[1-^{13}\text{C}]$ -acetate, $[1-^{13}\text{C}]$ -pyruvate, and L-alanine-glycine and fumarate, respectively, using 90° nutation angle pulses applied every 300 s.

c. Natural Abundance ^{13}C – Metabolomics

In this last application, ^{13}C NMR enhanced by CP D-DNP is applied to metabolites in natural abundance. NMR is a major analytical technique in the field of metabolomics. On top of offering unambiguous structural information about the molecules that are present in solution, NMR has the advantage to be quantitative and reproducible. However, the method suffers from low sensitivity, compared to mass spectrometry, which is often preferred for this reason. Metabolomics studies by NMR are usually limited to protons. Due to limitations on experimental time, it is rare that ^{13}C spectra or 2D experiments are performed, even if they offer a better resolution and more reliable assignments. The large SNR enhancement offered by D-DNP can be an answer to solve this low sensitivity problem of metabolomics studies by NMR. The great advantage of CP-assisted D-DNP is that its performance is not sample-specific and simply relies on transferring the proton polarization in a glass-forming solvent to all dissolved metabolites by multiple contact $^1\text{H}\rightarrow^{13}\text{C}$ CP. As reported below, the acquisition of 1D and single-scan HMBC-type heteronuclear ($^1\text{H}\rightarrow^{13}\text{C}$) 2D correlation NMR spectra of biological extracts with natural ^{13}C abundance is possible, including measurements of metabolite signals that could not be detected without DNP even after hours of signal averaging [27].

In a first study, natural abundance tomato fruit pericarp extracts (20 mg of lyophilized dry powder), prepared following a standard protocol [28], were tested as DNP sample. The extracts were dissolved in the usual DNP solution ($\text{H}_2\text{O}:\text{D}_2\text{O}:\text{Glycerol-}d_8$ 1:4:5 with 40 mM TEMPOL) and hyperpolarized in 20 minutes by multiple contact $^1\text{H}-^{13}\text{C}$ CP. After dissolution, DNP-enhanced ^{13}C spectra were obtained using a single 90° pulse (figure 10). In parallel, a spectrum in thermal equilibrium without DNP was acquired using conventional sample preparation with the same amount of material on a 700 MHz spectrometer in about 12 h. The spectra in figure 10 focus on the quaternary ^{13}C region, where the DNP sensitivity gain is the most remarkable and where the polarization is best preserved because of favorable long T_1 .

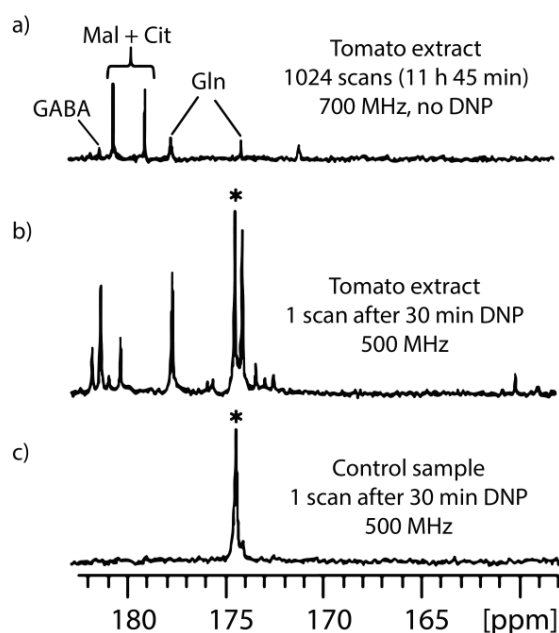


Fig. 10 ^{13}C NMR spectra of the quaternary carbons of tomato extracts. The molecules of γ -aminobutyrate (GABA), malate (Mal), citrate (Cit) and glutamine (Gln) are identified. (a) Conventional (non-hyperpolarised) spectrum of 20 mg extract (prepared from 20 mg lyophilized grounded tissue) dissolved in 700 μL D_2O , recorded with 1024 scans (11 h 45 min) at 700 MHz with a cryogenic probe. (b) Spectrum of an identical extract recorded with D-DNP combined with CP. The extract was first dissolved in a 200 μL mixture of $\text{H}_2\text{O}/\text{D}_2\text{O}/\text{glycerol-d}_8$ (2 : 3 : 5) doped with 25 mM TEMPOL, then enhanced by a standard D-DNP experiment with CP. (c) Same as (b), but the tomato extract was replaced by a control sample prepared under strictly identical conditions without any biological material. The hyperpolarized spectra result from the sum of six consecutive acquisitions using 30° pulses spaced by 7.7 s. The symbol * Indicates the signal of a ^{13}C -labeled pyruvate impurity.

The comparison of figures 10a and b clearly shows the sensitivity gain. The single-scan ^{13}C D-DNP spectrum (where the most intense peak has a SNR of 65) shows many more peaks than the thermal spectrum (where the most intense peak has a SNR of 30), although the latter was recorded with 1024 scans at 41 s intervals in ca. 12 h at a higher magnetic field (16.4 T). A confirmation that the additional peaks provide a spectral signature of the plant extract comes from figure 10c, recorded under the same conditions as figure 10b but on a control DNP sample which underwent the same extraction and preparation steps as the plant extract.

In a second experiment, it was shown that single-scan 2D NMR spectra [29] can be recorded by transferring the polarization of hyperpolarized ^{13}C nuclei to scalar-coupled protons after spatial encoding, followed by an echo-planar detection scheme. Single-scan HMBC-type experiments allow one to assign the quaternary carbons. This strategy was applied to extracts from human breast cancer cell lines, both at natural abundance and with partial isotopic enrichment (figure 11).

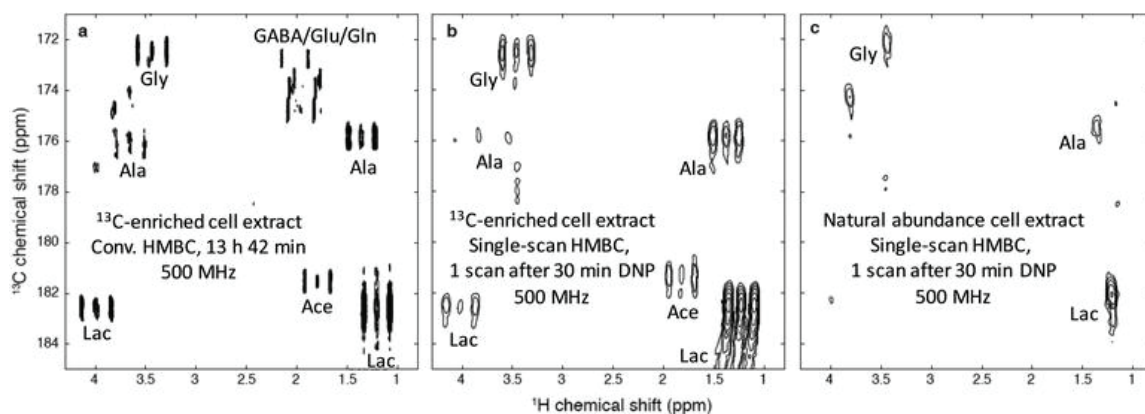


Fig. 11 HMBC-type $^1\text{H} \rightarrow ^{13}\text{C}$ correlation spectra of extracts of human breast cancer cell lines showing signals of acetate (Ace), alanine (Ala), γ -aminobutyrate (GABA), glutamine (Gln), glutamate (Glu), glycine (Gly) and lactate (Lac). (a) Conventional HMBC spectrum, recorded in 13 h 42 min at 500 MHz with a cryogenic probe, on a partially enriched extract (ca. 57 million extracted cells) dissolved in 700 μL D_2O . (b) Hyperpolarized single-scan spectrum. The cell extract was dissolved in 200 μL of a mixture of $\text{H}_2\text{O}/\text{D}_2\text{O}$ /glycerol- d_8 (2 : 3 : 5) with 25 mM TEMPOL and polarized for 30 min at 1.2 K and 6.7 T, and finally dissolved with 5 mL D_2O . A fraction of 700 μL of the hyperpolarized sample was injected in a 500 MHz spectrometer equipped with a cryogenic probe where the spectrum was recorded in a single scan. (c) Same as (b), but with a natural abundance extract (ca. 113 million cells) obtained from the same cell line.

With this study, we demonstrated the possibility of applying D-DNP to metabolomics research and more generally to studies in natural abundance.

Chapter 3: Spectra of highly polarized molecules in solution

The analysis of hyperpolarized samples gives the opportunity to study J couplings and to have a better resolution. A non-standard asymmetry was systematically observed for all highly polarized samples. It appears that this asymmetry is a function of the polarization of the coupled nuclei. In a two spin system, the observed peaks correspond of the single-quantum coherences of the four-level energy system. The intensity of each measured peak depends on the population of related states. The standard spectrum of a two-spin system gives two doublets. It is well known that the roof effect due to strong coupling induces an asymmetry like in figure 12. The asymmetry observed in hyperpolarized samples can be much larger than the strong coupling effect. This asymmetry is related to the polarization of the coupled spin [30].

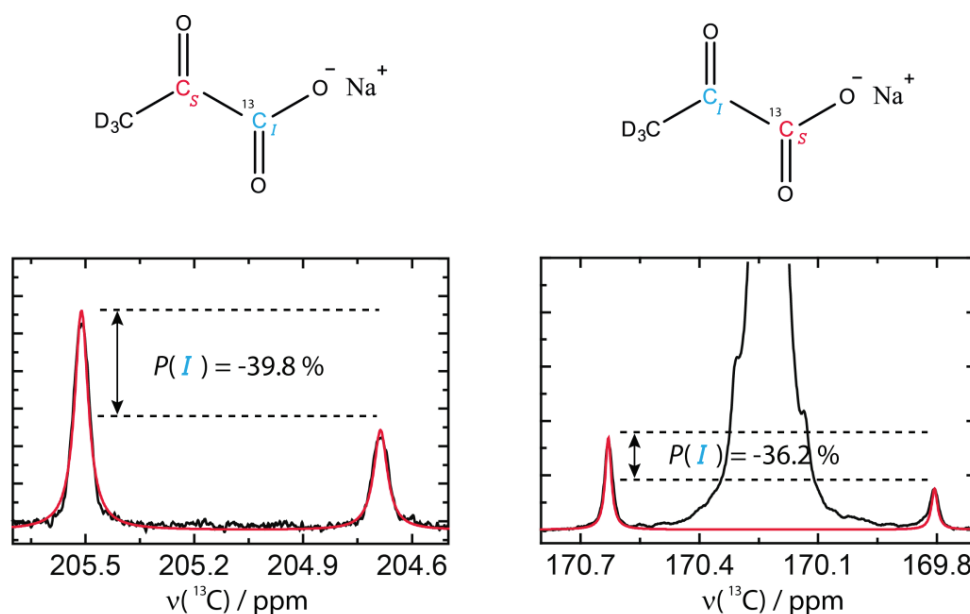


Fig. 12 ^{13}C Spectrum of hyperpolarized pyruvate. On the left, the doublet of the ketone carbon (red). The asymmetric signal is due to the polarization of the carboxylic carbon (blue). On the right, as before the asymmetry of the doublet of carboxylic carbon (red) is due to the polarization of the ketone carbon (blue). Note that the molecule is labeled on the carboxylic carbon.

References

1. Nelson, S.J.; Vigneron, D.; Kurhanewicz, J.; Chen, A.; Bok, R.; Hurd, R. *Applied Magnetic Resonance*, **2008**, 34(3-4),533-544.
2. Ardenkjaer-Larsen, J.H.; Laustsen, C.; Bowen, S.; Rizi, R. *Magnetic Resonance in Medicine*, **2014**, 71(1),50-56.
3. Kim, Y.; Hilty, C. *Angewandte Chemie-International Edition*, **2015**, 54(16),4941-4944.
4. Min, H.; Sekar, G.; Hilty, C. *Chemmedchem*, **2015**, 10(9),1559-1563.
5. Dalvit, C.; Fogliatto, G.; Stewart, A.; Veronesi, M.; Stockman, B. *Journal of Biomolecular Nmr*, **2001**, 21(4),349-359.
6. Friguet, B.; Chaffotte, A.F.; Djavadiohianance, L.; Goldberg, M.E. *Journal of Immunological Methods*, **1985**, 77(2),305-319.
7. Schuck, P. *Current Opinion in Biotechnology*, **1997**, 8(4),498-502.
8. Ladbury, J.E.; Chowdhry, B.Z. *Chemistry & Biology*, **1996**, 3(10),791-801.
9. Owicki, J.C. *Journal of Biomolecular Screening*, **2000**, 5(5),297-306.
10. Wyss, D.F.; McCoy, M.A.; Senior, M.M. *Current Opinion in Drug Discovery & Development*, **2002**, 5(4),630-647.
11. Fielding, L. *Progress in Nuclear Magnetic Resonance Spectroscopy*, **2007**, 51(4),219-242.
12. Buratto, R.; Mammoli, D.; Chiarparin, E.; Williams, G.; Bodenhausen, G. *Angewandte Chemie-International Edition*, **2014**, 53(42),11376-11380.
13. Salvi, N.; Buratto, R.; Bornet, A.; Ulzega, S.; Rebollo, I.R.; Angelini, A.; Heinis, C.; Bodenhausen, G. *Journal of the American Chemical Society*, **2012**, 134(27),11076-11079.
14. Levitt, M.H. *Annual Review of Physical Chemistry, Vol 63*, **2012**, 63,89-105.
15. Buratto, R.; Bornet, A.; Milani, J.; Mammoli, D.; Vuichoud, B.; Salvi, N.; Singh, M.; Laguerre, A.; Passemard, S.; Gerber-Lemaire, S.; Jannin, S.; Bodenhausen, G. *Chemmedchem*, **2014**, 9(11),2509-2515.
16. Sarkar, R.; Vasos, P.R.; Bodenhausen, G. *Journal of the American Chemical Society*, **2007**, 129(2),328-334.
17. Checa, A.; Ortiz, A.R.; dePascualTeresa, B.; Gago, F. *Journal of Medicinal Chemistry*, **1997**, 40(25),4136-4145.
18. Schanda, P.; Brutscher, B. *Journal of the American Chemical Society*, **2005**, 127(22),8014-8015.
19. Olsen, G.; Markhasin, E.; Szekely, O.; Bretschneider, C.; Frydman, L. *Journal of Magnetic Resonance*, **2016**, 264,49-58.
20. Gajan, D.; Bornet, A.; Vuichoud, B.; Milani, J.; Melzi, R.; van Kalker, H.A.; Veyre, L.; Thieuleux, C.; Conley, M.P.; Gruning, W.R.; Schwarzwald, M.; Lesage, A.; Coperet, C.; Bodenhausen, G.; Emsley, L.; Jannin, S. *Proceedings of the National Academy of Sciences of the United States of America*, **2014**, 111(41),14693-14697.
21. Vuichoud, V.B., A.; de Nanteuil, F.; Milani, J.; Canet, E.; Ji, X.; Miéville, P.; Weber, E.; Kurzbach, D.; Flamm, A.; Konrat, R.; Gossert, A.; Jannin, S.; Bodenhausen, G. . *To be submitted to Chemistry a European Journal*, **2016**.
22. Krishnan, V.V.; Murali, N. *Progress in Nuclear Magnetic Resonance Spectroscopy*, **2013**, 68,41-57.
23. Hore, P.J., *Nuclear magnetic resonance*. Oxford chemistry primers. 1995, Oxford ; New York: Oxford University Press. v, 90 p.
24. Chappuis, Q.; Milani, J.; Vuichoud, B.; Bornet, A.; Gossert, A.D.; Bodenhausen, G.; Jannin, S. *Journal of Physical Chemistry Letters*, **2015**, 6(9),1674-1678.
25. Harris, T.; Degani, H.; Frydman, L. *Nmr in Biomedicine*, **2013**, 26(12),1831-1843.
26. Miclet, E.; Abergel, D.; Bornet, A.; Milani, J.; Jannin, S.; Bodenhausen, G. *Journal of Physical Chemistry Letters*, **2014**, 5(19),3290-3295.

27. Dumez, J.N.; Milani, J.; Vuichoud, B.; Bornet, A.; Lalande-Martin, J.; Tea, I.; Yon, M.; Maucourt, M.; Deborde, C.; Moing, A.; Frydman, L.; Bodenhausen, G.; Jannin, S.; Giraudeau, P. *Analyst*, **2015**, 140(17),5860-5863.
28. Benard, C.; Bernillon, S.; Biais, B.; Osorio, S.; Maucourt, M.; Ballias, P.; Deborde, C.; Colombie, S.; Cabasson, C.; Jacob, D.; Vercambre, G.; Gautier, H.; Rolin, D.; Genard, M.; Fernie, A.R.; Gibon, Y.; Moing, A. *Journal of Experimental Botany*, **2015**, 66(11),3391-3404.
29. Tal, A.; Shapira, B.; Frydman, L. *Angewandte Chemie-International Edition*, **2009**, 48(15),2732-2736.
30. Vuichoud, B.; Milani, J.; Chappuis, Q.; Bornet, A.; Bodenhausen, G.; Jannin, S. *Journal of Magnetic Resonance*, **2015**, 260,127-135.

Part D:

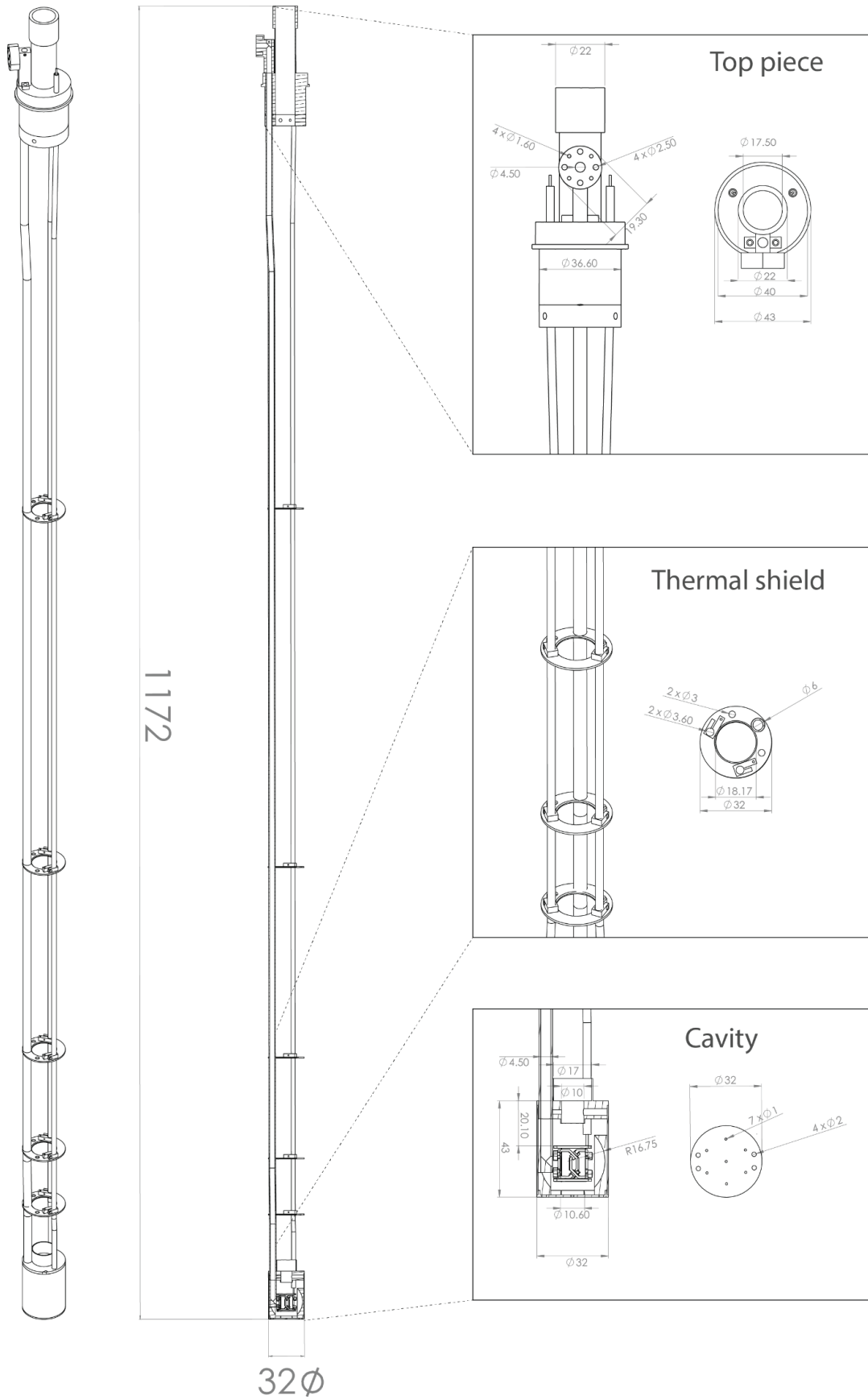
Conclusion

We have demonstrated in this Thesis several instrumental steps forward in D-DNP. We have shown how with an improved microwave irradiation system, together with an optimized Cross Polarization strategy, one could afford rapid and high polarization in ^{13}C and ^{15}N , with for example unprecedented polarization levels up to $P(^{15}\text{N}) = 25\%$. We have also shown how hyperpolarization could be better preserved during transfer in the liquid state by using a new concept of a magnetic tunnel that was already successfully installed in Lausanne and Paris. These advances are of direct relevance for many applications such as drug discovery and metabolomics that are also demonstrated in this Thesis. Finally, a new D-DNP approach using triplet state was initiated, with an already functioning setup that will be used in the near future.

Part E:

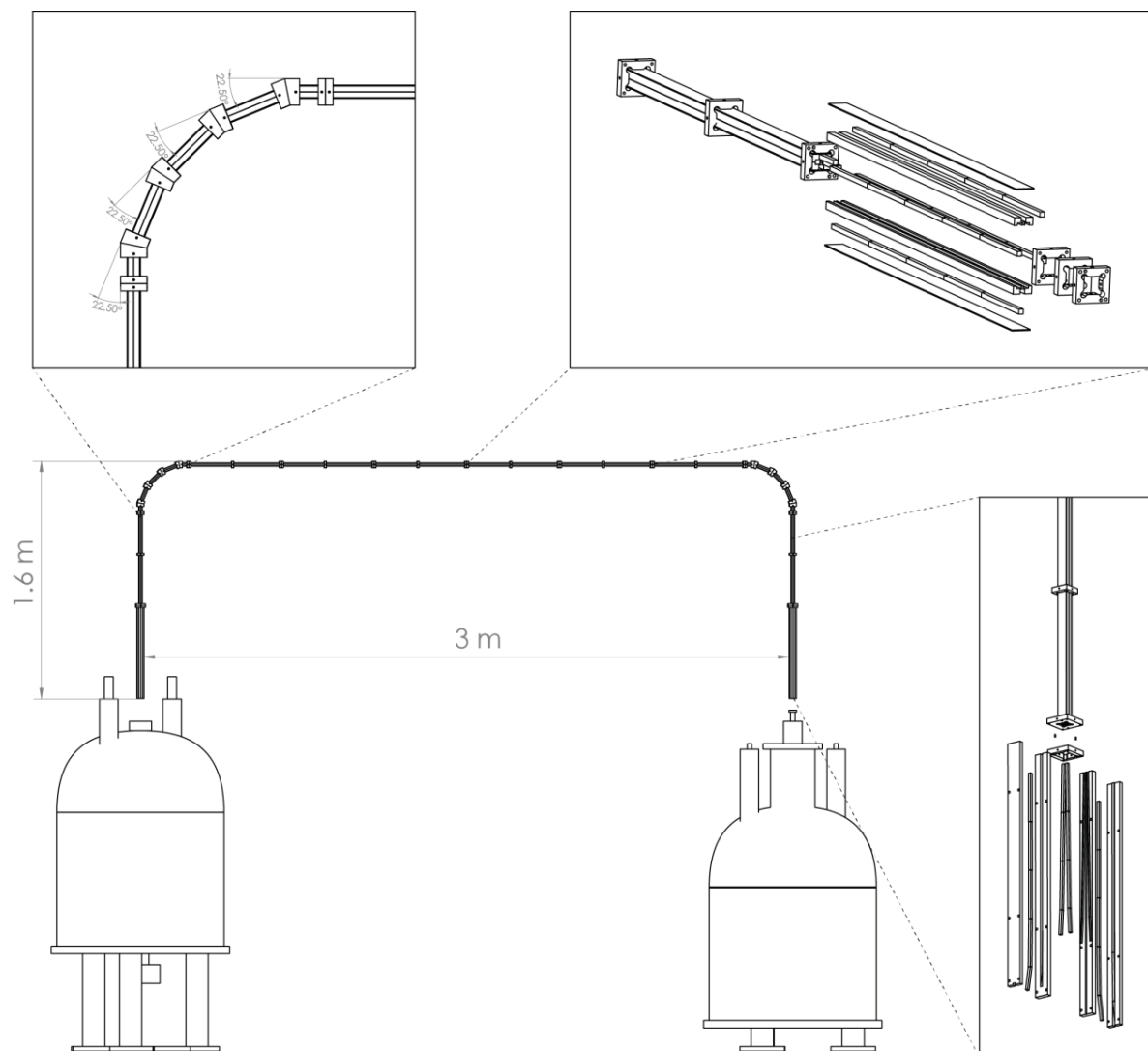
Annexes

Probe design

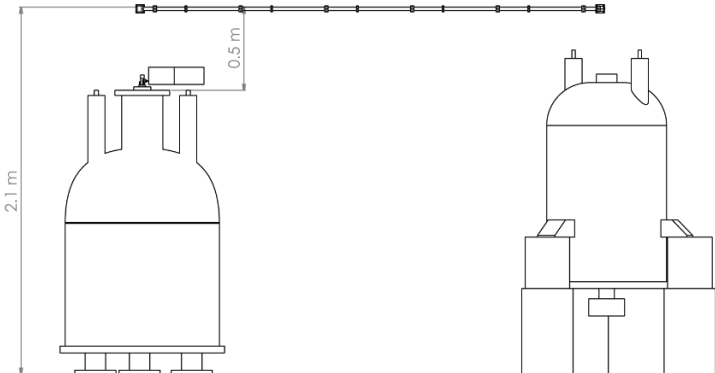
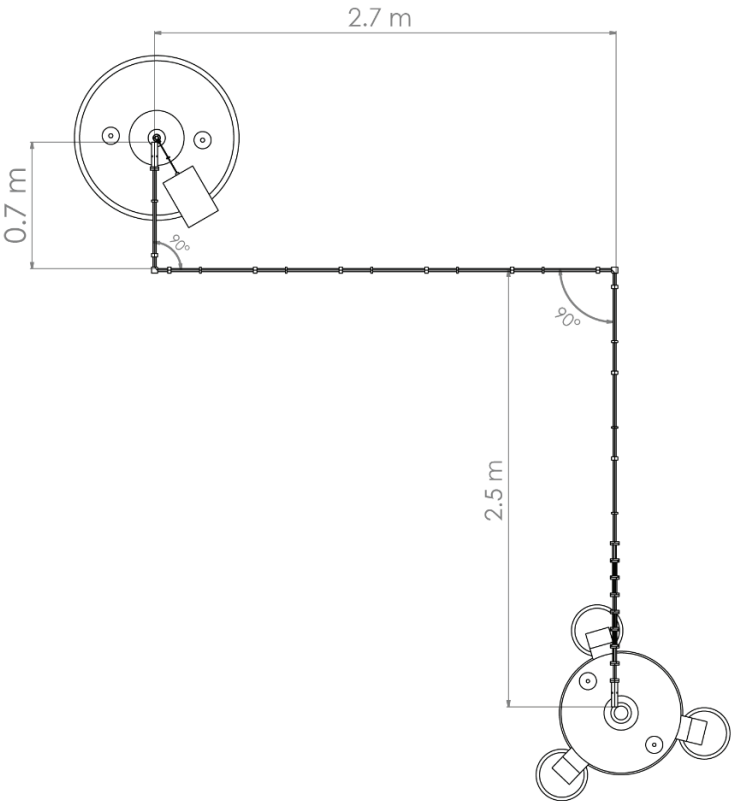
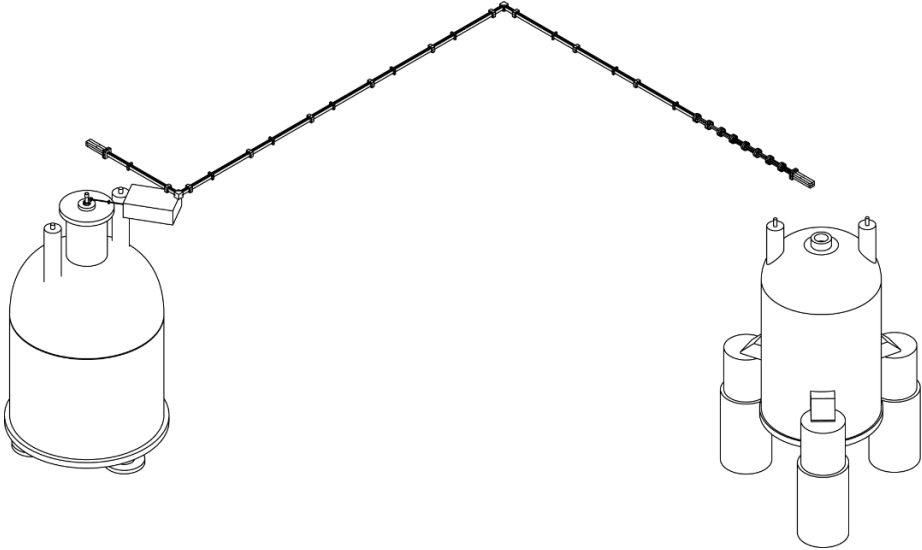


Magnetic tunnel design

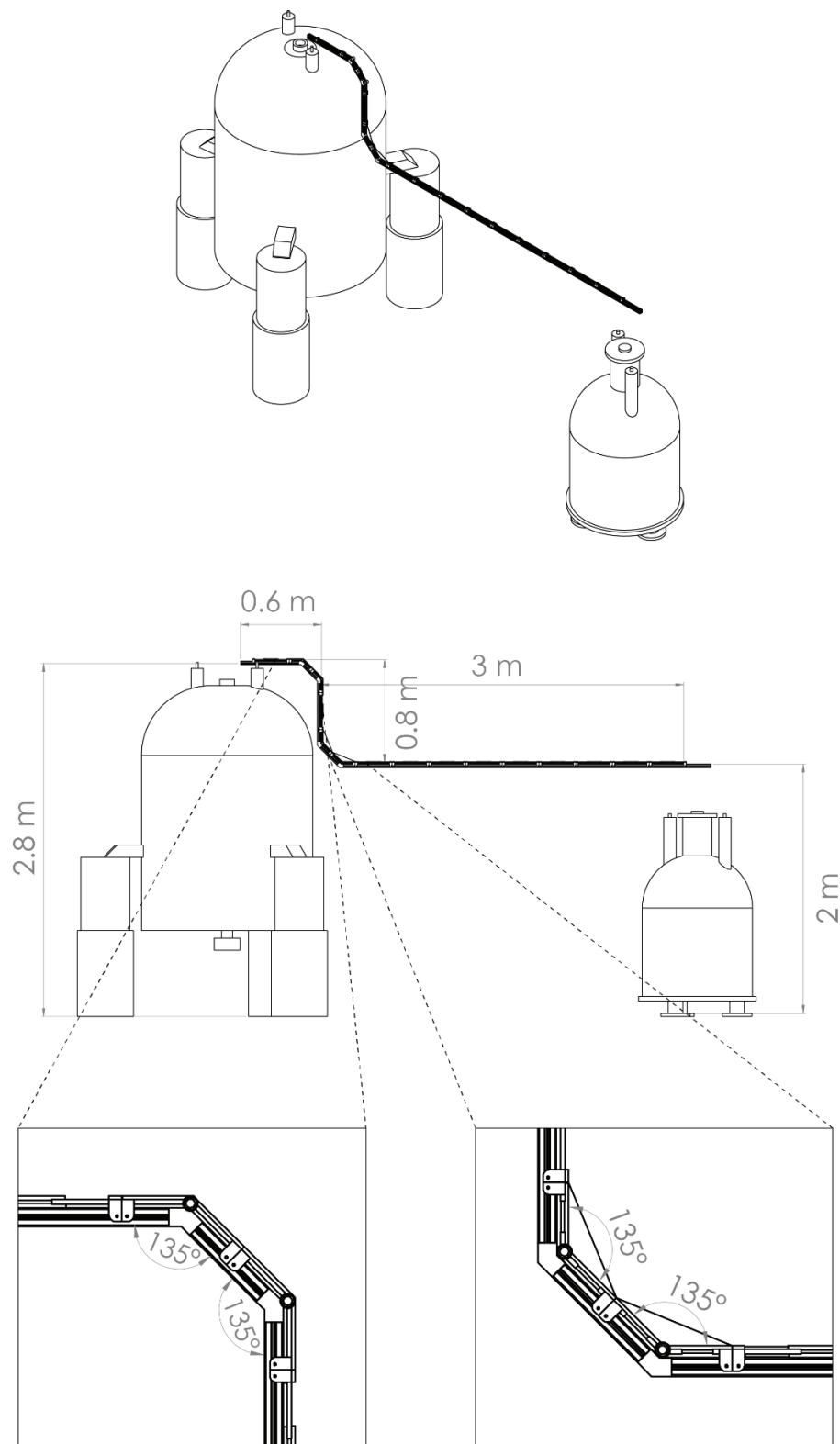
6.7 T DNP Polarizer to 300 MHz spectrometer in EPFL



6.7 T DNP Polarizer to 500 MHz spectrometer in EPFL



6.7 T DNP Polarizer to 800 MHz spectrometer in ENS Paris



Remerciement

Tout d'abord, je tiens à remercier tous les membres de mon jury, **Frank Engelke**, **Jan van Bentum**, **Lyndon Emsley** et **Kay Severin**, pour avoir non seulement accepté de lire et juger mon travail mais aussi de l'avoir fait.

Je remercie grandement mon directeur de thèse, **Geoffrey Bodenhausen**, qui m'a donné la chance de faire, tout d'abord, mon travail de master dans son laboratoire et par la suite un doctorat. J'ai beaucoup apprécié travailler dans son laboratoire, notamment grâce à la grande liberté que nous avons pour réaliser nos projets. Grande figure de l'RMN, je suis fier d'avoir fait partie de son équipe.

La personne à qui je dois beaucoup et que je remercie chaleureusement est mon codirecteur de thèse, **Sami Jannin**. Il m'a non seulement appris tout ce que je sais au sujet de la DNP, mais ça a été aussi mon mentor "bricolage", me sortant totalement de ma chimie traditionnelle pour faire des projets orientés très physiques. Scientifique de renom, il garde un coter plus rigolo comme lorsqu'il proposa de créer le *Gang des Barbues* à l'occasion du symposium DNP à Copenhague en 2014.

Mes remerciements vont aussi à mon équipe scientifique ou *Mafia Romande* (ou encore *DNP Team*) avec qui j'ai travaillé durant quatre ans. Une thèse au sein de ce laboratoire est réellement un travail d'équipe. Tous mes projets auraient été nettement plus difficiles et surtout moins marrants sans mes deux acolytes : **Aurélien Bornet**, grand valaisan n'ayant d'égal à son grand cœur que sa barbe (et sûrement son fois). Toujours motivé à "s'en boire une", c'est aussi un danseur de valse hors pair exerçant dans des caves mal famées à des heures non respectables. **Basile Vuichoud**, le Vaudois. Ayant dans un premier temps laissé sa description à ce simple mot (qui le résume ôh tellement bien), j'ai décidé néanmoins de peaufiner sa description. Amateur de vin (vaudois) et grand fan du comptoir suisse et du LHC (le CERN ou le hockey, je vous laisse deviner), c'est avec lui que j'ai partagé mon bureau lieu-dit *La Place des Beaufs*. À ces deux-là c'est ajouté durant deux ans **Xiao Ji**, *le plus suisse de tous les chinois*, et pour preuve j'en ai les fondues qu'il apprécie (particulièrement au Trois-Sifflet avec son pote, le patron), mais surtout la St-Martin où il a grandement apprécié la culture jurassienne.

Merci à toute la *Mafia Latino* : **Roberto Buratto** avec qui nous étions les deux petits étudiants en Master (à l'époque...), de surcroît fan de pizza à l'ananas, **Estel Canet** et sa motivation inégale à fêter les défenses de thèse (jusqu'au bout de la nuit), ainsi que **Daniele Mammoli** ou *comment le café devient un art*.

Je remercie aussi **Pascal Miéville** pour ses conseils surtout au début de ma thèse et "d'avoir été là" pour s'occuper des spectromètres lorsque plus rien ne fonctionnait. Merci aussi à **Béatrice Bliesener**

pour s'être très bien occupé de nos cas pour toute l'administratif. Merci à **Roger Mottier** et **toute l'équipe de l'atelier mécanique** de la section de chimie pour leur grand et précieux savoir-faire.

Merci aussi à toute l'équipe du LRM pour leur sympathique présence (et la nouvelle déco des bureaux). **Jasmine** dite *Caribou*, **Federico**, **Brennan**, **Albert**, **Nadia**, **Claudia**, **Snaedis**, **Dominik** et **Subba**. Spécial big up (oui j'ai osé utiliser ce terme totalement naze) à **Arthur**, premier élément du LRM qui m'a initié au tour de France et presque au trampoline, et **Baptiste**, anar des grands chemins, et par grand chemin j'entends !!! bref.

Un grand merci aussi à **Marcel Schreier**, **Valentin Manzanares**, **Loïc Arm**, **Véronique Amstutz**, anciens collègues d'étude avec qui j'ai beaucoup apprécié passer du moment durant ces quatre années.

Merci encore **aux cuisinières Taï** de la *Banane* qui se souciaient personnellement de mon alimentation en me donnant des portions *sur mesure*.

Enfin, je remercie tout le comité de **Balélec**, comité dans lequel je suis resté durant près de six ans. Le fait d'avoir fait partie d'une telle association a sans nul doute influencé ma vie sur l'EPFL. Véritable petite entreprise, elle nous apprend beaucoup dans la gestion de projets, sans compter l'aspect humain qui nous fait découvrir des gens fabuleux.

COMPETENCIES

Languages

French : Mother tongue
English : Advanced
German : Basic knowledge

Computer skill

Adobe Illustrator, Solidworks, Matlab
LabVIEW (basic), MS Office Suite

INTERESTS

Sport : Rock climbing, Boxing, Running, Mountain Bike

Music : I like to play the trombone.

Other : Since my childhood, I am part of a group of Scout. I am still now in the head of the group.

PUBLICATIONS

1. **Milani, J.**; Vuichoud, B.; Bornet, A.; Melzi, R.; Jannin, S.; Bodenhausen, G. *Hyperpolarization of Nitrogen-15 Nuclei by Cross Polarization and Dissolution Dynamic Nuclear Polarization* to be submitted to Review of Scientific Instruments, 2016
2. Kurzbach, D.; Weber, E.; Jhajharia, A.; Cousin, S.; Sadet, A.; Marhabaie, S.; Canet, E.; Birlirakis, N.; **Milani, J.**; Jannin, S.; Eschenko, D.; Melzi, R.; Luetolf, S.; Sacher, M.; Kempf, J.; Weller, M.; Bodenhausen, G.; Abergel, D. *Dissolution DNP of Deuterated Molecules*, To be submitted to J. Chem. Phys., 2016
3. Vuichoud, V.; Bornet, A.; de Nanteuil, F.; **Milani, J.**; Canet, E.; Ji, X.; Miéville, P.; Weber, E.; Kurzbach, D.; Flamm, A.; Konrat, R.; Gossert, A.; Jannin, S.; Bodenhausen, G. *Filterable Agents for Hyperpolarization of Water, Metabolites, and Proteins*, To be submitted to Chemistry a European Journal, 2016.
4. Poschko, M.T.; Vuichoud, B.; **Milani, J.**; Bornet, A.; Bechmann, M.; Bodenhausen, G.; Jannin, S.; Muller, N. *Chemphyschem*, 2015, 16(18),3859-3864.
5. Chappuis, Q.; **Milani, J.**; Vuichoud, B.; Bornet, A.; Gossert, A.D.; Bodenhausen, G.; Jannin, S. *Journal of Physical Chemistry Letters*, 2015, 6(9),1674-1678.
6. Mammoli, D.; Salvi, N.; **Milani, J.**; Buratto, R.; Bornet, A.; Sehgal, A.A.; Canet, E.; Pelupessy, P.; Carnevale, D.; Jannin, S.; Bodenhausen, G. *Physical Chemistry Chemical Physics*, 2015, 17(40),26819-26827.
7. **Milani, J.**; Vuichoud, B.; Bornet, A.; Mieville, P.; Mottier, R.; Jannin, S.; Bodenhausen, G. *Review of Scientific Instruments*, 2015, 86(2).
8. Mammoli, D.; Vuichoud, B.; Bornet, A.; **Milani, J.**; Dumez, J.N.; Jannin, S.; Bodenhausen, G. *Journal of Physical Chemistry B*, 2015, 119(10),4048-4052.

9. Dumez, J.N.; **Milani, J.**; Vuichoud, B.; Bornet, A.; Lalande-Martin, J.; Tea, I.; Yon, M.; Maucourt, M.; Deborde, C.; Moing, A.; Frydman, L.; Bodenhausen, G.; Jannin, S.; Giraudeau, P. *Analyst*, 2015, 140(17),5860-5863.
10. Bornet, A.; Ji, X.; Mammoli, D.; Vuichoud, B.; **Milani, J.**; Bodenhausen, G.; Jannin, S. *Chemistry-a European Journal*, 2014, 20(51),17113-17118.
11. Buratto, R.; Bornet, A.; **Milani, J.**; Mammoli, D.; Vuichoud, B.; Salvi, N.; Singh, M.; Laguerre, A.; Passemard, S.; Gerber-Lemaire, S.; Jannin, S.; Bodenhausen, G. *Chemmedchem*, 2014, 9(11),2509-2515.
12. Linde, A.J.P.; Bornet, A.; **Milani, J.**; Vuichoud, B.; Melzi, R.; Jannin, S.; Bodenhausen, G. *Physical Chemistry Chemical Physics*, 2014, 16(45),24813-24817.
13. Gajan, D.; Bornet, A.; Vuichoud, B.; **Milani, J.**; Melzi, R.; van Kalker, H.A.; Veyre, L.; Thieuleux, C.; Conley, M.P.; Gruning, W.R.; Schwarzwald, M.; Lesage, A.; Coperet, C.; Bodenhausen, G.; Emsley, L.; Jannin, S. *Proceedings of the National Academy of Sciences of the United States of America*, 2014, 111(41),14693-14697.
14. Vuichoud, B.; **Milani, J.**; Bornet, A.; Melzi, R.; Jannin, S.; Bodenhausen, G. *Journal of Physical Chemistry B*, 2014, 118(5),1411-1415.
15. Miclet, E.; Abergel, D.; Bornet, A.; **Milani, J.**; Jannin, S.; Bodenhausen, G. *Journal of Physical Chemistry Letters*, 2014, 5(19),3290-3295.
16. Bornet, A.; **Milani, J.**; Vuichoud, B.; Linde, A.J.P.; Bodenhausen, G.; Jannin, S. *Chemical Physics Letters*, 2014, 602,63-67.
17. Bornet, A.; **Milani, J.**; Wang, S.T.; Mammoli, D.; Buratto, R.; Salvi, N.; Segawa, T.F.; Vitzthum, V.; Mieville, P.; Chinthapalli, S.; Perez-Linde, A.J.; Carnevale, D.; Jannin, S.; Caporini, M.; Ulzega, S.; Rey, M.; Bodenhausen, G. *Chimia*, 2012, 66(10),734-740.

CONFERENCES

Talks:

Hyperpolarization of ^{15}N by Dynamic Nuclear Polarization using a Cross Polarization probe compatible for dissolution experiments, Jonas Milani, Basile Vuichoud, Aurélien Bornet, Xiao Ji, Roberto Melzi, Sami Jannin and Geoffrey Bodenhausen, , COST at 5th International DNP Symposium, Egmond aan Zee, Netherlands, 2015.

Cross Polarization of ^{15}N combined with Dynamic Nuclear Polarization Dissolution, Jonas Milani, Basile Vuichoud, Aurélien Bornet, Roberto Melzi, Sami Jannin and Geoffrey Bodenhausen, , WG2-WG3 joint meeting, Southampton, UK, 2014.

Posters:

Hyperpolarization of ^{15}N by Dynamic Nuclear Polarization using a Cross Polarization probe compatible for dissolution experiments, Jonas Milani, Basile Vuichoud, Aurélien Bornet, Xiao Ji, Roberto Melzi, Sami Jannin and Geoffrey Bodenhausen, , 5th International DNP Symposium, Egmond aan Zee, Netherlands, 2015.

A magnetic tunnel for preserving hyperpolarization in Dissolution-DNP experiments, Jonas Milani, Basile Vuichoud, Aurélien Bornet, Pascal Miéville¹, Sami Jannin and Geoffrey Bodenhausen, 55th Experimental Nuclear Magnetic Resonance Conference ENC, Boston, Massachusetts, USA, 2014.

Microwave and Radio-Frequency Coupling Strategies for Dissolution-DNP, Jonas Milani, Roberto Melzi, Basile Vuichoud, Aurélien Bornet, Sami Jannin and Geoffrey Bodenhausen, 4th International DNP Symposium, Helsingør, Denmark, 2013.

Prizes:

Best Poster Prize, Hyperpolarization of ^{15}N by Dynamic Nuclear Polarization using a Cross Polarization probe compatible for dissolution experiments, 5th International DNP Symposium, Egmond aan Zee, Netherlands, 2015.

